5-2024

GEOCHEMICAL MECHANISMS OF TRACE ELEMENT MOBILIZATION AND ATTENUATION IN A CRUDE-OIL CONTAMINATED AQUIFER

Audrey Madison Davis
Trinity University

GEOCHEMICAL MECHANISMS OF TRACE ELEMENT MOBILIZATION AND ATTENUATION IN A CRUDE-OIL CONTAMINATED AQUIFER

Audrey Madison Davis

A DEPARTMENT HONORS THESIS SUBMITTED TO THE
DEPARTMENT OF EARTH AND ENVIRONMENTAL GEOSCIENCES AT TRINITY UNIVERSITY
IN PARTIAL FULFILLMENT OF THE REQUIREMENTS FOR GRADUATION WITH DEPARTMENTAL HONORS

April 12, 2024

Brady Ziegler
THESIS ADVISOR

Dr. Benjamin Surpless
DEPARTMENT CHAIR

Jennifer Henderson, AVPAA

Student Agreement

I grant Trinity University (“Institution”), my academic department (“Department”), and the Texas Digital Library ("TDL") the non-exclusive rights to copy, display, perform, distribute and publish the content I submit to this repository (hereafter called "Work") and to make the Work available in any format in perpetuity as part of a TDL, digital preservation program, Institution or Department repository communication or distribution effort.

I understand that once the Work is submitted, a bibliographic citation to the Work can remain visible in perpetuity, even if the Work is updated or removed.

I understand that the Work's copyright owner(s) will continue to own copyright outside these non-exclusive granted rights.

I warrant that:

1) I am the copyright owner of the Work, or
2) I am one of the copyright owners and have permission from the other owners to submit the Work, or
3) My Institution or Department is the copyright owner and I have permission to submit the Work, or
4) Another party is the copyright owner and I have permission to submit the Work.

Based on this, I further warrant to my knowledge:

1) The Work does not infringe any copyright, patent, or trade secrets of any third party,
2) The Work does not contain any libelous matter, nor invade the privacy of any person or third party, and
3) That no right in the Work has been sold, mortgaged, or otherwise disposed of, and is free from all claims.

I agree to hold TDL, DPN, Institution, Department, and their agents harmless for any liability arising from any breach of the above warranties or any claim of intellectual property infringement arising from the exercise of these non-exclusive granted rights.”

I choose the following option for sharing my thesis (required):

[X] Open Access (full-text discoverable via search engines)
[ ] Restricted to campus viewing only (allow access only on the Trinity University campus via digitalcommons.trinity.edu)

I choose to append the following Creative Commons license (optional): CC-BY-NC

GEOCHEMICAL MECHANISMS OF TRACE ELEMENT MOBILIZATION AND ATTENUATION IN A CRUDE-OIL CONTAMINATED AQUIFER

Audrey Madison Davis

Table of Contents

Abstract

Biodegradation of crude oil in a contaminated aquifer near Bemidji, MN has formed distinct geochemical zones downgradient from the spill site. The development of methanogenic, iron (Fe)-reducing, and interface zones have resulted in regions of distinct pH and/or redox state. As a result of these geochemical changes, geogenic trace elements have been mobilized from various minerals in native sediment into groundwater. We used sequential extractions of sediment from geochemical zones along the plume path to elucidate the sediment phase origins of 30 trace elements and provide insight into mobilization and attenuation mechanisms. Extractions targeted elements in surface exchangeable, carbonate, oxides and hydroxides, and organic phases, which were then analyzed with inductively coupled plasma-mass spectrometry (ICP-MS) and -optical emission spectroscopy and analyzed statistically. Organic-bound trace elements were further characterized using high performance liquid chromatography-size exclusion chromatography-ICP-MS and excitation-emission spectra to develop a parallel factor analysis model.

Results indicate that lead (Pb), manganese (Mn), and Fe are mobilized due to reductive dissolution of Fe and/or Mn oxides due to anaerobic biodegradation. Calcium, barium, magnesium, nickel, and strontium are mobilized into groundwater from native carbonates due to acidity associated with degradation intermediates and methanogenesis. Combined oxide and carbonate dissolution have created elevated levels of trace elements in groundwater, where they become human and environmental health hazards concomitant with petroleum hydrocarbons. Mobilization from native organic matter in sediment was also assessed, but it was found to be negligible.

Attenuation of mobilized elements occurs variably downgradient in sediment of different geochemical zones. Oxides and hydroxides did not constitute significant attenuation within the plume, as the distance examined in this study ended in the anoxic plume. Carbonate mineral

precipitation was a significant sink for many elements in the methanogenic and interface zones, including elements like Pb, Fe, and Mn that had originated in oxides and hydroxides in the background. Organic complexes within the plume helped to attenuate arsenic, chromium, and boron, among other elements, by metalloorganic complexation with heavy molecular weight organic matter.

Assessing a host of elements in a contaminated aquifer provides new knowledge of elemental cycling and the subsequent impacts to groundwater quality. Advancing knowledge of the behavior of geogenic contaminants following an oil spill aids efforts to remediate secondary contaminants and protect groundwater resources.

I. Introduction

Naturally occurring trace elements are present in aquifer sediment either through incorporation into mineral structures or through sorption on mineral surfaces and organic matter. The mobility of a trace element largely depends on the mineral it is associated with, which in turn is dependent on environmental factors, such as pH, redox conditions, and the presence of other competing ions and/or chelators (Berndt, 1987; Ziegler et al., 2017; Boiteau et al., 2018). Human activity can introduce excess organic carbon into aquifer systems through events including but not limited to oil spills, landfill leachate, sewage plumes, and jet fuel spills, which can alter these controlling factors and affect mineral phase stability (Baedecker et al., 1993; Cozzarelli et al., 2016; Delemos et al., 2006; Amirbahman et al., 2006; Long & Aelion, 1998). The biodegradation of organic carbon contaminants by microorganisms in groundwater environments can produce byproducts, like organic acids. These byproducts can also result in changes to pH and redox conditions and may further reduce mineral phase stability. While biodegradation may serve as an effective remediation strategy of organic contaminants in aquifers (Kalia et al., 2022), secondary contaminants in the form of mobilized geogenic trace elements may enter groundwater and persist for centuries (Ziegler et al., 2021). These processes ultimately have longer-term water quality consequences than the original organic contaminant.

Following an organic contaminant release, aquifer conditions enter a state of geochemical disequilibrium, resulting in rapid growth of microbial populations due to biodegradation (oxidation) of organic carbon coupled with consumption of dissolved oxygen (DO), creating anoxic conditions (Baedecker et al., 1993). Upon the depletion of DO, a series of anaerobic redox reactions for biodegradation occur with a lower thermodynamic yield than that of aerobic degradation (Bennett et al., 1993). Based on microbial availability, biodegradation will continue

to occur with different electron acceptors (Borch et al., 2010). Upon the depletion of DO, denitrification, Fe(III)-, and Mn(IV)-reduction can become the dominant terminal electron accepting processes (TEAPs) in a contaminated region (Baedecker et al., 1993; Howarth, 2002; Druschel et al., 2008; Miyata et al., 2006). Increased concentrations of dissolved ferrous Fe, Mn, and CH_4 indicate reducing conditions within an aquifer (Bennet et al., 1993). Fe(III)-minerals are reduced, contaminants mobilize from the sediment, such that sediment within the hydrocarbon plume is depleted of Fe(III) (Tuccillo et al., 1999). In association, ions that are sorbed to the surface of Fe(III)-minerals are mobilized simultaneously (Zachara et al., 2000). Subsequently to the depletion of reducible nitrate, Mn-, and Fe-oxides, sulfate reduction may occur, followed by methanogenesis (Morse & Luther, 1999; Kleikemper et al., 2005). Changing pH and redox conditions due to biodegradation of organic carbon causes alterations in the stability of mineral phases, including: exchangeable surface ions, carbonates, oxides and hydroxides, sulfides, and trace elements complexed with organic matter (Tessier et al., 1979).

The degradation of hydrocarbon into carbon dioxide (CO_2) by microorganisms produces organic acid intermediates, which can contribute to the dissolution of mineral carbonates in the aquifer (Cozzarelli et al., 1990). The dissolution rates of calcite and dolomite increase in earnest around pH 6.0-6.5, and continue to increase with lowering pH (Chou et al., 1989). Field and laboratory observations have illustrated that the anaerobic biodegradation of organic contaminants like benzene and alkylbenzenes produce phenol and organic acids downgradient of biodegradation (Cozzarelli et al., 1990). Carbonate mineral dissolution is observed with increases in Ca, Mg, and HCO_3^- with relation to increases in CO_2 and decreases in pH from organic acid byproducts (Bennett et al., 1993). Decreases in pH and the production of organic acids can contribute to minor

dissolution of feldspars (Bennett et al., 1993). Ions that are sorbed to the surfaces of carbonates or feldspars can mobilize with the dissolution of these minerals (Pokrovsky & Schott, 2002).

Geogenic contaminants may be further mobilized or attenuated by complexing with organic matter (OM) or dissolved organic matter (DOM) present in the aquifer. Organic acids formed due to biodegradation may complex with SiO_2 to promote the dissolution of quartz minerals and mobilize associated element (Bennett et al., 1993). Trace elements may also be sequestered by OM as they form metalloorganic complexes with DOM as ternary complexes, wherein a cation bridge connects a contaminant element with DOM (Aftabtalab et al., 2022). In particular, Ojeda et al. (2023) observed the process of complexing arsenic (As) with DOM under lab-simulated groundwater conditions. Increasing DOM concentrations resulted in increasing As complexation across multiple forms of DOM (Ojeda et al., 2023).

Groundwater contamination by trace elements poses a threat to environmental, ecosystem, and human health. When ingested, naturally occurring trace elements such as arsenic (As), nickel (Ni), barium (Ba), strontium (Sr), and cobalt (Co) can present numerous health complications. These complications can include, but are not limited to, kidney and liver dysfunction, gastrointestinal disease, and cardiovascular, skin, and bladder cancers (Sunderman et. al, 1989; Webster et. al, 1980; Kojola et. al, 1979; Ratnaike, 2003; Léonard & Lauwerys, 1980). Some elements, such as chromium (Cr), serve as a micronutrient in some valence states (Cr(III)) and exposure levels, but can become carcinogenic in others (Cr(VI)) (Pavesi and Moreira, 2020). Even low blood lead (Pb) levels in children can result in neurological dysfunction, as no amount of lead exposure is considered safe for children (Naranjo et al., 2020). Furthermore, the effects of co-exposure to different elemental contaminants may amplify or subdue the toxicity of each co-occurring contaminant, depending on which elements co-occur (Ollson et al., 2017). Regulatory

agencies, such as the United States Environmental Protection Agency (U.S. EPA), and health and safety agencies, such as the World Health Organization (WHO), provide guidelines on the acceptable levels of inorganic contaminants by establishing maximum acceptable contaminant levels for water resources (U.S. Environmental Protection Agency, 2023; World Health Organization, 2022). However, some potentially toxic trace elements on the U.S. EPA contaminant candidate list remain unregulated due to a dearth of toxicology studies to inform a regulatory threshold.

Study Site

In 1979, a pipeline transporting crude oil near Bemidji, Minnesota burst, contaminating the underlying glacial outwash aquifer (Pleistocene Bagley Outwash Plain) with 1,700,000 liters of crude oil (Pfannkuch, 1979). Following clean-up efforts, 400,000 L of crude oil remained floating on the water table (Pfannkuch, 1979). Partial dissolution of the oil body generated a hydrocarbon plume in the groundwater (Baedecker et al., 1993). In 1983, the site became a United States Geological Survey research site aimed at understanding the natural attenuation, transport, and fate of hydrocarbons in the aquifer subsurface (Figure 1). Since the spill, microorganism-mediated biodegradation of hydrocarbons has naturally diminished the remaining crude oil, resulting in distinct geochemical zones (Figure 1) in the direction of groundwater flow (Baedecker et al., 1993; Bennett et al., 1993; Jones et al., 2023). The resulting regions of distinct pH and/or redox state create geochemical conditions favorable to the mobilization of secondary geogenic contaminants from aquifer sediments into groundwater (Jones et al., 2023). While only one site is examined in this study, the processes in action within the Bemidji aquifer are well-characterized such that

greater general conclusions about elemental cycling could be extrapolated for understanding about larger scale systems.

Long-term research and monitoring of the Bemidji oil spill site resulted in a well-characterized geochemical profile spanning more than four decades, with initial characterization of the aquifer conducted in the 1980s. The Pleistocene Bagley Outwash Plain is composed predominantly of silty sand (54-61% quartz), with both potassium (8.0-13%) and plagioclase feldspars (17-20%) and carbonates (4.1-6.9%) (Bennett et al., 1993). The water table is located 6-10 m below land surface, in a 20 m thick aquifer (Bennett et al., 1993). Groundwater flows northeast, with local discharge in a small lake about 400 m downgradient from the spill site. In the uncontaminated aquifer, both historically and in the modern-day, the median groundwater pH is 7.60, (Bennett et al., 1993; Baedecker et al., 1993; Jones et al., 2023). Underneath the center of the oil body (locally referenced by well 421 in Figure 1), the pH was slightly acidic with high concentrations of dissolved carbon and no detectable DO (Bennett et al, 1993). The median contaminated groundwater pH in the anoxic zone was reported at pH 6.93 (Baedecker et al., 1993). Using kriged data informed by sampling, the pH in the modern methanogenic region is approximately 5.5-6.5 pH, the modern Fe-reducing region is 6.4-7.0 pH (Jones et al., 2023). At 178 m downgradient of the plume in the 1980s, the pH was 7.4 (Berndt, 1987). Approximately 200 m downgradient from the oil body in the modern day, the pH is 7.1-7.2 (Jones et al., 2023).

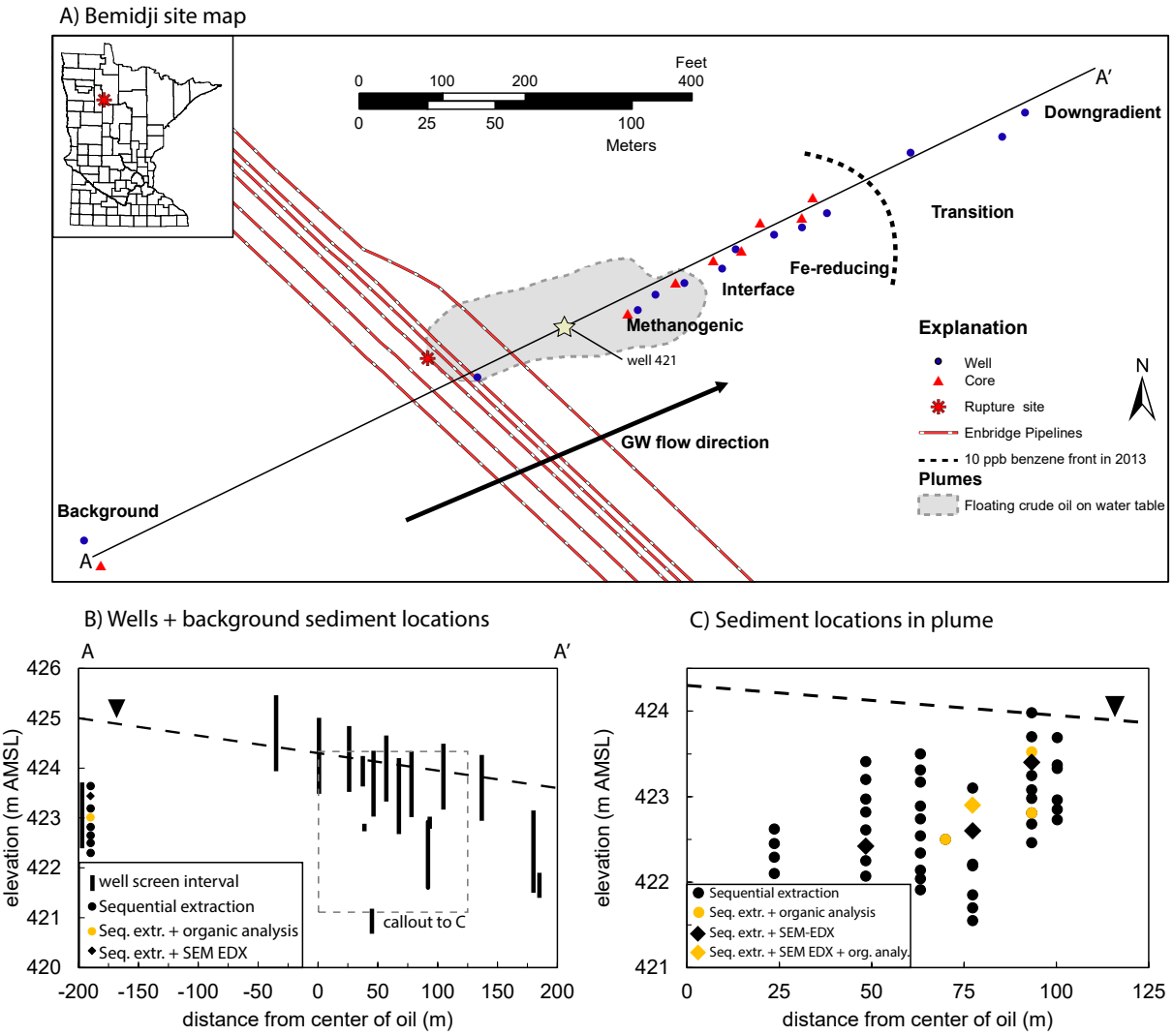

Figure 1. (A) Overhead view of the Bemidji spill site indicating the location of the crude oil body, location of wells used in this study (blue circles), and the locations of cores examined in this study (red triangles). Transect A-A' crosses through the center of the contaminant plume. The inset indicates the Bemidji site location in Minnesota. (B) Cross-sectional view of wells sampled for this study, including indicators of which sediment samples from the background core were used for which of the chemical characterization analyses. The dashed box indicates the bounds of (C). (C) Cross-sectional view of sediment samples collected for this study showing distance from the center of the oil body (indicated by well 421) and elevation. The different symbols indicate which samples were used in which chemical characterization analyses.

The evolution of the oil plume resulted in the spatial progression of the TEAPs over several decades, extending the anoxic region from about 60 m in 1987 to almost 120 m in the 2010s (Cozzarelli et al., 1990; Cozzarelli et. al, 2016). Anaerobic biodegradation in the hydrocarbon plume has been dominated by Mn(IV) and Fe(III) reduction and methanogenesis (Jones et al., 2023). Initial anaerobic biodegradation was almost entirely coupled to Mn(IV) reduction, resulting in concentrations of Mn above 8000 µg/L 70 m downgradient from the oil body (Bennett et al., 1993; Appendix A). Previous research suggests that the majority of reducible Mn(IV) oxides and hydroxides were reduced by 1984 and mobilized as a Mn^{2+} plume in the aquifer (Baedecker et al., 1993). Due to limited Mn(IV) mass in aquifer sediments, Mn(IV) reduction capacity was limited, giving way to Fe(III) reduction (Tuccillo et al., 1999). Fe(III) oxides are present in higher concentrations in native sediment (3.0-7.6%) than Mn(IV) oxides (0.07-0.09%), and are therefore the dominant repository for oxide reduction (Berndt, 1987). Zachara et al. (2004) report total Fe content at approximately 1%. Methanogenesis evolved after the reduction of Fe(III) and Mn(IV) occurred. The lack of SO_4^{2-} and NO_3^- in the aquifer means that reductions of these species are not major TEAPs in the Bemidji aquifer (Baedecker et al., 1993).

Table 1. Redox reactions for the oxidation of benzene. Adapted from Ng et al. (2014), Jones (2020), and Cozzarelli et al. (2016).

Redox Condition	Equilibrium Reaction	Electron Acceptor	Effects
Aerobic Degradation	$C_6H_6 + 7.5O_2 + 3H_2O \rightarrow 6HCO_3^- + 6H^+$	DO	Anoxia, increased acidity, increased alkalinity
Mn(IV) Reduction	$C_6H_6 + 14MnO_2\ (s) + 24H^+ \rightarrow 6HCO_3^- + 15Mn^{2+} + 12H_2O$	Mn^{2+}	Dissolved Mn, dissolved trace elements

Fe(III) Reduction	$C_6H_6 + 30Fe(OH)_3$ (s) + $54H^+$ → $6HCO_3^- + 30Fe^{2+} + 72H_2O$	Fe^{3+}	Dissolved Fe, dissolved trace elements, reduced acidity, increased alkalinity
Methanogenesis	$C_6H_6 + 6.5H_2O$ → $2.25HCO_3^- + 3.75CH_4 + 2.25H^+$	CO_2	Increased acidity

With the slow advancement of the plume due to biodegradation, the redox zones have effectively migrated downgradient through time. By the early 1990s, the anoxic plume extended to 80 m downgradient of the oil body (Cozzarelli et al., 1990). Anoxic plume spreading is evident in DO depletion and increases in dissolved Mn^{2+}, Fe^{2+}, and CH_4 (Baedecker et al., 1993). By 1995, the overall plume shape remained the same, but the anoxic front advanced downgradient and a plume of dissolved Fe(II) had increased in size and concentration (Cozzarelli et al., 2001). The rate of hydrocarbon plume advancement was calculated as 8 m/yr between 1987 and 1992, but slowed substantially to 7 m/yr between 1992 and 1995 (Cozzarelli et al., 2001; Tuccillo et al., 1999). By 2016, the rate of advance was 1.67 m/yr (Cozzarelli et al., 2016).

Trace elements that have been mobilized, transported downgradient, and resorbed or precipitated in the presence of DO are at risk of re-mobilization as the plume and redox zones evolve. For example, As sorbs to Fe(III) oxides in the transition zone between the Fe-reducing sediment and the suboxic sediment (Ziegler et al., 2017). However, as the hydrocarbon plume and redox zones continue to expand based on the rate of plume advancement, these transition zone sediments dissolve and remobilize As and Fe(III) into the aquifer (Ziegler et al., 2017). However, the slowing rate of plume progression indicates that the plume will achieve its maximal extent soon. In a decadal comparison based on 2022 field data, the extent of the 10 µg/L benzene plume retracted from 136 m to 120 m downgradient (Cozzarelli, personal communication). This

phenomenon was first predicted in a numerical model by Ziegler et al. (2021), whose model projections indicated that while the hydrocarbon and Fe plumes retract back toward the oil body, trace elements remain in groundwater and continue to advance downgradient.

In the modern-day plume and for the purposes of discussion in the remainder of this study, the following three zones have been established based on distinct geochemical activity observed within the plume (Figure 2). The methanogenic zone extends from the oil body to 55 m downgradient from the oil body, wherein methanogenesis is the primary redox condition following the depletion of O_2, Fe(III) oxides and hydroxides, and Mn(IV) oxides and hydroxides as electron acceptors (Jones et al., 2023). Further downgradient, the Fe-reducing zone extends from about 85 m to 125 m from the oil body. In the Fe-reducing zone, O_2 has been depleted, but oxide and hydroxide minerals remain in high enough concentration to serve as electron acceptors for reduction. Jones et al. (2023) identified the interface between the methanogenic and Fe-reducing zones as a hotbed of geochemical activity, distinct from the behavior of either adjacent zone. As such, this interface zone was identified as its own entity for the purposes of this research, defined between 55 and 85 m downgradient from the oil body.

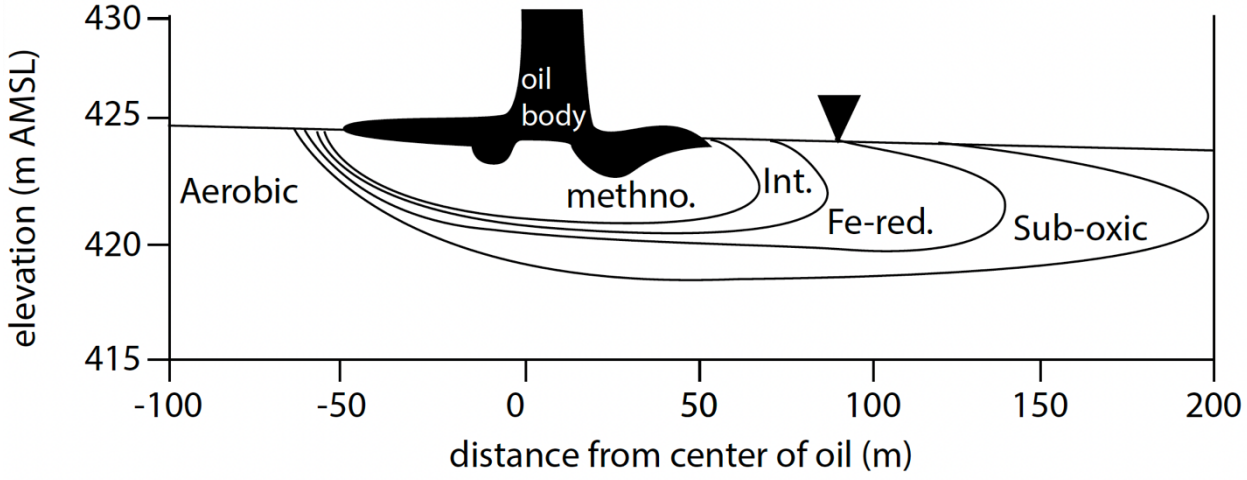

Figure 2. Cross section of the Bemidji aquifer indicating geochemical zone distribution within the aquifer. The direction of groundwater flow is left to right. The triangle indicates the water table.

Previous studies as early as 1985 examined the mobilization and later resorption outside the plume of Ca, Mg, Na, Al, silica, bicarbonate, K, Fe, Mn, V, the concentrations of which were all higher in plume than they were 178 m downgradient of the oil body (Berndt, 1987; Siegel et al., 1985). However, a contemporaneous investigation of sediments was unable to link these metals to mineralogic origins. Multiple studies have documented the trace metal contamination both in the modern-day plume and throughout the plume's historical evolution (Appendix A, which documents reported trace element chemistry from multiple wells in 1986, 2011, and 2021). Recent analyses of sediments in the methanogenic zone, nearest the oil source, have shown that Co, Ni, As, Sr, and Ba are stripped from the sediment, forming co-occurring trace element plumes in the groundwater (Jones et al., 2023). Fe-reduction and methanogenesis are the dominant redox reactions at the spill site, and are summarized in Table 1. Cations are resorbed by sediment in the methanogenic/Fe-reducing interface, while As remains mobilized until the transition zone between Fe-reduction and suboxic conditions (Jones et al., 2023). Ziegler et al. (2017) identified associations between As and Fe in the Bemidji aquifer sediments, with the majority of As (53-80%) sorbing to mineral surfaces. Ni and Co also likely sorb to Fe hydroxides, so they are similarly mobilized during Fe reduction. Additionally, Ba and Sr have been mobilized into trace element plumes in the groundwater (Lacey, 2021).

The processes controlling trace element mobilization and attenuation are underexplored at sites contaminated by organic carbon. At the Bemidji research site, the mineralogic origins, dissolution mechanisms, transport, and attenuation of geogenic contaminants are poorly characterized. At other organic-impacted sites, geogenic contaminants often go unconsidered. While some studies have focused on particular trace elements, they have been narrower in scope and limited to bulk mass characterizations in sediment (Berndt, 1987; Ziegler et al., 2017a).

Furthermore, prior studies often occur in isolation and fail to create an integrated assessment of the interrelated biogeochemical processes that may enhance or inhibit trace element transport. This study aims to compile a comprehensive analysis of trace element cycling to determine the mineralogic origins of trace elements in sediment, identify the mechanisms that mobilize these trace elements, and identify the geochemical conditions that attenuate trace elements. This improved understanding of trace element cycling will provide more holistic knowledge about the water quality consequences of organic carbon contamination in an aquifer. Further understanding the behavior of geogenic contaminants following the introduction of excess organic carbon aids efforts to remediate secondary contaminants and protect groundwater resource quality.

II. Methodology

Sediment collection, digestion, and chemical analyses

Sediment cores used in this study were collected in 2014, 2015, 2016, 2019, and 2023 along a transect through the center of the north contaminant plume at the National Crude Oil Spill Fate and Natural Attenuation Research Site near Bemidji, MN (Figure 1). Cores taken from 201 m upgradient from the spill site were used to characterize background conditions of sediment and trace elements. Cores were obtained using a hollow-stem auger to drill to 0.3 m below the water table, then the piston core barrel was pounded into sediment 2.1 m below the augers. Liquid CO_2 was used to freeze the cores while in the ground to preserve the redox conditions of the sample (Murphy & Herkelrath, 1996). Once removed, core ends were wrapped in plastic and cut. Visual observations of change in sediment color and texture denoted the subsections into which the cores were cut. Core segments were frozen on dry ice and shipped to the lab at Trinity University where they were kept frozen until sampled. Within a given core, samples were taken at a variety of

locations throughout the core to investigate the influence of the hydrocarbon plume at different depths.

SEM-EDX Analyses

As part of a larger project investigating the sediment-bound distribution of Ba, Sr, Co, and Ni, sediment from the background, methanogenic zone, interface zone, and Fe-reducing zone were analyzed for the association of trace elements with carbonates, Fe(III)-hydroxides, and silicates (Jones et al., 2023). Wet sediment was dried under anoxic conditions in a nitrogen atmosphere Coy anaerobic chamber (95% N_2, 5% H_2) to best maintain redox conditions. One gram of dried sediment was transferred to a centrifuge tube with isopropanol. The tube was sonified and suspended particulates in the supernatant were collected using a transfer pipette and filtered using vacuum filtration (0.45 μm filter pore size) to remove secondary mineral coatings off the coarser detrital minerals. A repeat wash of the sediment sample with isopropanol was conducted. The dried powder-like sediment was mounted on a cylindrical stub using PELCO Tabs (TM) Carbon Conductive Tabs for SEM analysis. I examined the composition and surface morphology of mineral coatings on a Jeol JSM-6010LA scanning electron microscope (acceleration voltage = 15.0 kV, working distance = 10-12, magnification = x3500 to x4000) at Trinity University. EDX mapped the major elemental composition of the sample, from which we identified mineral composition and used point analyses to examine the association of the aforementioned trace elements with given mineral types.

Sequential Chemical Extraction Procedure

Fifty-five sediment samples were digested following a sequential extraction procedure modified from Tessier et. al (1979) to elucidate the origins of 30 trace elements from sediment phases. We used a set of eight samples from a single core in the background sediment, 12 samples from two cores in the methanogenic zone sediment, 19 samples from two cores in interface zone sediment, and 16 samples from two cores in Fe-reducing sediment. From each sample, 0.500 g of sediment was measured and allowed to air dry in anaerobic chamber, while oxic background samples were dried in a convection oven at 40°C. Samples were ground with a mortar and pestle and grains larger than two mm were removed. Dried sediment was sequentially reacted with extraction solutions to provide insight into the following operationally defined phases: surface exchangeable ions, carbonate minerals, readily reducible oxides and hydroxides, and organic matter. The extraction steps were:

1. Surface exchangeable ions: 4 mL of 1 M $MgCl_2$ (adjusted to pH 7 with 5% NaOH) was added to sample and rotated on an end-over-end mixer for one hour. The samples were then centrifuged (8500 RPM, 30 minutes) and decanted into a centrifuge tube. 5 mL of deionized (DI) water were added to the sample, vortexed for one minute, centrifuged for 30 minutes, and then was decanted into the same centrifuge tube.
2. Elements bound to carbonates: 4 mL of 1 M NaOAc (adjusted to pH 5.0 with HOAc) was added to the sediment tube and mixed end-over-end for 5 hours. Afterwards, the same steps of centrifuging, decanting, washing, and decanting were repeated.
3. Elements bound to reducible oxides and hydroxides: 10 mL of 0.04 M hydroxylamine HCl in 25% (v/v) HNO_3 was added to sediment tubes. Tubes were placed in hot water baths around 96°C for 6 hours, with occasional manual agitation. Afterwards, the centrifuging, decanting, and cleansing steps were repeated.

4. Elements bound to organic matter: 1.5 mL of 0.02 HNO_3 and 2.5 mL of 30% H_2O_2 were added to the sediment tubes. Tubes were placed in a hot water bath at about 85°C for 2 hours with occasional manual agitation. A second aliquot of 1.5 mL H_2O_2 was added and was placed back in hot water bath for 3 additional hours with occasional agitation. Samples were allowed to cool to room temperature, and then 2.5 mL of 3.2 M NH_4OAc/HNO_3 and 2 mL DI water were added and mixed in end-over-end mixer for 30 minutes. Centrifuging, decanting, and cleansing steps were repeated.

Resulting extractants from each phase were sent to USGS (Reston, VA) and analyzed using inductively coupled plasma-mass spectrometry (ICP-MS) and inductively coupled plasma-optical emission spectroscopy (ICP-OES) to quantify concentrations of trace elements (Ag, As, B, Ba, Be, Cd, Ce, Co, Cr, Cu, La, Li, Mn, Mo, Ni, Pb, Rb, Sb, Se, Sr, Tl, U, Zn) and major and minor elements (Al, Ca, Fe, K, Mg, Na, Si), respectively.

Statistical analyses of sequential extraction data

ICP-MS and ICP-OES data were obtained from USGS (Reston, VA). Sequential extraction ICP-MS and ICP-OES data of 30 trace elements were calculated in milligrams of element per kilogram of sediment by zone. Sixteen elements were reported only on ICP-MS (Ag, As, Be, Cd, Ce, Co, Cr, La, Mo, Ni, Pb, Rb, Sb, Se, Tl, U) and five were reported only on ICP-OES (Ca, K, Mg, Na, Si). For nine elements, both were reported (Al, B, Ba, Cu, Fe, Li, Mn, Sr, Zn). These datasets were consolidated using the following framework:

- If the value of MS was greater than the upper limit of detection, use OES value if available
- If the value of OES was less than the lower limit of detection, use MS value if available
- If both were measurably reported, use MS value

- If the only value available is less than the lower limit of detection, report the value as half the analytical detection limit
- If the only value available is above the upper limit of detection, estimate by reporting at the upper limit

Analytical values were then converted from µg/L and mg/L to mg element/kg sediment based on the sediment mass in the extracted sample and the volume of extractant used. Elements for which 10% of samples were below the ICP-MS detection limit were removed from further analysis.

Shapiro-Wilk tests were conducted using RStudio on each phase of the eighteen elements analyzed in the stacked bar charts to determine if the data for a given element within a given phase was normally distributed. If the data were not normally distributed, a second Shapiro-Wilk test was run to determine if the data were log-normally distributed.

Kruskall-Wallis non-parametric one-way analysis of variance tests were employed to identify if statistically significant differences existed between at least one of the four geochemical zones for a given element in a given mineral phase. If the p value was less than 0.05, indicating a significant difference in elemental concentration between at least two zones, Pairwise Wilcoxon tests were used to identify the zones between which there was a statistically significant difference. Pairwise Wilcoxon tests were conducted in RStudio with a Bonferroni correction.

A matrix constructed from the values in the Pairwise Wilcoxon tests was used to compare commonalities between trace element mobilization and sequestration patterns between zones. For an overall understanding of the similarities between elemental cycling in the three mineral phases across the four geochemical zones, the output from the Wilcoxon signed rank tests was used to create a unique "fingerprint" for each element (Appendix B). For a given element in a specific extraction phase (e.g., Mg in carbonates), comparisons between geochemical zones were

evaluated. If zone x was statistically greater than zone y based on a Wilcoxon signed rank test, the matrix cell comparing zones x and y was denoted with a 1 (e.g. see Background vs. Methanogenic in carbonates for Mg in Figure 3). If zone x was statistically less than zone y, the cell was denoted with a -1 (e.g. see Fe-reducing vs. Interface in organics for Mg in Figure 3). Matrix cells between zones were left null if no significant difference was observed. This process was then repeated for the additional two phases for the same element.

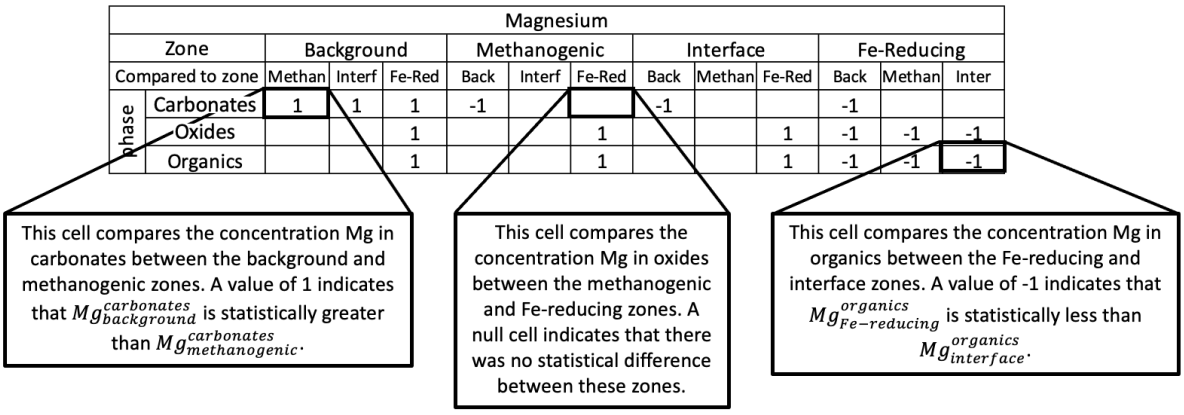

Figure 3. Each cell in the fingerprint matrix can be read as comparing the concentration of an element (e.g. Mg) in the "zone" row to the zone in the "compared to zone" row for the phase listed in the leftmost column. If a value of 1 is placed, the "zone" concentration is greater than the comparison zone concentration for that phase. A value of -1 indicates that the comparison zone has a greater concentration than the "zone" concentration for that phase. A null cell indicates no statistically significant difference between the zones.

Each element's fingerprint matrix was then compared to all other elements' matrices to evaluate commonalities in statistically significant differences. One element was chosen as the reference element (e.g., Mg), and then evaluated with respect to all other comparison elements. Then a new element (e.g., Ca, Mn) was denoted as the reference element and evaluated across all other comparison elements (Figure 4).

In comparing the similarity between the reference element and the comparison element, if the same statistical change was observed for a phase between two zones (i.e., the same cell in both

fingerprint matrices was demarcated as both 1 or both -1), an output matrix was flagged as 1 for that zone-to-zone comparison for that mineral phase (Figure 4). If one element showed a statistical increase between zones while the other element showed either a statistical decrease or no significant difference between those same zones, the cell in the output matrix was flagged as 0. The total number of similarities between the two elements (i.e., the total number of ones in the comparison matrix) was summed and divided by the total number of significant differences flagged in the fingerprint matrix for the reference element, resulting in a correlation between the reference element and the comparison element, whereby zero indicates no correlation and one indicates perfect correlation.

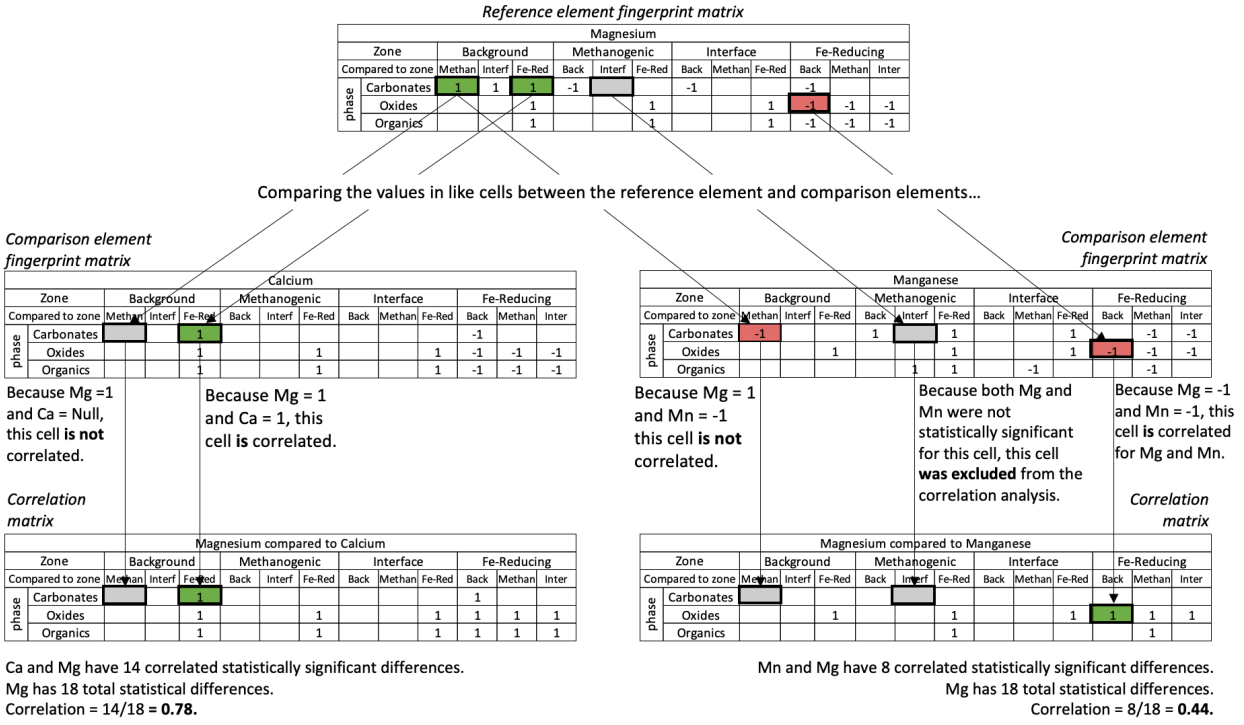

Figure 4. If a given comparison cell from one fingerprint matrix corresponds with the same value (e.g. both 1 or both -1) with the same comparison cell in another fingerprint matrix, the cells were considered to be correlated. If the cells did not contain the same value (e.g. 1 with -1, 1 with null), the cells were not correlated. If both cells were null, the cell was excluded from the analysis. The number of shared significant differences between two fingerprint matrices was summed, then divided by the total number of significant cells for one of the two elements to yield a correlation value.

Principal component analysis (PCA) is a dimensionality reduction model that identifies the two main forms of variability in a multivariate data set for the interpretation of the user. Numerous sources of variability can be reduced into principal components, which indicate the main sources of variability. This process can eliminate causes of data variation that are noise/not important to the data analysis. In a PCA biplot, principal component 1 (PC1) is plotted along the x-axis and represents the main source of variability. Principal component 2 (PC2) describes the second-largest source of variability/second largest spread of data, and is independent (and therefore perpendicular) to PC1. PC2 is plotted along the y-axis in a PCA biplot. Data points are plotted in the PC space with variable vectors pointing outwards from the origin. The directions of the vectors define what axes the variable influences, and the length of the vector represents the degree of influence on an axis.

To construct PCA biplots, each dataset in mg element per kg sediment for a given phase was log-normally distributed, then normalized from 0 to 1 to rank the values. Elements that were previously removed from analysis were not included in the PCA biplots. No exchangeable phase biplot was created due to insufficient data. For elements that did not have sufficient data, PCA biplots were constructed in RStudio using the ggplot2 packages ggfortify and ggrepel. The plotted samples in the biplot were colorized by zone on one iteration and by depth in the second iteration.

Characterizing organically complexed elements

Alkaline pH extractions were conducted at Trinity University to target organically bound trace metals in sediment. Alkaline organic extraction methods were adapted from that of Swift (1996). Sediment samples were dried in a Coy anaerobic chamber with a nitrogen atmosphere (95% N_2, 5% H_2). Dried samples were crushed with a mortar and pestle, and grains larger than

2.0 mm were removed. Five to ten g of sediment were reacted with 0.5 M NaOH at a ratio of 1 g/5 mL in a 50 mL centrifuge tube. Suspension was agitated on an orbital shaker for 48 hours, with occasional manual agitation, after which the sediment and extractant were separated by centrifuging (8500 RPM) for thirty minutes. The samples were then sealed under a nitrogen atmosphere, wrapped in parafilm, frozen, and shipped to Auburn University on ice.

High-performance liquid chromatography (HPLC) (1200 HPLC Quaternary Pump, Agilent, USA) equipped with two size exclusion columns (SEC) (Protein-Pak 125, 10 µm, 7.8 x 300 mm, Waters, USA) and coupled to ICP-MS (Agilent 7900 Quadrupole, USA) was used to determine the molecular weight distribution of organic matter and associated trace elements in sediment. Prior to the installation of SEC columns, a guard column (PL Aquagel-OH GPC/SEC Guard Column, 8 µm, 50 x 7.5 mm, Agilent, USA) was installed. The HPLC-SEC-ICP-MS used ammonium nitrate (0.01 M) solution as the mobile phase, operating in no gas mode at a flow rate of 1 mL/min. The injection volume was 100 µL. Arsenic standards, ranging from 5 to 100 ppb, were run for HPLC-SEC-ICP-MS. The HPLC-SEC-ICP-MS methodology is further detailed in Ojeda et al. (2023). Resulting data was normalized to identify the retention times of organic matter.

HPLC-SEC (1200 HPLC Quaternary Pump, Agilent, USA) with fluorescence (FLD) and variable wave (VWD) detectors were used with the same guard and SEC columns as the HPLC-SEC-ICP-MS, a flow rate of 1 mL/min, and a sample injection volume of 100 µL. The mobile phase was ammonium nitrate (0.01 M) solution. Polystyrene sulfonate standards ranging from 1600 to 15,800 Da were run with acetone (48 Da) and guanosine (283 Da) to create a calibration curve of molecular mass with retention time. UV detectors were run at 254 nm, while FLD detectors were at 260/450 nm.

Parallel Factor Analysis

Parallel factor analysis (PARAFAC) allows for the decomposition fluorescence excitation-emission matrices (EEMs) into chemical constituents (Murphy et al., 2013). Fluorescence analyses can provide detailed information on organic matter in order to identify organic matter type or functional groups present. Samples were analyzed on an Agilent Cary UV-Vis spectrometer at wavelengths ranging 200 to 800 nm. Samples were subsequently diluted to achieve an absorbance at 254 nm less than 0.2. Excitation and emission wavelengths of the extractants from the alkaline extractions were measured on a FP-8500 spectrofluorometer (JASCO, USA) at Auburn University to determine the maxima of excitation and emission for a given sample. Samples were measured in a 10 mm quartz cuvette. Prior to PARAFAC modeling, a blank subtraction was conducted and resulting excitation and emission spectra were corrected. Raman normalization was employed to correct for Rayleigh scattering. Values were normalized to 254 nm for UV-Vis. PARAFAC was conducted using the drEEM toolbox on RStudio, supplemented by the stardom package to spectroscopically analyze dissolved organic matter in RStudio (Pucher, 2023).

III. Results

SEM-EDX Analyses

Results from SEM-EDX point analyses were previously published in Jones et. al (2023), but are expanded upon here. I collected SEM-EDX data for four trace elements: barium (Ba), cobalt (Co), nickel (Ni), and strontium (Sr) (Figure 5) in accordance with that project's objective (Jones et al., 2023). Although these trace elements are present in only trace amounts in bulk sediment, the separation of secondary precipitates from detrital minerals effectively concentrates

elements into the lower percent range needed to quantify partitioning between different minerals and in different geochemical zones. In the background sediments, all cations are present at appreciable weight percent in the minerals, either via sorption to the surface or incorporated into the mineral lattice of the examined carbonates and Fe(III) hydroxides. Sr occurs at a greater concentration with silicate minerals than carbonates or Fe(III) hydroxides, but is still present in the other mineral phases. In the methanogenic zone, long-term biodegradation has mobilized the majority of trace element masses from the sediment, resulting in low (but detectable) trace element associations with silicates and Fe(III) hydroxides. Ba, Co, and Ni did not experience the same degree of mobilization from the carbonates because most carbonates are insensitive to decreases in redox potential compared to the other mineral types. In fact, the medians for Ba, Co, and Ni all increased in methanogenic carbonates compared to background sediments. In the interface zone between the methanogenic and Fe-reducing zones, the concentration of Ba, Co, and Ni associated with carbonates decreased slightly, while silicate association remained similar. Co and Ni increased relative to the methanogenic zone in association with Fe(III) hydroxides in the interface zone, while Ba decreased slightly. Sr concentrations in the interface remained low in carbonates and silicates, with a slight increase in Fe(III) hydroxides.

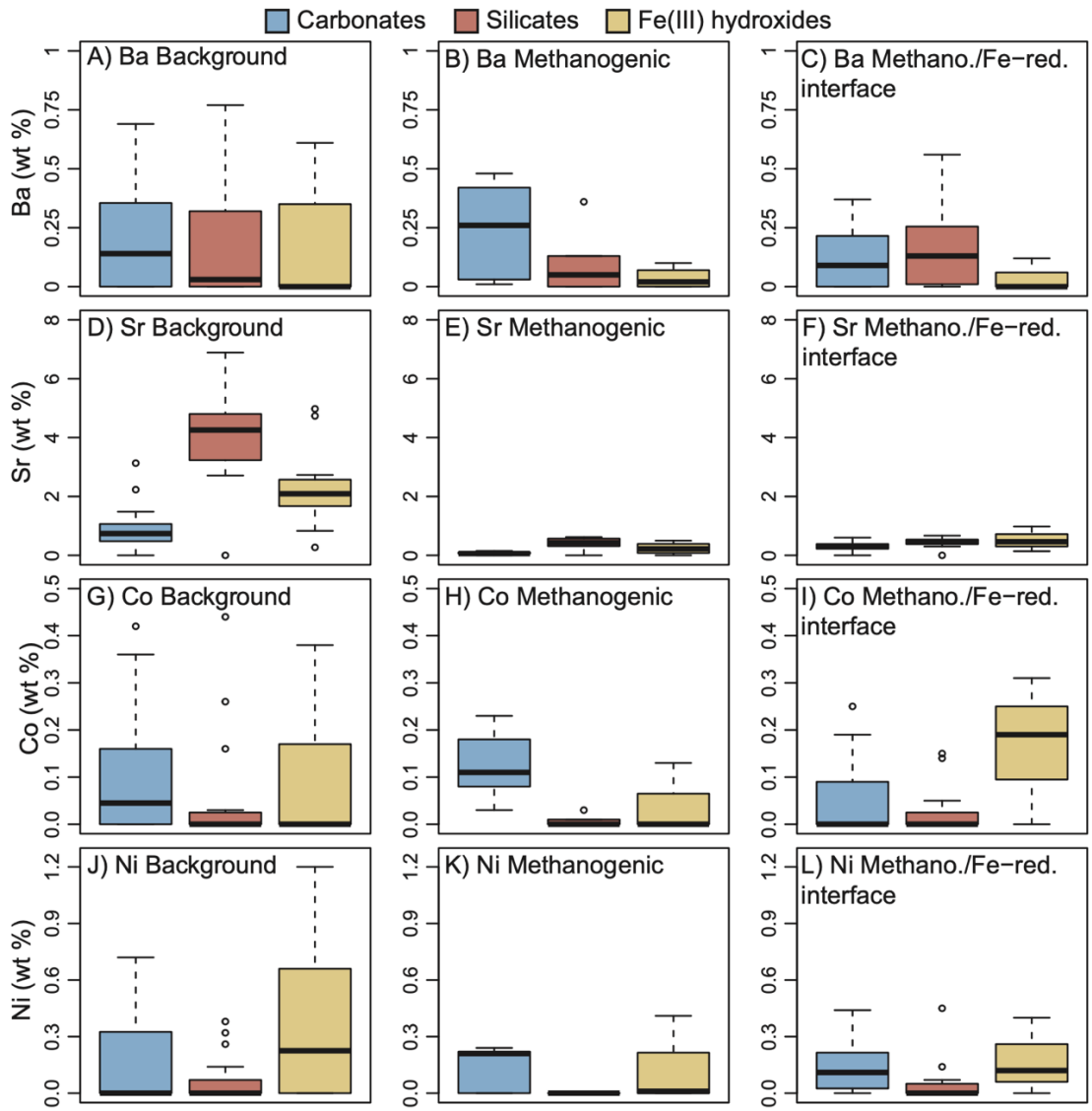

Figure 5. Boxplots of EDX point analysis data in sediments organized by zone, with the background on the left, the methanogenic zone in the center, and the interface zone on the right. Boxplots show the wt % of Ba (top row), Sr (second row), Co (third row), and Ni (bottom row) in sediment, with carbonates in blue, silicates in red, and Fe(III) hydroxides in yellow. Figure originally published in Jones et al. (2023).

Sequential Extraction Stacked Bar Charts

Twelve elements (silver (Ag), beryllium (Be), cadmium (Cd), lithium (Li), potassium (K), molybdenum (Mo), sodium (Na), rubidium (Rb), antimony (Sb), selenium (Se), thallium (Tl), and uranium (U)) were eliminated from further analysis because less than 10% of data were above the

detection limit. Furthermore, the surface exchangeable phase has minimal reported data resulting from salts precipitating on the ICP-MS inlet during analysis of $MgCl_2$ extractants. The elements for which exchangeable data were not reported are arsenic (As), cerium (Ce), cobalt (Co), chromium (Cr), lanthanum (La), magnesium (Mg), nickel (Ni), and lead (Pb).

Sediments in the background and plume had similar concentrations of aluminum in each of the four measured phases, with one anomalous organic peak in the methanogenic zone. The average values for a given phase within a given zone are reported, followed by the interquartile range for the same dataset (Table X).

Table 2. Mean values and interquartile range values (in italics) for a given element within a phase and zone. All values are in mg element per kg sediment.

	Exchangeable				**Carbonates**				**Oxides & Hydroxides**				**Organics**			
	Bkg.	Met.	Int.	FeR.	Bkg.	Met.	Int.	FeR.	Bkg.	Met.	Int.	FeR.	Bkg.	Met.	Int.	FeR.
Al	43.7	44.1	44.2	44.1	12.3	9.0	8.5	11.1	109.6	115.7	108.0	117.2	45.0	80.8	60.0	60.0
	2.9	*0.9*	*27.3*	*1*	*3.8*	*1.5*	*1.6*	*2.7*	*22.9*	*0*	*27.1*	*0*	*23.5*	*0*	*0*	*0*
As	-	-	-	-	0.45	0.45	0.48	0.45	0.60	0.60	0.69	0.80	0.08	0.60	0.15	1.37
					0.00	*0.00*	*0.00*	*0.00*	*0.00*	*0.00*	0.00	*0.31*	*0.00*	*0.14*	*0.15*	*1.11*
B	17.5	17.6	17.7	17.6	2.6	1.7	1.2	2.5	2.3	4.8	2.1	3.5	0.3	1.0	0.3	0.9
	1.2	*0.4*	*0.4*	*0.4*	*0.1*	*0.3*	*0.1*	*0.2*	*0.9*	*0.4*	*0.6*	*0.7*	*0.0*	*0.9*	*0.0*	*0.3*
Ba	17.5	17.6	17.7	17.6	9.4	6.3	6.6	4.8	8.1	6.7	4.2	5.0	1.1	2.1	1.6	1.3
	1.2	*0.4*	*1.3*	*0.4*	*4.4*	*1.9*	*2.7*	*1.1*	*5.5*	*1.8*	*1.3*	*1.3*	*1.2*	*0.8*	*0.5*	*0.2*
Ca	652	1,085	1,009	1,026	19,285	13,312	11,594	11,737	12,754	8,325	9,013	4,131	492	366	402	249
	54	*466*	*1,164*	*126*	*10,503*	*1521*	*2,088*	*2,516*	*10,058*	*2,228*	*5,055*	*1,236*	*208*	*116*	*109*	*66*
Ce	-	-	-	-	1.2	1.5	1.6	1.3	3.4	3.3	3.3	2.3	0.4	1.3	0.8	0.4
					0.2	*0.4*	*0.6*	*0.2*	*1.0*	*1.0*	*1.7*	*0.6*	*0.0*	*1.0*	*0.5*	*0.1*
Co	-	-	-	-	0.2	0.2	0.2	0.1	1.4	0.8	0.7	0.5	0.1	0.1	0.1	0.1
					0.2	*0.1*	*0.1*	*0.1*	*1.4*	*0.3*	*0.2*	*0.1*	*0.0*	*0.0*	*0.0*	*0.0*
Cr	-	-	-	-	0.17	0.18	0.18	0.17	0.68	0.73	0.69	0.84	0.18	0.35	0.28	0.43
					0.03	*0.01*	*0.02*	*0.02*	*0.09*	*0.09*	*0.10*	*0.14*	*0.09*	*0.10*	*0.07*	*0.06*
Cu	17.46	17.63	17.68	17.63	3.17	2.59	3.56	2.84	2.97	4.81	2.01	4.27	0.15	0.28	0.23	0.21
	1.19	*0.36*	*8.95*	*0.38*	*0.70*	*0.56*	*2.22*	*0.91*	*0.92*	*0.98*	*1.49*	*2.13*	*0.12*	*0.12*	*0.09*	*0.07*
Fe	8.7	8.8	8.8	8.8	8.8	93.2	124.8	67.2	1779.0	1001.5	1122.8	1147.7	11.8	27.6	21.6	20.8
	0.6	*0.2*	*0.0*	*0.2*	*3.6*	*50.9*	*106.8*	*66.4*	*226.5*	*148.5*	*736.5*	*348.8*	*7.7*	*5.6*	*4.5*	*5.3*
La	-	-	-	-	0.85	0.80	0.83	0.73	1.50	1.67	1.62	1.12	0.27	0.98	0.60	0.42
					0.19	*0.19*	*0.20*	*0.12*	*0.43*	*0.55*	*0.88*	*0.30*	*0.20*	*0.61*	*0.32*	*0.14*
Mg	-	-	-	-	2,062	1,289	1,230	1,206	5,973	4,299	4,622	2,141	183	142	144	46
					741	*328*	*442*	*241*	*4,200*	*1,215*	*2,417*	*636*	*95*	*76*	*35*	*1*

Mn	8.7	9.7	9.8	8.8	25.9	64.7	42.5	20.1	121.8	53.8	42.6	12.6	3.0	3.5	2.3	2.0
	0.6	*0.2*	*0.2*	*0.2*	*7.3*	*56.9*	*27.8*	*4.7*	*104.0*	*19.2*	*35.8*	*4.8*	*2.5*	*1.2*	*0.5*	*0.6*
Ni	-	-	-	-	0.66	0.48	0.46	0.32	1.80	1.30	1.29	0.93	0.11	0.30	0.21	0.30
					0.18	*0.15*	*0.23*	*0.07*	*1.30*	*0.39*	*0.58*	*0.20*	*0.03*	*0.06*	*0.16*	*0.10*
Pb	-	-	-	-	0.05	0.27	0.28	0.11	0.98	0.7	0.76	0.59	0.08	0.08	0.08	0.08
					0.00	*0.03*	*0.14*	*0.12*	*0.25*	*0.17*	*0.26*	*0.14*	*0.00*	*0.00*	*0.00*	*0.00*
Si	21.8	22.1	22.1	22.1	22.2	22.2	23.5	22.2	330.6	215.3	240.9	257.6	215.1	174.2	206.8	211.4
	1.5	*0.5*	*4.5*	*0.5*	*0.1*	*0.0*	*0.1*	*0.0*	*52.7*	*20.8*	*78.3*	*34.0*	*64.7*	*32.6*	*18.2*	*20.7*
Sr	21.8	22.1	22.1	22.1	16.8	12.1	11.2	9.5	6.0	6.4	4.2	8.3	0.4	1.0	0.7	0.6
	1.5	*0.5*	*4.8*	*0.5*	*11.0*	*1.7*	*1.8*	*2.4*	*5.4*	*2.5*	*1.8*	*6.8*	*0.1*	*0.6*	*0.6*	*0.4*
Zn	17.46	17.63	17.68	17.63	2.78	2.25	1.68	2.69	4.76	14.22	6.21	7.85	1.08	1.7	1.24	1.45
	1.19	*0.36*	*0.36*	*0.38*	*0.11*	*0.41*	*0.46*	*0.30*	*1.60*	*4.02*	*1.29*	*3.05*	*0.55*	*0.59*	*0.14*	*0.26*

Al associated with mineral phases at similar rates in the background sediment and in the plume sediment, predominantly associated with oxides and hydroxides (Figure 6). There was one anomalously high Al peak in the methanogenic carbonates.

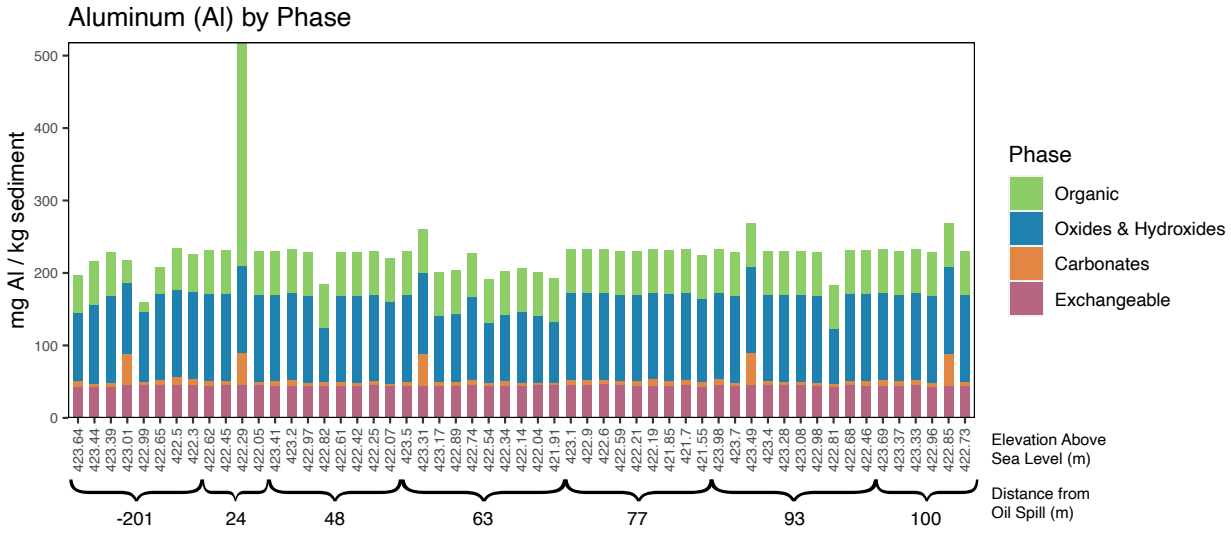

Figure 6. Stacked bar chart of aluminum (Al) by phase based on sequential extraction data. The y-axis displays milligrams of Al per kilogram sediment. The x-axis reports the sample's elevation is reported in m above sea level and the samples are grouped by the core's distance from the oil spill in meters. The organic extraction phase is shown in green, oxides and hydroxides in blue, carbonates in orange, and exchangeable surface ions in pink.

Arsenic was largely below the detection limit of the instruments in the background, methanogenic, and interface zones. However, in the Fe-reducing zone, the values increased notably in the organic phase (Figure 7).

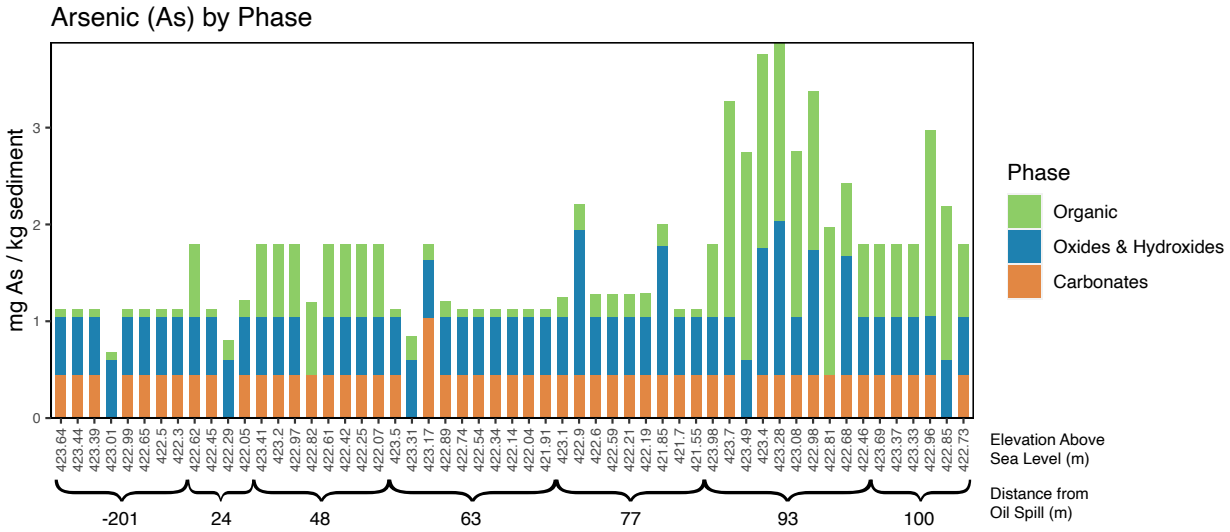

Figure 7. Stacked bar chart of arsenic (As) by phase based on sequential extraction data. The y-axis displays milligrams of As per kilogram sediment. The x-axis reports the sample's elevation is reported in m above sea level and the samples are grouped by the core's distance from the oil spill in meters.

Barium was present in variable concentrations throughout both the plume and background, with some peaks in the plume in the carbonate and oxides and hydroxides phases (Figure 8).

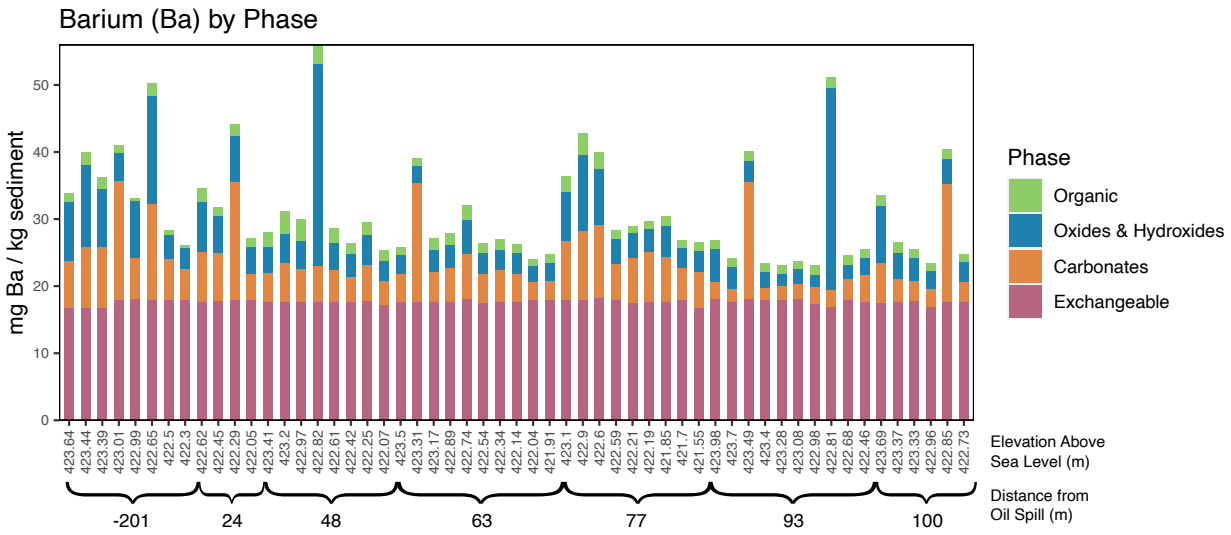

Figure 8. Stacked bar chart of barium (Ba) by phase based on sequential extraction data. The y-axis displays milligrams of Ba per kilogram sediment. The x-axis reports the sample's elevation is reported in m above sea level and the samples are grouped by the core's distance from the oil spill in meters.

Boron was present in variable concentrations throughout both the plume and background (Figure 9). Some likely anomalous peaks were observed in the carbonates and oxides and hydroxides phases. In the exchangeable phase, the majority of samples were at or below the lower detection limit.

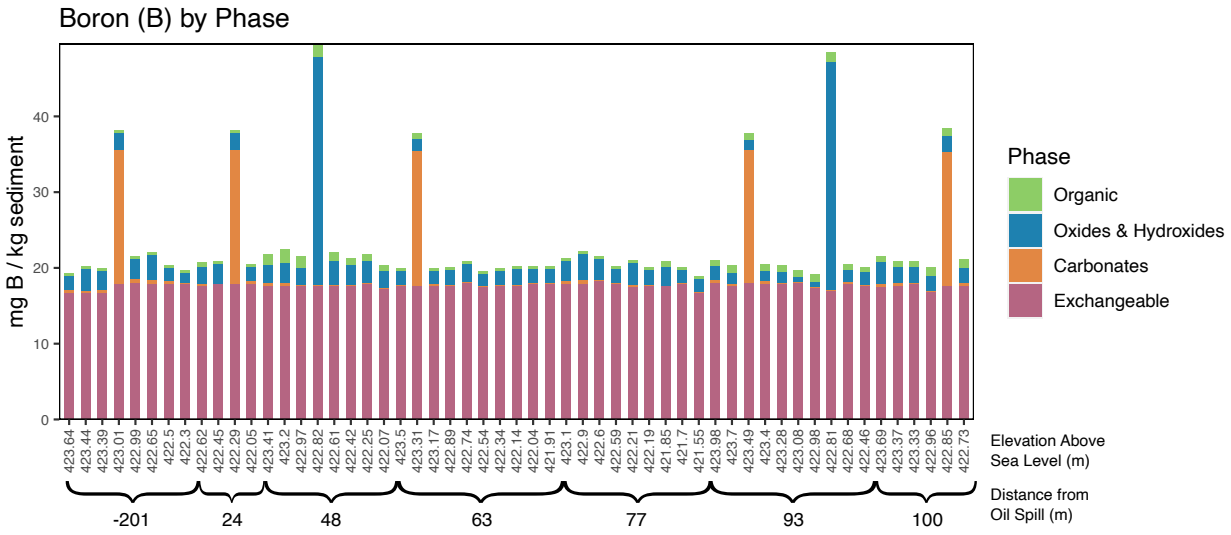

Figure 9. Stacked bar chart of boron (B) by phase based on sequential extraction data. The y-axis displays milligrams of Al per kilogram sediment. The x-axis reports the sample's elevation is reported in m above sea level and the samples are grouped by the core's distance from the oil spill in meters.

Calcium was predominantly present in oxide and hydroxide and carbonate phases throughout both the plume and the background, with a decrease in oxides and hydroxides in the plume body, specifically in the Fe-reducing zone (Figure 10).

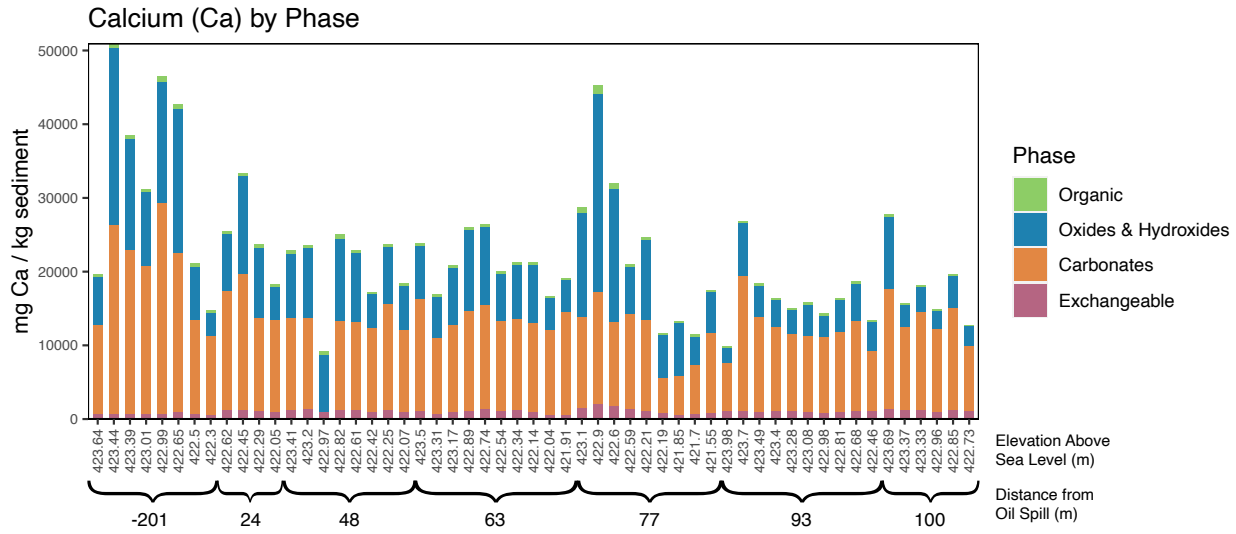

Figure 10. Stacked bar chart of calcium (Ca) by phase based on sequential extraction data. The y-axis displays milligrams of Ca per kilogram sediment. The x-axis reports the sample's elevation is reported in m above sea level and the samples are grouped by the core's distance from the oil spill in meters.

Cerium was present in variable values throughout both the plume and background. In the Fe-reducing zone, both the oxides and hydroxides and organic phases see some depletion (Figure 11).

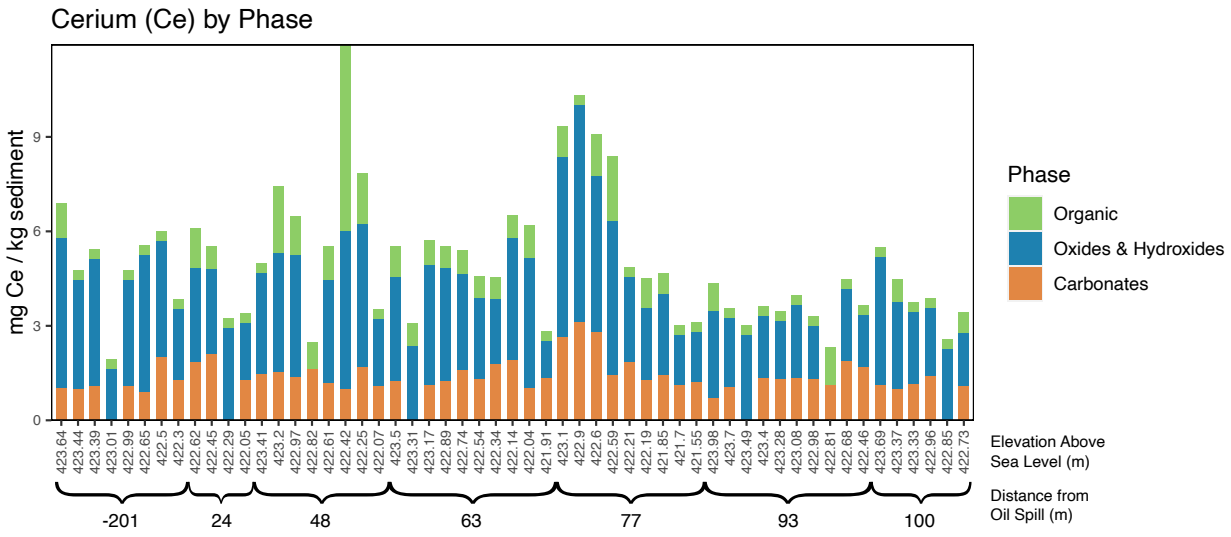

Figure 11. Stacked bar chart of cerium (Ce) by phase based on sequential extraction data. The y-axis displays milligrams of Ce per kilogram sediment. The x-axis reports the sample's elevation is reported in m above sea level and the samples are grouped by the core's distance from the oil spill in meters.

Cobalt was predominantly found in the oxide and hydroxide phases of sediment in both the plume and the background (Figure 12).

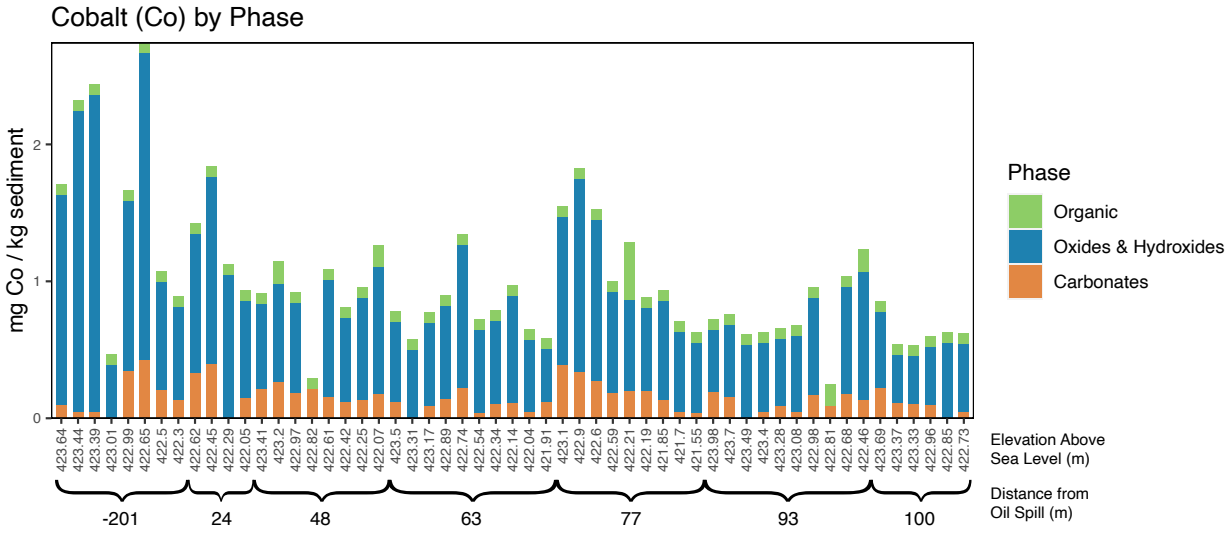

Figure 12. Stacked bar chart of cobalt (Co) by phase based on sequential extraction data. The y-axis displays milligrams of Co per kilogram sediment. The x-axis reports the sample's elevation is reported in m above sea level and the samples are grouped by the core's distance from the oil spill in meters.

Chromium was present in variable amounts throughout both the plume and background (Figure 13). However, the Cr associated with the organic phase increases throughout the plume and Cr associated with oxides and hydroxides increases in the Fe-reducing zone. Little variation in carbonates was observed for Cr.

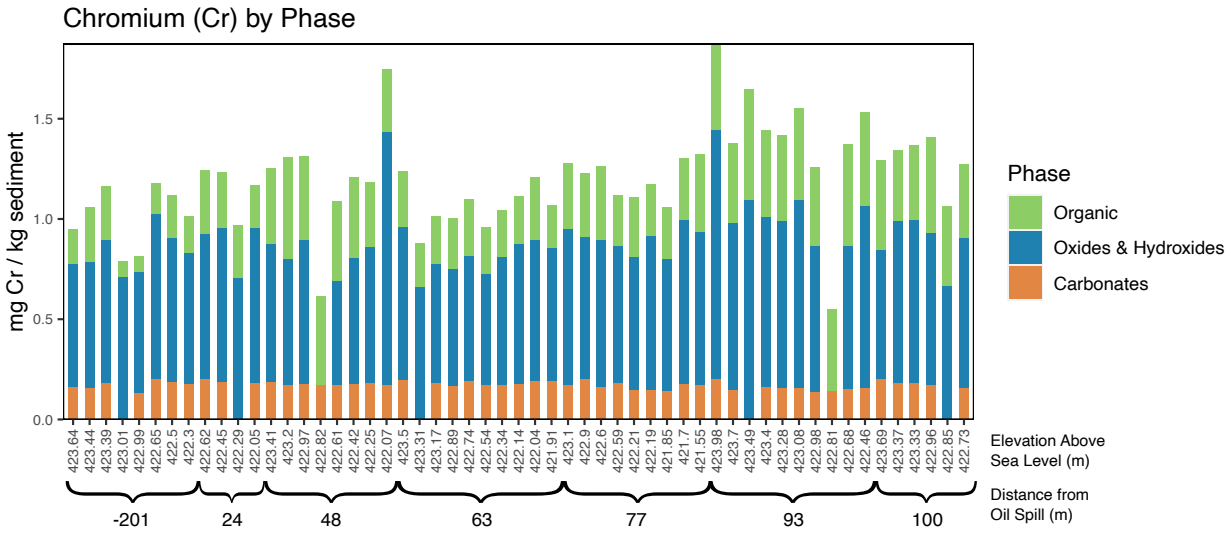

Figure 13. Stacked bar chart of chromium (Cr) by phase based on sequential extraction data. The y-axis displays milligrams of Cr per kilogram sediment. The x-axis reports the sample's elevation is reported in m above sea level and the samples are grouped by the core's distance from the oil spill in meters.

Copper was present in variable amounts throughout the background and plume, with a consistently higher concentration in carbonates in the interface zone (Figure 14). While background and interface carbonates have similar means, this is heavily skewed by one anomalously high Cu carbonate sample in the background.

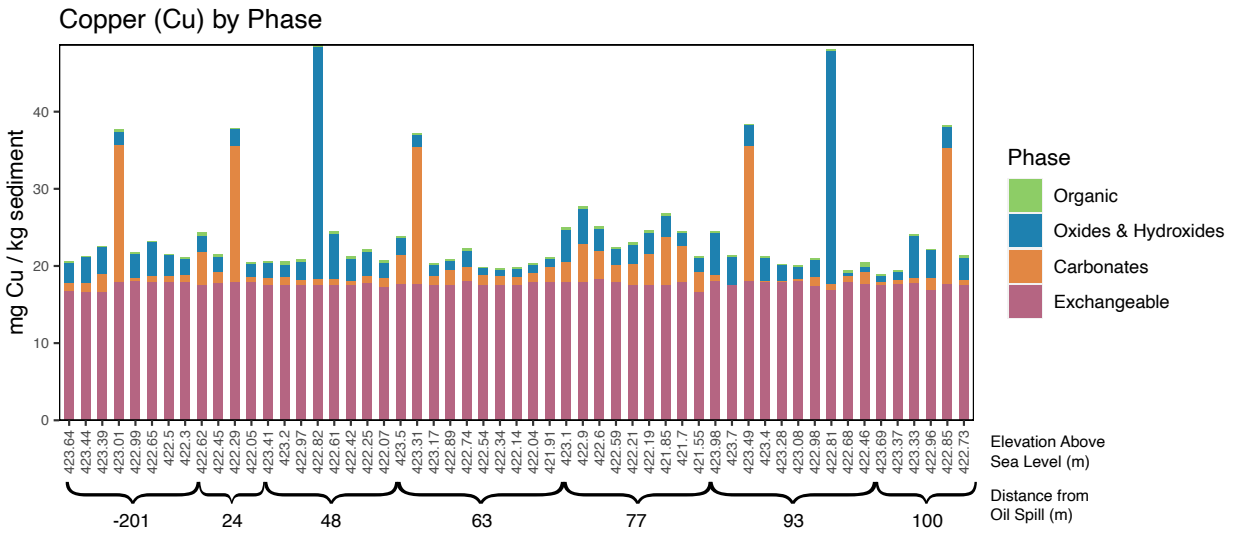

Figure 14. Stacked bar chart of copper (Cu) by phase based on sequential extraction data. The y-axis displays milligrams of Cu per kilogram sediment. The x-axis reports the sample's elevation is reported in m above sea level and the samples are grouped by the core's distance from the oil spill in meters.

Iron was predominantly present in the oxides and hydroxides phase throughout the background and plume, but increased in the carbonate phase throughout the plume (Figure 15). Overall, background oxides had consistently higher Fe than in plume sediments, although plume sediment oxides were sporadic and varied substantially with depth. The Fe concentration in the exchangeable phase was negligible compared to other phases.

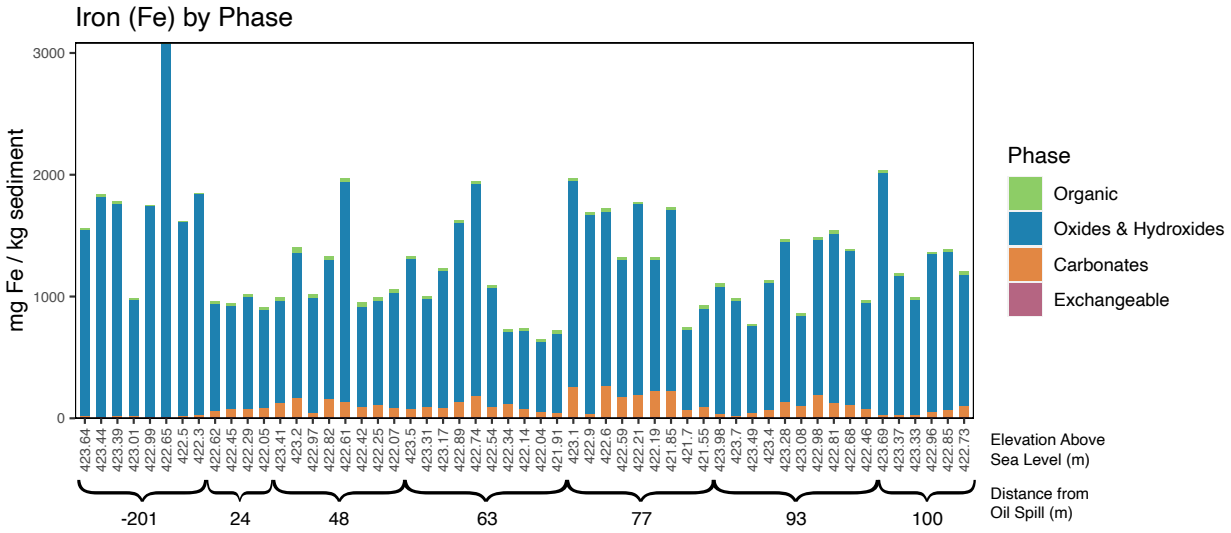

Figure 15. Stacked bar chart of iron (Fe) by phase based on sequential extraction data. The y-axis displays milligrams of Fe per kilogram sediment. The x-axis reports the sample's elevation is reported in m above sea level and the samples are grouped by the core's distance from the oil spill in meters.

Lanthanum was reported in greater concentration in the methanogenic and interface zones than in the background or Fe-reducing zones, with a substantial increase in organic-bound La compared to background sediments (Figure 16).

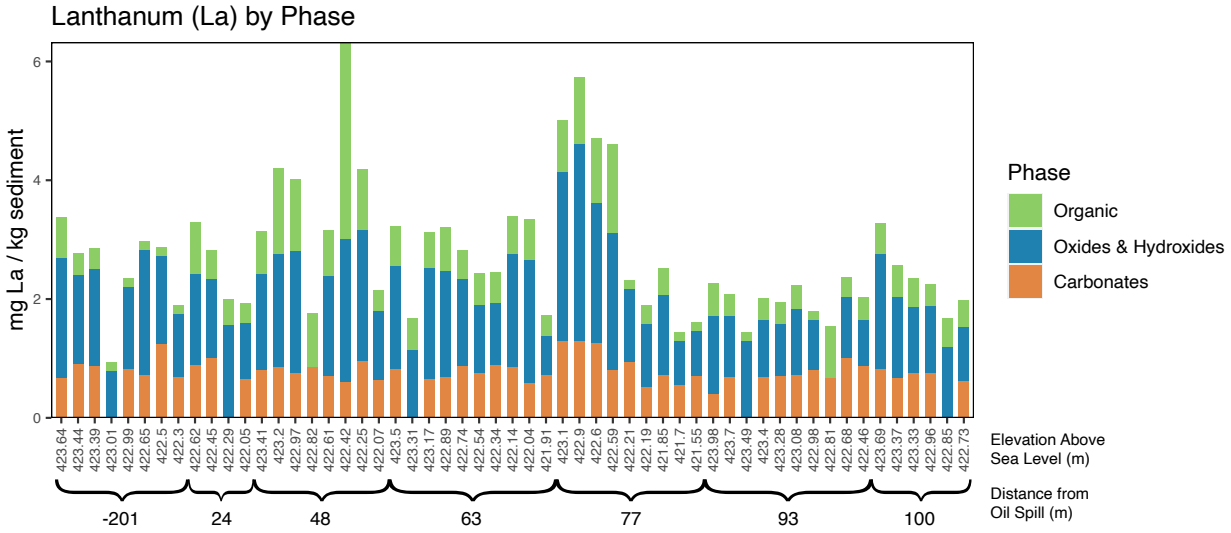

Figure 16. Stacked bar chart of lanthanum (La) by phase based on sequential extraction data. The y-axis displays milligrams of La per kilogram sediment. The x-axis reports the sample's elevation

is reported in m above sea level and the samples are grouped by the core's distance from the oil spill in meters.

Magnesium is overwhelmingly present in oxide and hydroxide phases in both the background and the plume (Figure 17). Values are generally lower in the plume than in the background, with the exception of the upper samples of the core taken at 77 m. An appreciable amount of organic Mg also appears in background sediments and are generally lower in the plume.

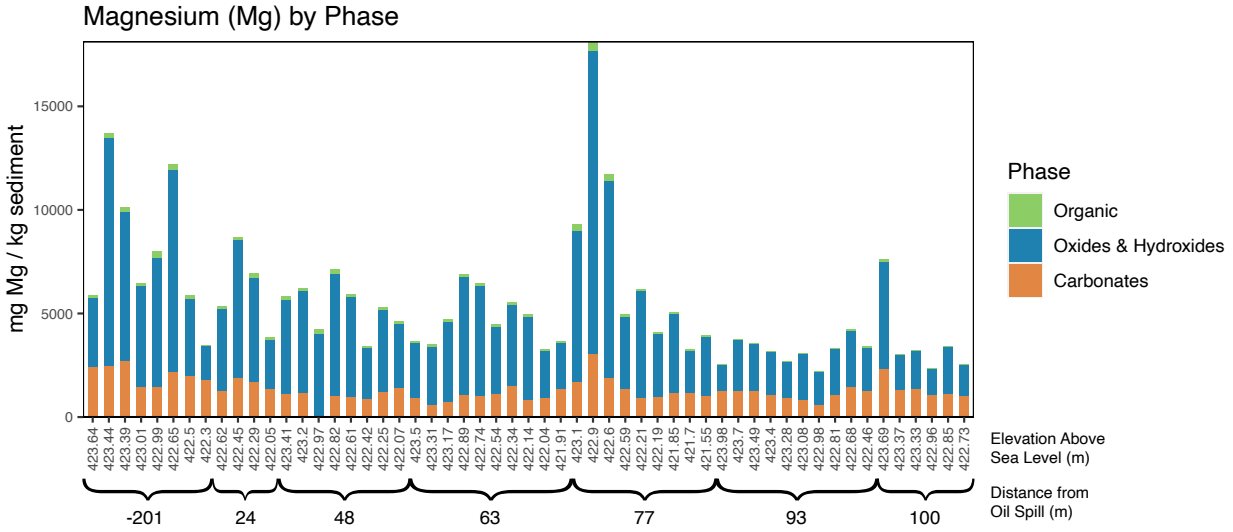

Figure 17. Stacked bar chart of magnesium (Mg) by phase based on sequential extraction data. The y-axis displays milligrams of Mg per kilogram sediment. The x-axis reports the sample's elevation is reported in m above sea level and the samples are grouped by the core's distance from the oil spill in meters.

Manganese shows a marked shift in geochemistry between background sediments and sediments in the plume (Figure 18). In the background, Mn was predominantly present in oxide and hydroxide phases, with measurable carbonates as well. In the plume body, there is a marked decrease in oxides and hydroxides and increase in carbonates.

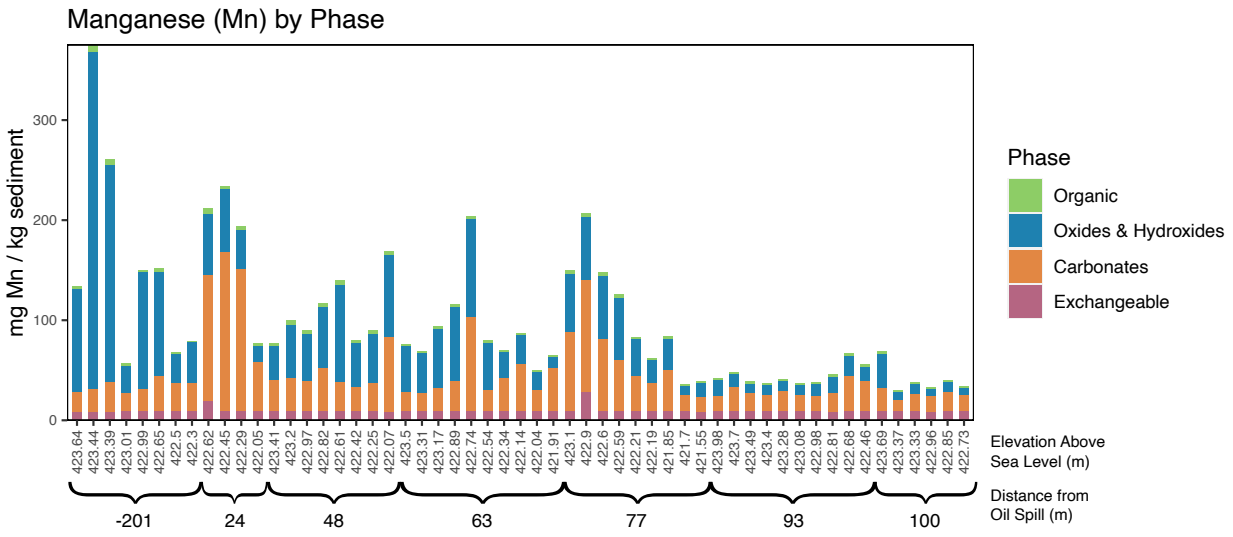

Figure 18. Stacked bar chart of manganese (Mn) by phase based on sequential extraction data. The y-axis displays milligrams of Mn per kilogram sediment. The x-axis reports the sample's elevation is reported in m above sea level and the samples are grouped by the core's distance from the oil spill in meters.

Nickel concentrations in the plume and background were sporadic and did not show an obvious geochemical shift in different zones (Figure 19). In fact, within a single zone, Ni concentrations in the various phases varied markedly from sample to sample. In the upper portion of the 77 m core, Ni is higher in carbonates and oxides and hydroxides relative to the rest of the interface and Fe-reducing sediment.

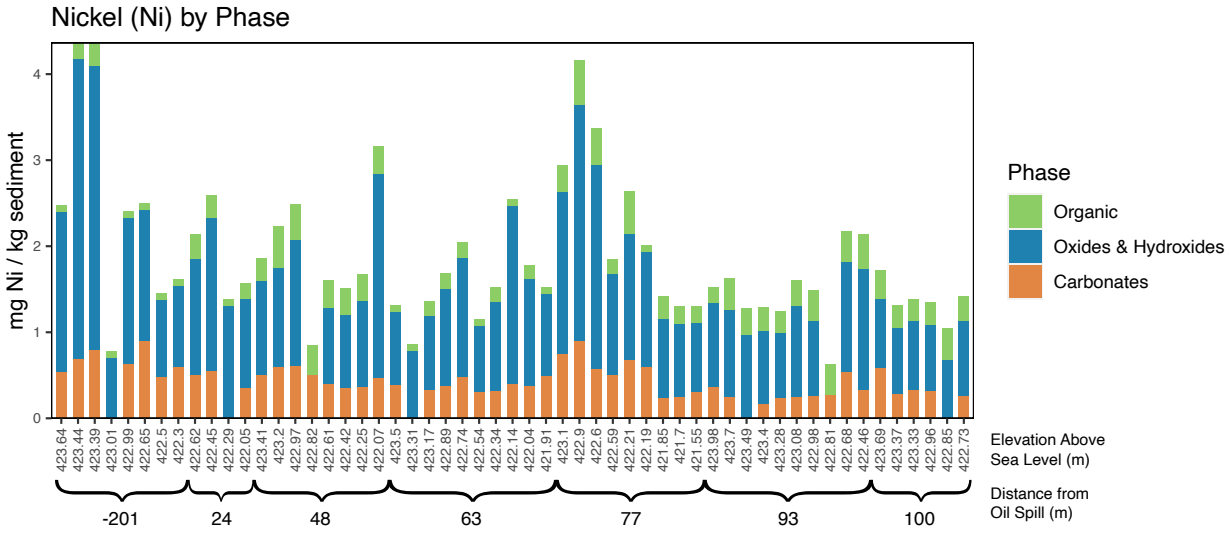

Figure 19. Stacked bar chart of nickel (Ni) by phase based on sequential extraction data. The y-axis displays milligrams of Ni per kilogram sediment. The x-axis reports the sample's elevation is reported in m above sea level and the samples are grouped by the core's distance from the oil spill in meters.

Lead was largely reported in oxides and hydroxides in the background and plume (Figure 20). However, in the plume zones, there is a mass loss of Pb in oxides, which corresponds to an increase in lead carbonates, which persist throughout the methanogenic and interface zones. Additionally, Pb in the oxides and hydroxides phase increases in the upper samples from the 77 m core.

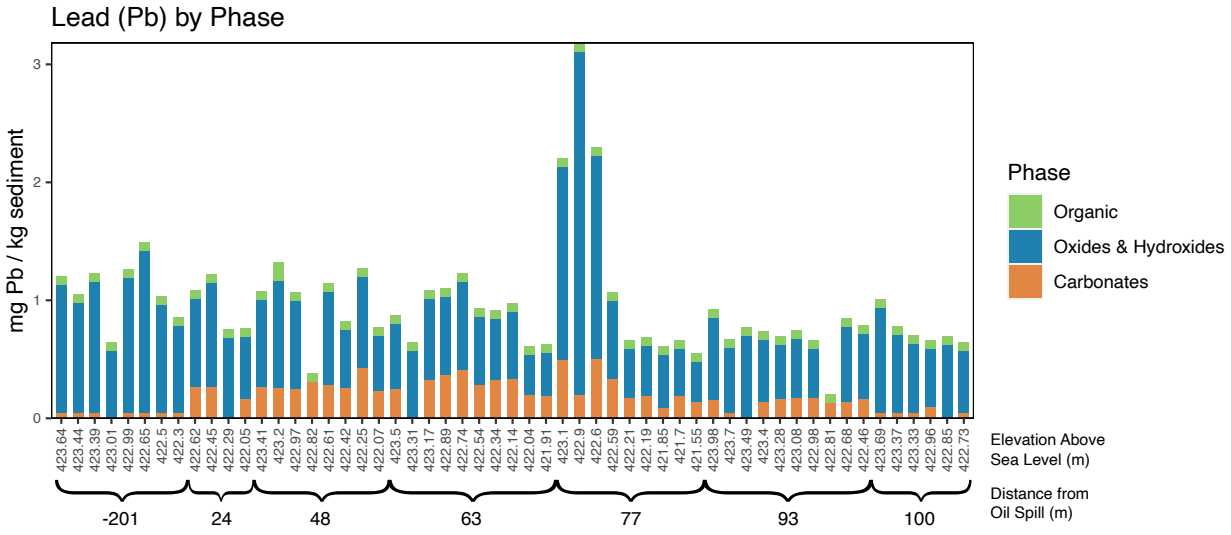

Figure 20. Stacked bar chart of lead (Pb) by phase based on sequential extraction data. The y-axis displays milligrams of Pb per kilogram sediment. The x-axis reports the sample's elevation is reported in m above sea level and the samples are grouped by the core's distance from the oil spill in meters.

Silicon was predominantly present in oxide and hydroxide and organic phases throughout both the plume and the background, although there is a measurable loss of oxide-bound Si in the plume compared to background, whereas the organic-bound Si is consistent in both regions (Figure 21). The exchangeable and carbonate phases for Si were consistent across all samples.

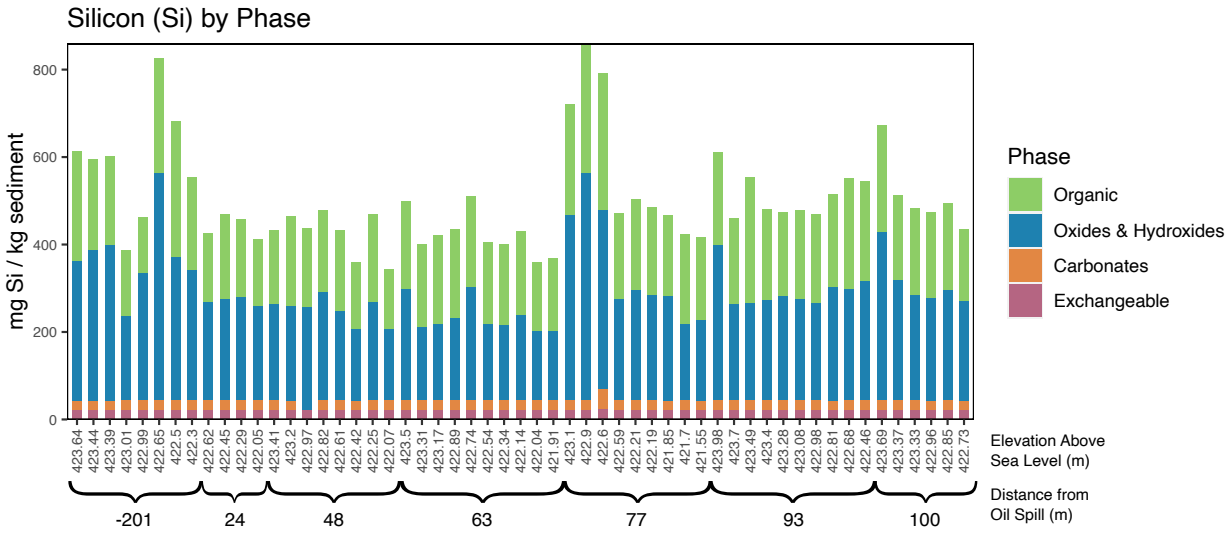

Figure 21. Stacked bar chart of silicon (Si) by phase based on sequential extraction data. The y-axis displays milligrams of Si per kilogram sediment. The x-axis reports the sample's elevation is reported in m above sea level and the samples are grouped by the core's distance from the oil spill in meters.

Strontium was predominantly present in the carbonate phase throughout both the plume and the background, however is lost from the background to the methanogenic sediment in both carbonate and oxide and hydroxide phases (Figure 22). An increase in oxides and hydroxides is observed in the Fe-reducing zone. Sr was below the detection limit for all exchangeable analysis, and is instead reported as half the lower detection limit.

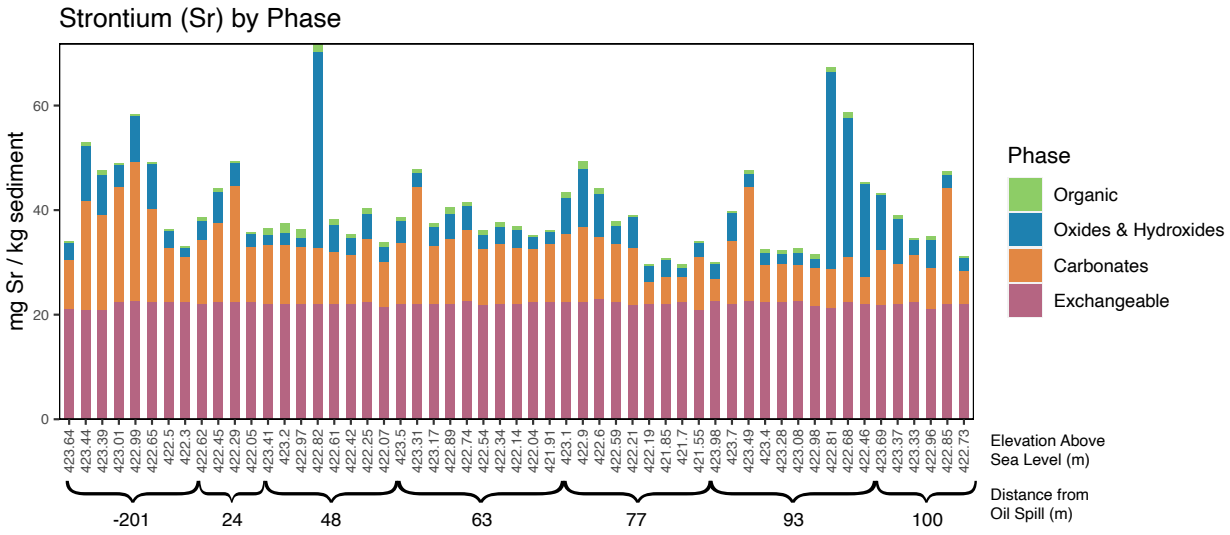

Figure 22. Stacked bar chart of strontium (Sr) by phase based on sequential extraction data. The y-axis displays milligrams of Sr per kilogram sediment. The x-axis reports the sample's elevation is reported in m above sea level and the samples are grouped by the core's distance from the oil spill in meters.

Zinc was predominantly present in the oxides and hydroxides phase throughout both the plume and the background (Figure 23). With the exception of a slight increase in oxides in the methanogenic sediment and sporadic increases in oxides or carbonates in a few samples, few obvious trends are discernable.

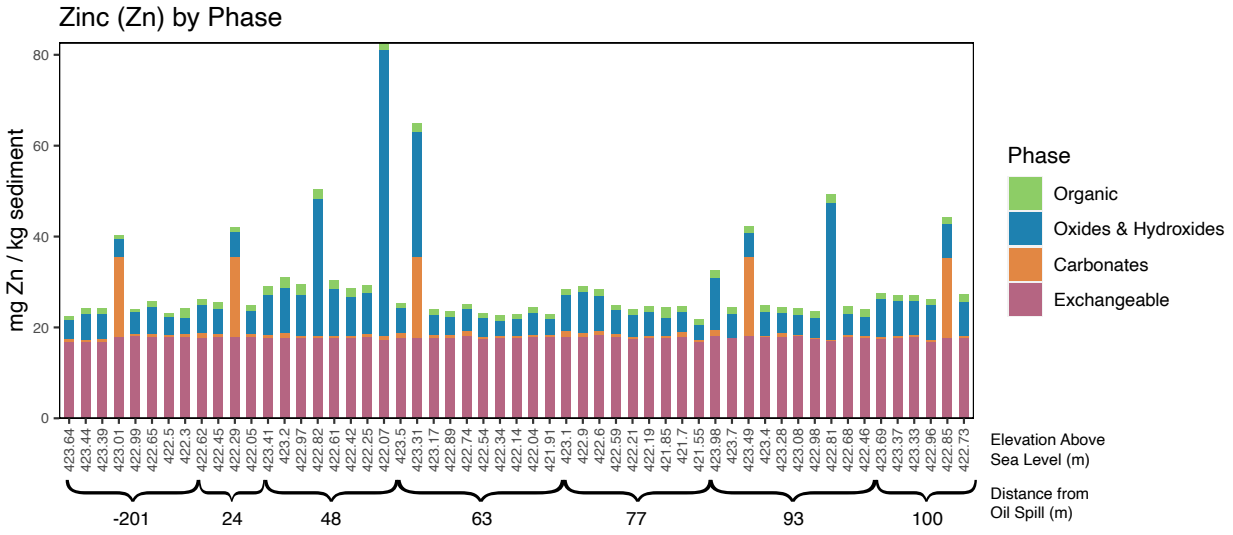

Figure 23. Stacked bar chart of zinc (Zn) by phase based on sequential extraction data. The y-axis displays milligrams of Zn per kilogram sediment. The x-axis reports the sample's elevation is reported in m above sea level and the samples are grouped by the core's distance from the oil spill in meters.

Statistical Analyses

Shapiro-Wilk tests indicated that only three of the element datasets (Cr in carbonates, Cr in organics, and Fe in organics) were normally distributed across zones (Table 3). Subsequent Shapiro-Wilk tests of log-transformed concentrations revealed that some carbonate phases and some oxide and hydroxide data were log-normally distributed, but the majority of the data were not. Therefore, further statistical analyses were conducted with non-parametric tests.

Table 3. Shapiro-Wilk Tests for Normality, wherein p-values greater than 0.05 (bold text) indicate normal or log-normal distribution, depending on the column.

Element	**Exchangeable**		**Carbonates**		**Oxides & Hydroxides**		**Organics**	
	p value normal	p value log	p value normal	p value log	p value normal	p value log	p value normal	p value log
Al	4.1×10^{-6}	2.7×10^{-6}	5.0×10^{-13}	1.9×10^{-9}	1.1×10^{-10}	8.6×10^{-11}	1.2×10^{-15}	3.7×10^{-14}
As	-	-	1.1×10^{-15}	1.1×10^{-15}	1.5×10^{-13}	1.4×10^{-13}	8.2×10^{-8}	9.3×10^{-6}

Ba	3.4×10^{-6}	2.2×10^{-6}	2.9×10^{-14}	2.2×10^{-11}	5.9×10^{-15}	1.8×10^{-9}	3.1×10^{-7}	2.6×10^{-7}
B	3.4×10^{-6}	2.2×10^{-6}	1.5×10^{-7}	**6.0×10^{-2}**	1.3×10^{-11}	3.4×10^{-5}	7.2×10^{-5}	9.8×10^{-6}
Ca	1.2×10^{-2}	2.2×10^{-2}	2.5×10^{-5}	1.4×10^{-3}	2.4×10^{-6}	**6.1×10^{-1}**	1.0×10^{-6}	2.6×10^{-2}
Ce	-	-	8.7×10^{-6}	2.1×10^{-2}	8.7×10^{-3}	**8.4×10^{-1}**	3.2×10^{-12}	3.6×10^{-7}
Co	-	-	7.2×10^{-4}	6.2×10^{-3}	6.0×10^{-8}	5.6×10^{-3}	4.2×10^{-15}	1.6×10^{-14}
Cr	-	-	**3.0×10^{-1}**	-	1.9×10^{-6}	1.1×10^{-3}	**6.6×10^{-1}**	-
Cu	3.4×10^{-6}	2.2×10^{-6}	7.7×10^{-12}	1.1×10^{-2}	6.3×10^{-14}	1.9×10^{-4}	7.7×10^{-3}	4.9×10^{-4}
Fe	7.6×10^{-6}	4.9×10^{-6}	8.5×10^{-4}	1.9×10^{-3}	2.0×10^{-4}	**5.1×10^{-1}**	**9.8×10^{-2}**	-
La	-	-	1.3×10^{-3}	**1.2×10^{-1}**	6.0×10^{-3}	**8.7×10^{-1}**	2.2×10^{-9}	1.3×10^{-2}
Mg	-	-	6.6×10^{-5}	**2.3×10^{-1}**	1.0×10^{-6}	**4.6×10^{-1}**	9.0×10^{-7}	2.3×10^{-3}
Mn	2.0×10^{-15}	5.8×10^{-15}	1.2×10^{-9}	3.3×10^{-4}	3.6×10^{-10}	**8.7×10^{-2}**	1.1×10^{-5}	**3.1×10^{-1}**
Ni	-	-	1.9×10^{-2}	**5.1×10^{-1}**	1.0×10^{-7}	3.4×10^{-4}	5.6×10^{-3}	1.3×10^{-5}
Pb	-	-	5.1×10^{-3}	5.7×10^{-5}	2.5×10^{-9}	5.4×10^{-3}	2.2×10^{-16}	2.2×10^{-16}
Si	5.2×10^{-6}	3.4×10^{-6}	3.4×10^{-16}	4.0×10^{-16}	3.2×10^{-6}	4.6×10^{-3}	3.1×10^{-4}	1.4×10^{-2}
Sr	5.2×10^{-6}	3.4×10^{-6}	8.5×10^{-5}	**7.1×10^{-2}**	9.4×10^{-12}	8.3×10^{-5}	3.4×10^{-5}	1.7×10^{-5}
Zn	3.4×10^{-6}	2.2×10^{-6}	6.2×10^{-14}	1.9×10^{-9}	5.0×10^{-13}	2.3×10^{-7}	1.5×10^{-2}	**1.3×10^{-1}**

A Kruskall-Wallis non-parametric one-way analysis of variance test identifies if statistically significant differences exist between at least two of the four geochemical zones for a given element in a given mineral phase (Table 4). The p-values for the majority of carbonates, oxides and hydroxides, and organics phase tests were less than 0.05, indicating at least one significant difference in elemental concentration between the zones. All elements with exchangeable phase data reported had p-values greater than 0.05, indicating no significant

difference between zones, except for Ca. Given that the null hypothesis was maintained for almost all of the exchangeable datasets, the exchangeable data were removed from further analysis.

Table 4. Kruskall-Wallis Tests for Variance, wherein p-values greater than 0.05 are bolded, indicating no significant difference between zones.

Element	Exchangeable	Carbonates	Oxides & Hydroxides	Organics
Al	**8.7×10^{-1}**	**2.4×10^{-1}**	1.3×10^{-2}	1.4×10^{-7}
As	-	**6.2×10^{-1}**	**1.3×10^{-1}**	5.3×10^{-9}
B	**8.2×10^{-1}**	3.1×10^{-2}	1.3×10^{-2}	9.5×10^{-8}
Ba	**8.2×10^{-1}**	5.9×10^{-4}	2.9×10^{-3}	4.9×10^{-3}
Ca	1.2×10^{-3}	2.1×10^{-2}	3.9×10^{-5}	2.2×10^{-4}
Ce	-	4.2×10^{-2}	3.3×10^{-2}	3.8×10^{-3}
Co	-	**8.9×10^{-2}**	3.7×10^{-4}	**5.7×10^{-1}**
Cr	-	**1.4×10^{-1}**	3.8×10^{-3}	6.9×10^{-8}
Cu	**8.2×10^{-1}**	9.1×10^{-4}	**1.5×10^{-1}**	1.4×10^{-2}
Fe	**8.5×10^{-1}**	2.0×10^{-5}	3.8×10^{-3}	1.7×10^{-4}
La	-	**5.9×10^{-1}**	2.0×10^{-2}	1.7×10^{-3}
Mg	-	1.3×10^{-3}	4.3×10^{-5}	7.3×10^{-7}
Mn	**9.7×10^{-1}**	7.1×10^{-5}	1.1×10^{-6}	1.4×10^{-3}
Ni	-	1.9×10^{-4}	2.1×10^{-2}	2.7×10^{-4}
Pb	-	2.7×10^{-7}	4.4×10^{-3}	**3.1×10^{-1}**
Si	**8.5×10^{-1}**	**7.2×10^{-1}**	3.1×10^{-3}	4.8×10^{-3}
Sr	**8.5×10^{-1}**	1.1×10^{-2}	**7.3×10^{-1}**	4.1×10^{-2}
Zn	**8.2×10^{-1}**	4.7×10^{-2}	1.0×10^{-3}	2.1×10^{-4}

The results of the non-parametric Pairwise-Wilcoxon tests with Bonferroni adjustments compared an element between zones within a given mineral phase (Table 5). Of comparisons that were significantly different, several elements were depleted in the Fe-reducing zone across all phases examined, including Ba, Ca, Ce, Co, Mg, Mn, and Sr. Pb and Fe behaved similarly in that both were present in oxides and hydroxides in the background sediment, but increased in the carbonates phase in the plume. Arsenic, B, and Cr were all found in the organic phase in the plume, but did not occur with organics in the background sediment.

Table 5. Pairwise Wilcoxon test p-values with Bonferroni adjustments. Statistically significant difference are highlighted in green. In cells that denote a statistically significant difference between zones, the arrow points to the zone of greater concentration.

		Carbonates			Oxides & Hydroxides			Organics		
		Background	Fe-Reducing	Interface	Background	Fe-Reducing	Interface	Background	Fe-Reducing	Interface
Al	Fe-Reducing	1.000	-	-	0.167	-	-	-	-	-
	Interface	1.000	1.000	-	1.000	0.027 ↑	-	-	-	-
	Methanogenic	0.590	1.000	0.800	0.842	1.000	0.295	-	-	-
As	Fe-Reducing	-	-	-	-	-	-	0.000 ←	-	-
	Interface	-	-	-	-	-	-	0.093	0.000 ↑	-
	Methanogenic	-	-	-	-	-	-	0.001 ←	0.006 ↑	0.003 ←
B	Fe-Reducing	0.786	-	-	1.000	-	-	0.000 ←	-	-
	Interface	0.013 ↑	0.627	-	1.000	0.927	-	1.000	0.000 ↑	-
	Methanogenic	0.977	1.000	1.000	1.000	0.008 ←	0.136	0.016 ←	1.000	0.001 ←
Ba	Fe-Reducing	0.020 ↑	-	-	0.034 ↑	-	-	1.000	-	-
	Interface	0.449	0.011 ←	-	0.065	1.000	-	1.000	1.000	-
	Methanogenic	0.223	0.026 ←	1.000	1.000	0.064	0.171	0.073	0.001 ←	0.100
Ca	Fe-Reducing	0.042 ↑	-	-	0.008 ↑	-	-	0.004 ↑	-	-
	Interface	0.111	1.000	-	1.000	0.000 ←	-	0.566	0.011 ←	-
	Methanogenic	0.454	0.479	1.000	1.000	0.001 ←	1.000	0.495	0.009 ←	1.000
Ce	Fe-Reducing	1.000	-	-	0.141	-	-	1.000	-	-
	Interface	0.100	0.430	-	1.000	0.217	-	0.136	0.043 ←	-
	Methanogenic	0.420	0.710	1.000	1.000	0.046 ←	1.000	0.151	0.056	1.000
Co	Fe-Reducing	1.000	-	-	0.036 ↑	-	-	1.000	-	-
	Interface	1.000	1.000	-	0.101	0.059	-	1.000	1.000	-
	Methanogenic	1.000	0.051	0.452	0.773	0.004 ←	0.510	1.000	1.000	1.000
Cr	Fe-Reducing	1.000	-	-	0.033 ←	-	-	0.001 ←	-	-
	Interface	1.000	0.690	-	1.000	0.006 ↑	-	0.023 ←	0.000 ↑	-
	Methanogenic	1.000	0.120	1.000	1.000	0.154	1.000	0.005 ←	0.121	0.042 ←
Cu	Fe-Reducing	1.000	-	-	1.000	-	-	1.000	-	-
	Interface	0.068	0.005 ←	-	0.150	1.000	-	0.190	0.440	-
	Methanogenic	1.000	1.000	0.016 ↑	1.000	1.000	0.780	0.110	0.220	0.800
Fe	Fe-Reducing	0.000 ←	-	-	0.026 ↑	-	-	0.013 ←	-	-
	Interface	0.000 ←	0.110	-	0.011 ↑	1.000	-	0.003 ←	1.000	-
	Methanogenic	0.000 ←	0.730	1.000	0.006 ↑	0.360	1.000	0.001 ←	0.078	0.045 ←
La	Fe-Reducing	1.000	-	-	0.169	-	-	0.141	-	-
	Interface	1.000	1.000	-	1.000	0.237	-	0.093	0.424	-
	Methanogenic	1.000	1.000	1.000	1.000	0.008 ←	1.000	0.013 ←	0.073	0.769
Mg	Fe-Reducing	0.000 ↑	-	-	0.008 ↑	-	-	0.007 ↑	-	-
	Interface	0.003 ↑	1.000	-	1.000	0.000 ←	-	0.397	0.000 ←	-
	Methanogenic	0.010 ↑	1.000	1.000	1.000	0.000 ←	1.000	0.692	0.000 ←	1.000
Mn	Fe-Reducing	0.138	-	-	0.000 ↑	-	-	1.000	-	-
	Interface	1.000	0.006 ←	-	0.180	0.000 ←	-	1.000	1.000	-
	Methanogenic	0.025 ←	0.000 ←	0.843	1.000	0.000 ←	1.000	1.000	0.001 ←	0.005 ←
Ni	Fe-Reducing	0.001 ←	-	-	0.180	-	-	0.003 ←	-	-
	Interface	0.057	0.066	-	1.000	0.250	-	0.540	0.022 ↑	-
	Methanogenic	0.087	0.012 ↑	1.000	1.000	0.030 ←	1.000	0.014 ←	1.000	0.127
Pb	Fe-Reducing	0.062	-	-	0.002 ↑	-	-	-	-	-
	Interface	0.001 ←	0.000 ←	-	0.117	1.000	-	-	-	-
	Methanogenic	0.002 ←	0.000 ←	1.000	0.072	0.322	0.466	-	-	-
Si	Fe-Reducing	1.000	-	-	0.138	-	-	1.000	-	-
	Interface	1.000	1.000	-	0.075	0.529	-	1.000	1.000	-
	Methanogenic	1.000	1.000	1.000	0.013 ↑	0.037 ↑	1.000	0.415	0.005 ↑	0.026 ↑
Sr	Fe-Reducing	0.034 ↑	-	-	1.000	-	-	1.000	-	-
	Interface	1.000	0.206	-	1.000	1.000	-	0.480	1.000	-
	Methanogenic	1.000	0.037 ←	1.000	1.000	1.000	1.000	0.090	0.220	1.000
Zn	Fe-Reducing	0.520	-	-	0.322	-	-	0.095	-	-
	Interface	1.000	0.200	-	1.000	0.354	-	1.000	0.001 ↑	-
	Methanogenic	1.000	0.150	1.000	0.013 ←	0.185	0.002 ←	0.095	0.727	0.012 ↑

A comparison matrix was constructed from the values in the Pairwise Wilcoxon tests to compare commonalities between trace element mobilization and sequestration patterns as identified from the statistically significant differences between zones (Figure 24). The following

element pairs correlated completely, indicating shared statistical differences between zones and phases: Al and Cr, Ca and Mg, Ce and Mg, Co and Mg, Ce and Ca, Co and Ca, Co and Mn, La and B, La and Ni, Sr and Ba, and Sr and Ni. Several elements (Al, Cu, Si, and Zn) did not correlate with many other elements examined, while Mn and Ni correlated with numerous elements.

	Al (2)	As (10)	B (12)	Ba (10)	Ca (14)	Ce (4)	Co (4)	Cr (14)	Cu (4)	Fe (20)	La (4)	Mg (18)	Mn (16)	Ni (12)	Pb (10)	Si (8)	Sr (4)	Zn (8)
Al (2)	x	0	0	0	0	0	0	1	0	0	0	0	0	0	0	0	0	0
As (10)	0	x	0.8	0	0	0	0	0.8	0	0.6	0.2	0	0.2	0.6	0	0.2	0	0.2
B (12)	0	0.67	x	0	0.17	0.17	0.17	0.67	0	0.5	0.33	0.33	0.33	0.67	0	0	0	0.17
Ba (10)	0	0	0	x	0.6	0	0.2	0	0.2	0.2	0	0.6	0.8	0.4	0.6	0	0.4	0
Ca (14)	0	0	0.14	0.43	x	0.29	0.29	0	0	0.14	0.14	1	0.57	0.29	0.14	0	0.14	0
Ce (4)	0	0	0.5	0	1	x	0.5	0	0	0	0.5	1	0.5	0.5	0	0	0	0
Co (4)	0	0	0.5	0.5	1	0.5	x	0	0	0.5	0.5	1	1	0.5	0.5	0	0	0
Cr (14)	0.14	0.57	0.57	0	0	0	0	x	0	0.57	0.14	0	0.14	0.43	0	0	0	0.14
Cu (4)	0	0	0	0.5	0	0	0	0	x	0	0	0	0.5	0	0.5	0	0	0
Fe (20)	0	0.3	0.3	0.1	0.1	0	0.1	0.4	0	x	0.1	0.1	0.3	0.2	0.3	0.1	0	0
La (4)	0	0.5	1	0	0.5	0.5	0.5	0.5	0	0.5	x	0.5	0.5	1	0	0	0	0
Mg (18)	0	0	0.22	0.33	0.78	0.22	0.22	0	0	0.11	0.11	x	0.44	0.22	0.11	0	0.11	0
Mn (16)	0	0.12	0.25	0.5	0.5	0.13	0.25	0.13	0.13	0.38	0.13	0.5	x	0.25	0.5	0	0.13	0
Ni (12)	0	0.5	0.67	0.33	0.33	0.17	0.17	0.5	0	0.33	0.33	0.33	0.33	x	0.17	0	0.33	0.17
Pb (10)	0	0	0	0.6	0.2	0	0.2	0	0.2	0.6	0	0.2	0.8	0.2	x	0	0.2	0
Si (8)	0	0.25	0	0	0	0	0	0	0	0.25	0	0	0	0	0	x	0	0.25
Sr (4)	0	0	0	1	0.5	0	0	0	0	0	0	0.5	0.5	1	0.5	0	x	0
Zn (8)	0	0.25	0.25	0	0	0	0	0.25	0	0	0	0	0	0.25	0	0.25	0	x

Figure 24. Correlation matrix for elemental comparison. A value of 0 indicates no correlation in significantly different zones and phases, whereas a value of 1 indicates perfect correlation.

Principal Component Analyses

PCA was employed to further examine elemental relationships for each phase. In the carbonates PCA biplot (Figure 25), PC1 accounts for 30.1% of variance and PC2 accounts for

26.52% of variance, such that both are similarly influential components. B exerts the most influence on PC1, with Pb and Fe extending into the positive PC1 space and B extending into the negative PC1 space. All other elements examined also extend into the negative PC1 space. Pb exerts the most influence on PC2, followed by Fe, B, and Mn. Arsenic remains at the origin, with no variance along either of the main principal component axes, indicating As has little variance within carbonates. The near 180° difference between Pb and Fe with B indicates that they are negatively correlated with respect to PC1. Elements appear to be more associated with carbonates in the methanogenic and interface zones overall, but Ca, Mg, and B seem to associate more closely with carbonates in the background. No vectors point directly into the cluster of Fe-reducing sediment samples, but Fe points near the mixed cluster of interface and Fe-reducing sediment. Very deep samples (> 100 cm below the top of the core) appear to be in positive PC1 space, while shallow samples appear to group in negative PC1 space.

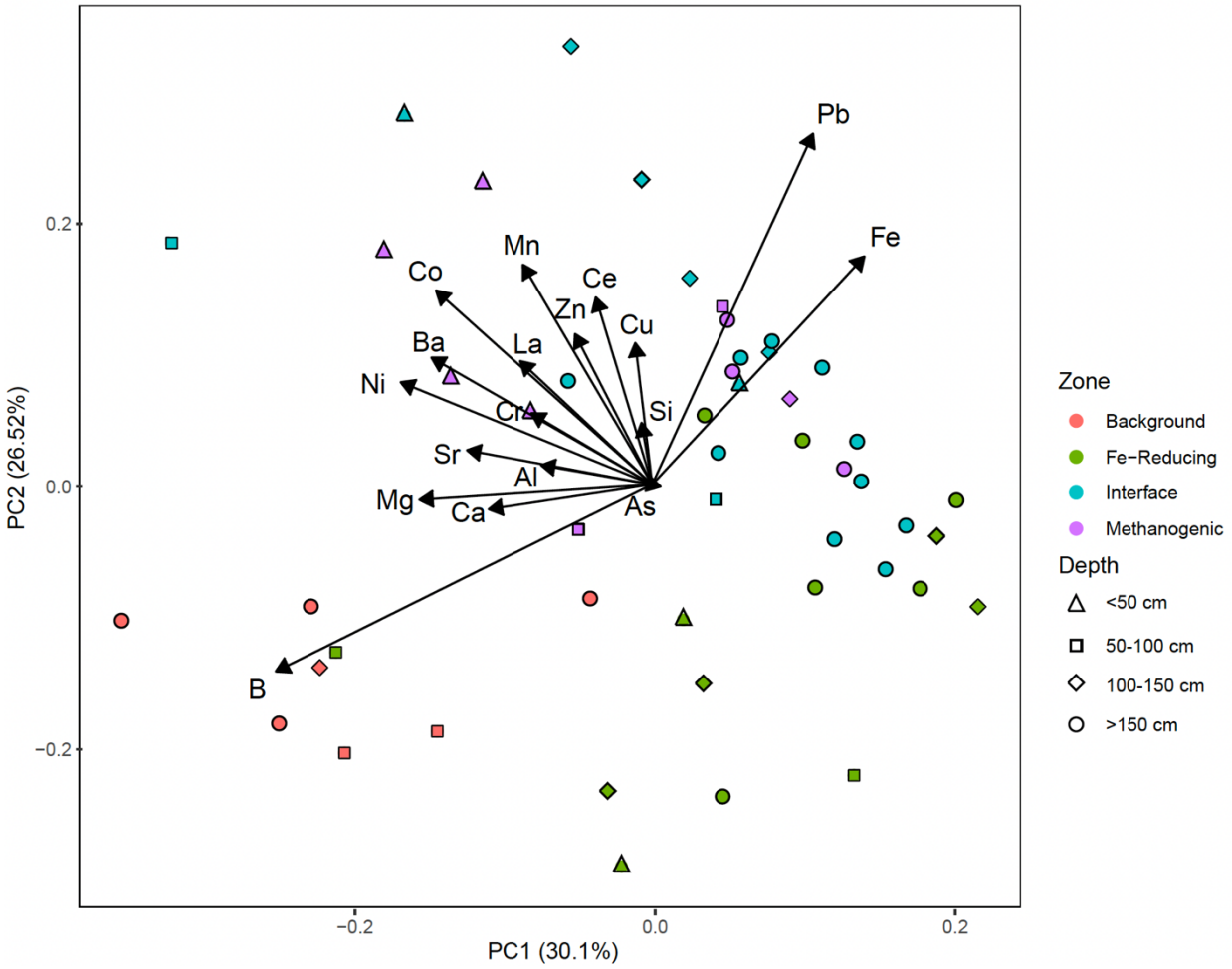

Figure 25. PCA biplot of carbonates, with samples colorized by zone and symbolized by depth.

In the oxides and hydroxides PCA biplot (Figure 26), PC1 accounts for 45.04% of the data variance. Metals point into the negative PC1 space, towards the majority of the background samples. Methanogenic samples are clustered around the origin, extending towards negative PC1, in greater association with elements Mn, Ca, Mg, B, Ni, and Cu. PC2 accounts for 14.65% of the data variance, with Al exerting the strongest control. No element vectors extend into the predominantly interface zone samples. In the Fe-reducing cluster of samples, Al, As, and Cr are present. Al exerts the strongest influence on PC2, having the longest vector in this dimension. Interestingly, oxide chemistry seems more similar between background and methanogenic (i.e.,

most reducing) sediment compared to interface or Fe-reducing sediment. Depth does not appear to influence element distribution in oxides (Figure 26).

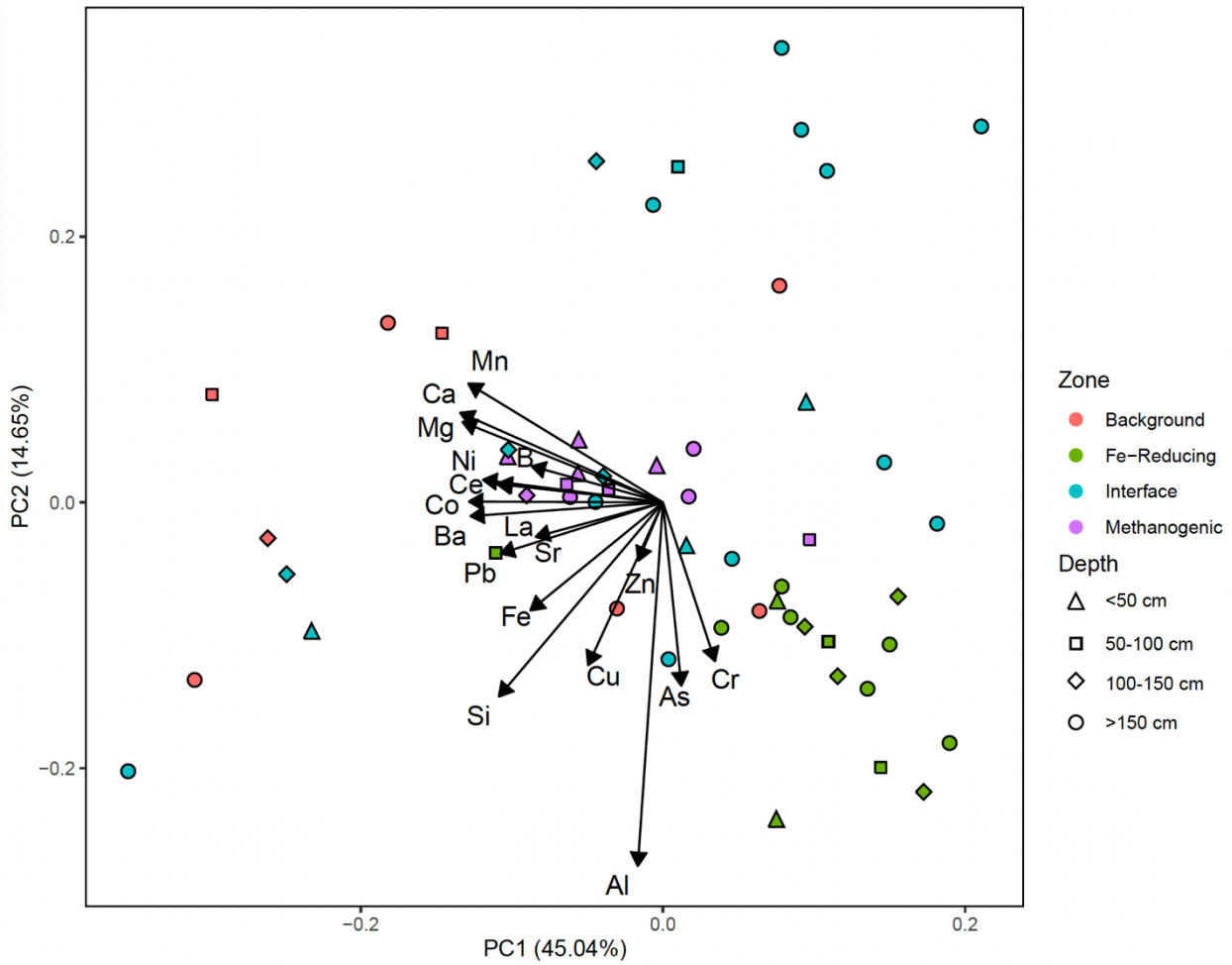

Figure 26. PCA biplot of oxides and hydroxides, with samples colorized by zone and symbolized by depth.

In the PCA biplot for organic matter (Figure 27), PC1 represents 41.05% of the variance in the data set. Arsenic, B, and Ni (followed by Cr, Zn, Sr) exert the strongest influence on PC1, all extending into negative PC1 space. However, the As, B, and Ni cluster is tightly associated with organics in the Fe-reducing zone and is orthogonal to the Cr, Zn, and Sr cluster, which are associated with methanogenic sediments. Largely these two clusters diverge along the PC2 axis, which explains 19.77% of the data variance, with Sr, Mg, and As exerting the most influence on the component. Most methanogenic zone samples are located in negative PC1, negative PC2,

alongside the elements Ni, Zn, Fe, Cu, Sr, La, Ca, Pb, Si, Ce, and Mn. Spread across positive PC1 are the interface and background sediment samples. Ca and Mg extend into positive PC1, negative PC2, suggesting a negative correlation with As, B, and Cr. There is no observed correlation with the depth of the samples. However, samples from the four geochemical zones show distinct clusters. There is little organic signature in the background or in the interface zone. Most of the organic signature occurs in the Fe-reducing zone, where As, B, and Cr are located, and in the methanogenic zone.

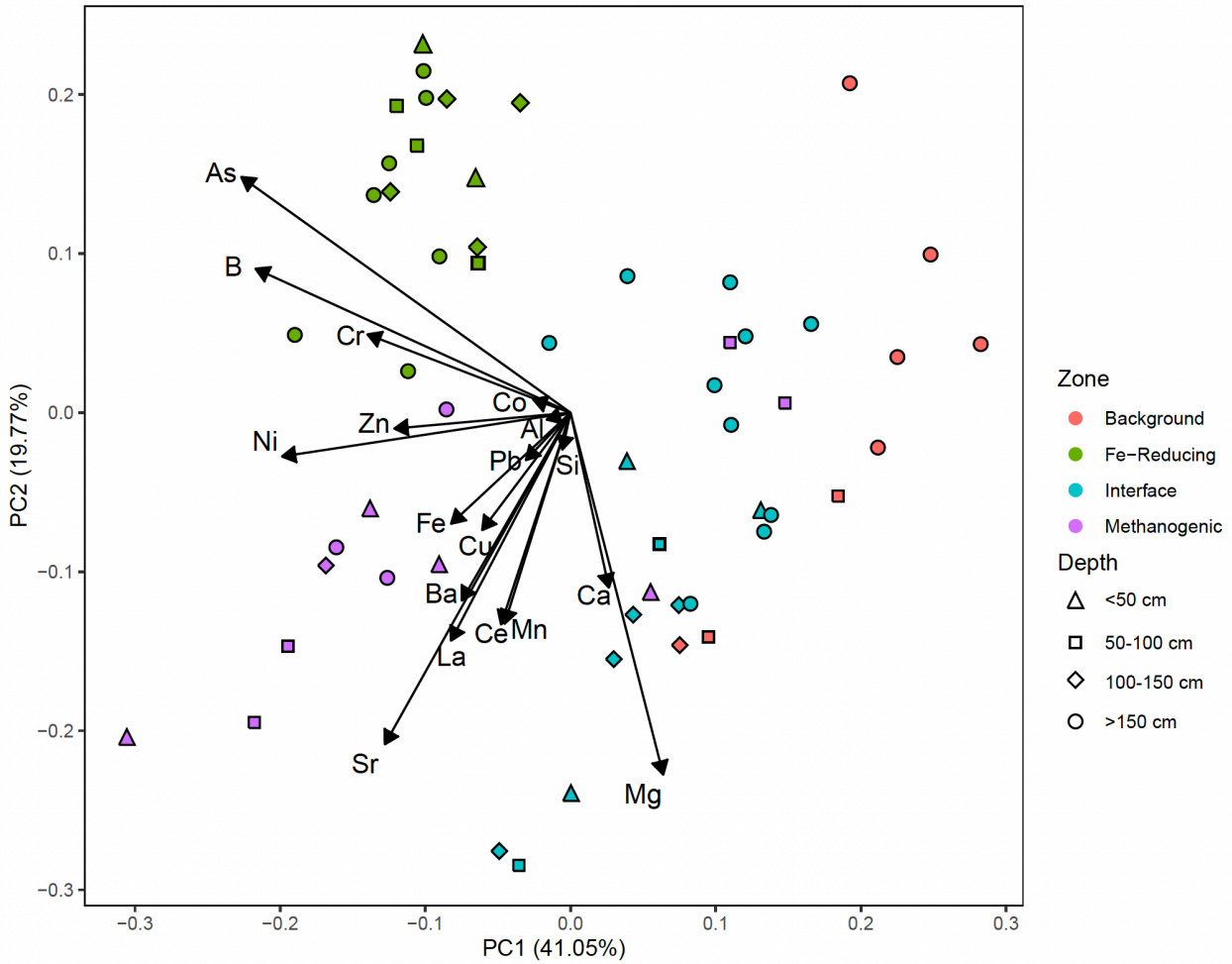

Figure 27. PCA biplot of organics, with samples colorized by zone and symbolized by depth.

Alkaline Organic Extraction Analyses: Chromatograms

Arsenic standards ranging from 0 to 100 ppb run as calibration for ICP-MS performed linearly with an R^2 value of 0.9996. HPLC-UV-FLD was calibrated with standards of acetone, guanosine, and sodium polystyrene sulfonate before being run.

Select sediment samples (Figures 6-23) that yielded a notable organic signature for multiple elements in the sequential chemical extraction procedure were chosen to further characterize trace metals bound by organic carbon. Retention times for trace metal chromatograms from HPLC-SEC-ICP-MS separation were overlaid with organic carbon spectra from fluorescence and ultraviolet detectors (FLD/UV) to yield signals of co-occurring OM and trace elements, which indicates trace elements complexing with organic matter in sediment. Inorganic and free trace elements, if present, elute later in the 40-min run, owing to their lighter masses. OM elution data and trace element peaks are summarized in Table 6.

In the background, the OM elution range occurred between 11- and 30-min (Figure 28). ^{52}Cr, ^{55}Mn, ^{56}Fe, ^{57}Fe, and ^{66}Zn all eluted at about 12.5-min, concurring with a small OM peak from 11-13 minutes. ^{52}Cr and ^{66}Zn each had secondary peaks at 14.5-min, overlapping with the strongest OM signal. The remaining peaks occurred within the strongest OM signal. ^{59}Co had two peaks, at 14.5- and 16.5-min. ^{60}Ni had two peaks, at 14- and 20-min. An ^{75}As peak was observed in the ICP-MS chromatogram at 14.5-min. ^{88}Sr was observed at 19.5-min. ^{121}Sb peaked at 13- and 17.5-min. ^{137}Ba peaked at 20-min.

In the 70 m interface zone sample, the OM elution range occurred between 12- and 24-min, however the strongest peak shifted forward to the 12-14 min range (Figure 29). The leading edge of the strongest OM peak overlapped with the observed peaks for ^{52}Cr, ^{55}Mn, ^{56}Fe, ^{57}Fe, and ^{66}Zn at 12.5-min, with ^{66}Zn also having a peak at 13.5-min alongside ^{59}Co and ^{60}Ni. All additional

observed peaks occurred within the weaker OM signal. A peak was observed for ^{51}V at 16-min. ^{59}Co had a second peak at 16.5-min along with ^{121}Sb. An ^{75}As peak was observed in the ICP-MS chromatogram at 14.5-min. ^{137}Ba peaked at 19.5-min. No peaks were observed for ^{43}Ca, ^{44}Ca, and ^{88}Sr.

Further downgradient in the interface zone, at 77 m, the DOM elution range occurred between 13-min and 32-min, with a gradual baseline shift through the end of the 40-min run. The strongest OM peak occurred between 14- and 18-min, while the weaker occurred after 18-min (Figure 30). Interestingly, the peaks for ^{52}Cr, ^{55}Mn, ^{56}Fe, ^{57}Fe, and ^{66}Zn at 12.5-min and ^{59}Co and ^{60}Ni at 13.5-min occurred prior to the OM elution range. The remaining peaks occurred within the elution range. A peak was observed for ^{35}Cl at 16.5-min. ^{43}Ca and ^{44}Ca had peaks at 20-min, with a baseline shift throughout the run. ^{52}Cr and ^{66}Zn also had peaks at 14.5-min. ^{59}Co had additional peaks at 14- and 16-min. An ^{75}As peak was observed in the ICP-MS chromatogram at 14.5-min. ^{137}Ba peaked at 20-min with a baseline shift throughout the run. No peaks were observed for ^{51}V or ^{88}Sr.

In the Fe-reducing zone, two samples from the same core were analyzed using HPLC-SEC-ICP-MS. In the shallower sample, the OM elution range was observed between 12- and 30-min, with the strongest OM peak occurring between 12- and 18-min (Figure 31). All observed peaks overlapped with the OM signal. A peak was observed for ^{35}Cl at 16.5-min. ^{52}Cr peaks were observed at 15- and 17-min. Poorly defined peaks for ^{56}Fe and ^{57}Fe were observed at 17-min. ^{59}Co and ^{66}Zn observed peaks at 14.5- and 16.5-min, with ^{59}Co having an additional peak at 13.5-min. ^{60}Ni peaked 14-min. ^{75}As peaks were observed in the ICP-MS chromatogram at 15- and 19.5-min. ^{88}Sr peaked at 19-min, with a baseline shift throughout the run. Peaks were observed for ^{121}Sb at 13- and 16.5-min. ^{137}Ba peaked at 20-min. No peaks were observed for ^{43}Ca, ^{44}Ca, ^{51}V, or ^{55}Mn.

In the deeper Fe-reducing sample, the OM elution range was observed between 12- and 29-min, with the strongest peak occurring between 12- and 19-min (Figure 32). ^{52}Cr, ^{55}Mn, ^{56}Fe, ^{57}Fe, and ^{66}Zn observed peaks at 12.5-min, along the leading edge of the OM signal. The remaining peaks occurred within the range of the strongest OM peak. Peaks were observed for ^{35}Cl and ^{51}V at 16-min. ^{52}Cr and ^{66}Zn also had peaks at 14-min. A poorly defined peak is observed for ^{52}Cr at 16-min. ^{59}Co and ^{60}Ni peaked 13-, 14-, and 16-min. An ^{75}As peak observed in the ICP-MS chromatogram at 14.5-min. Peaks were observed for ^{121}Sb at 12.5- and 16-min. ^{137}Ba had peaks at 12.5- and 19.5-min, with a baseline shift throughout the run. No peaks were observed for ^{43}Ca, ^{44}Ca, or ^{88}Sr.

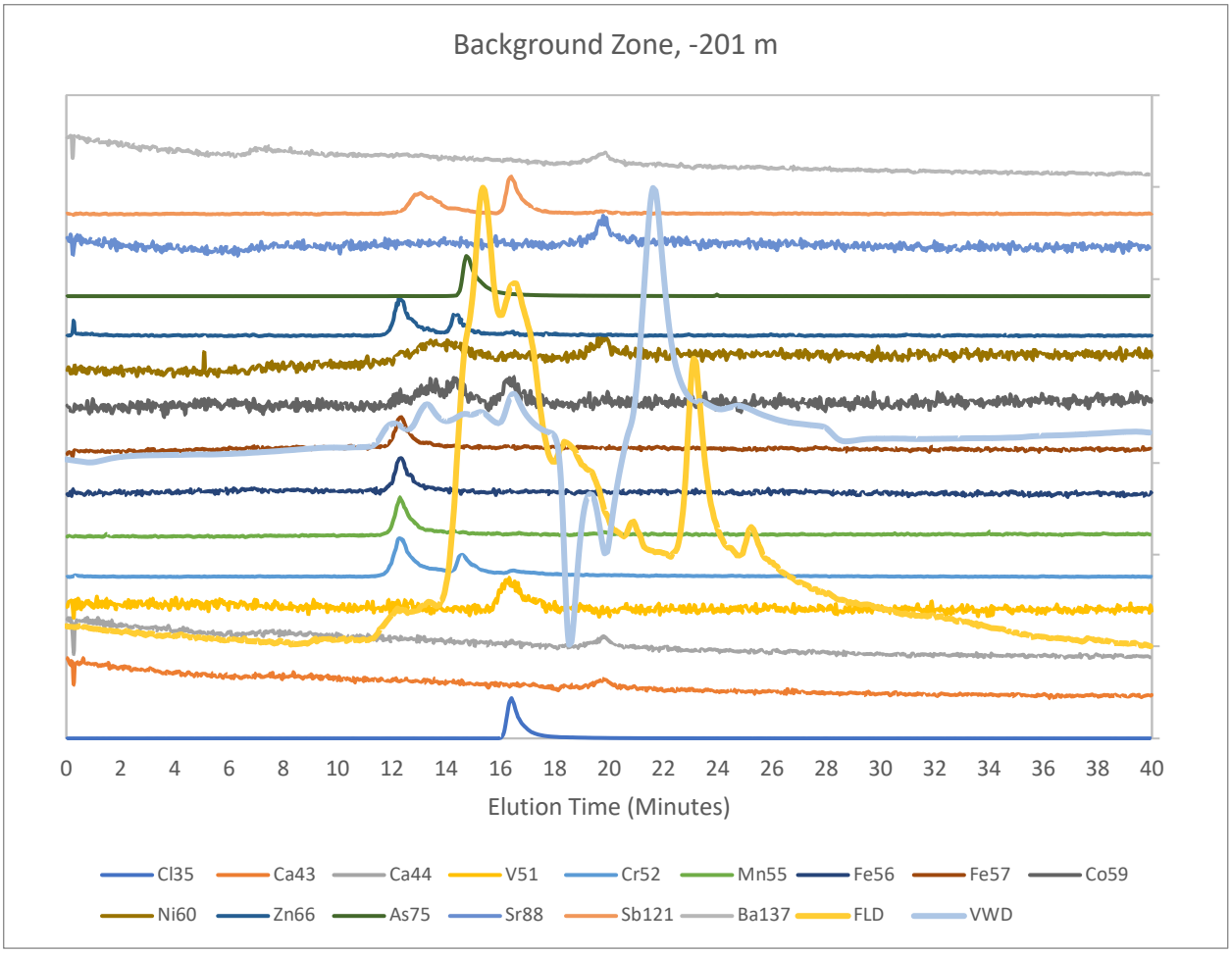

Figure 28. Time-matched chromatograms of ICP-MS data (primary axis) and FLD data (secondary axis) for a background sample. The positions on the y-axes are arbitrary.

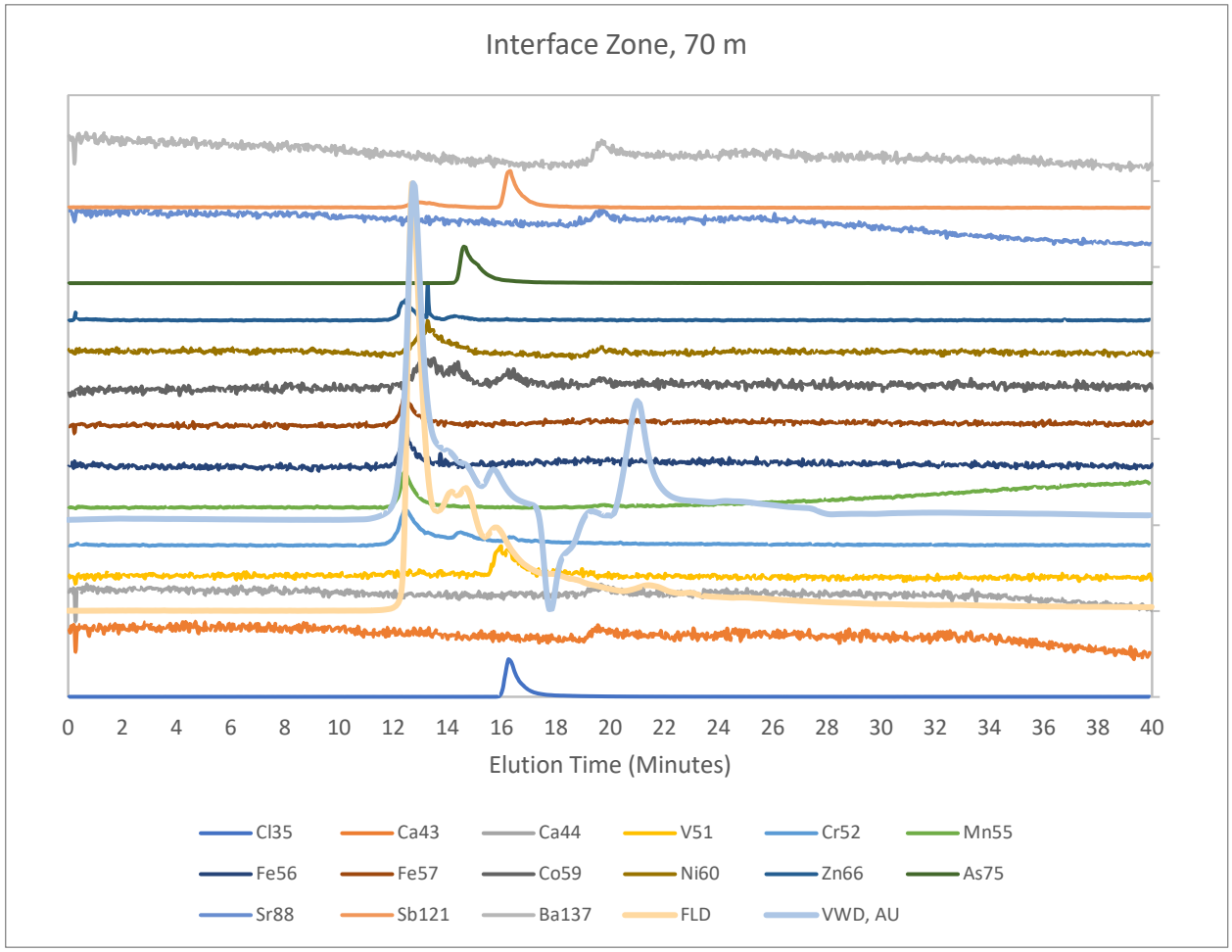

Figure 29. Time-matched chromatograms of ICP-MS data (primary axis) and FLD data (secondary axis) for an interface sample. The positions on the y-axes are arbitrary.

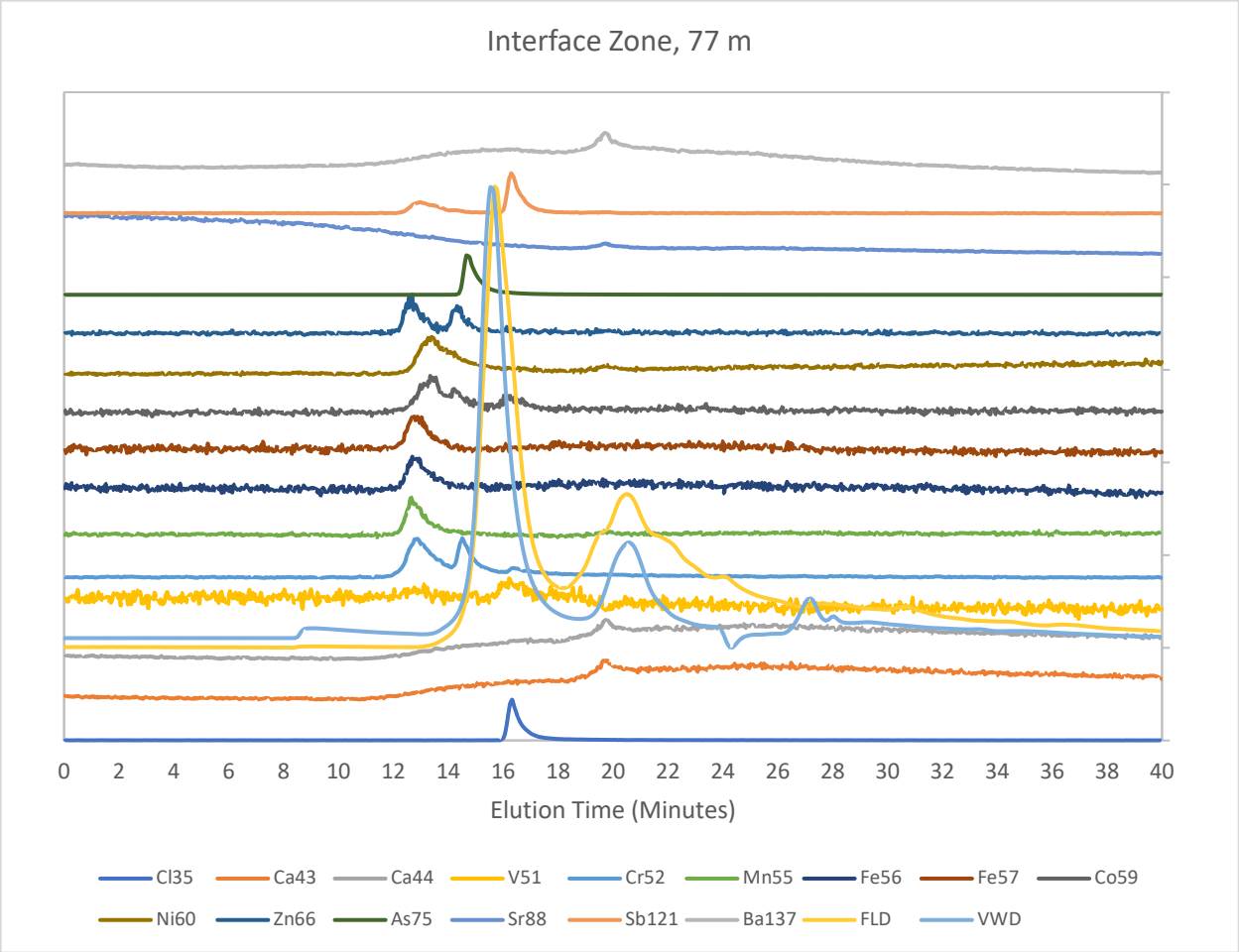

Figure 30. Time-matched chromatograms of ICP-MS data (primary axis) and FLD data (secondary axis) for an interface sample. The positions on the y-axes are arbitrary.

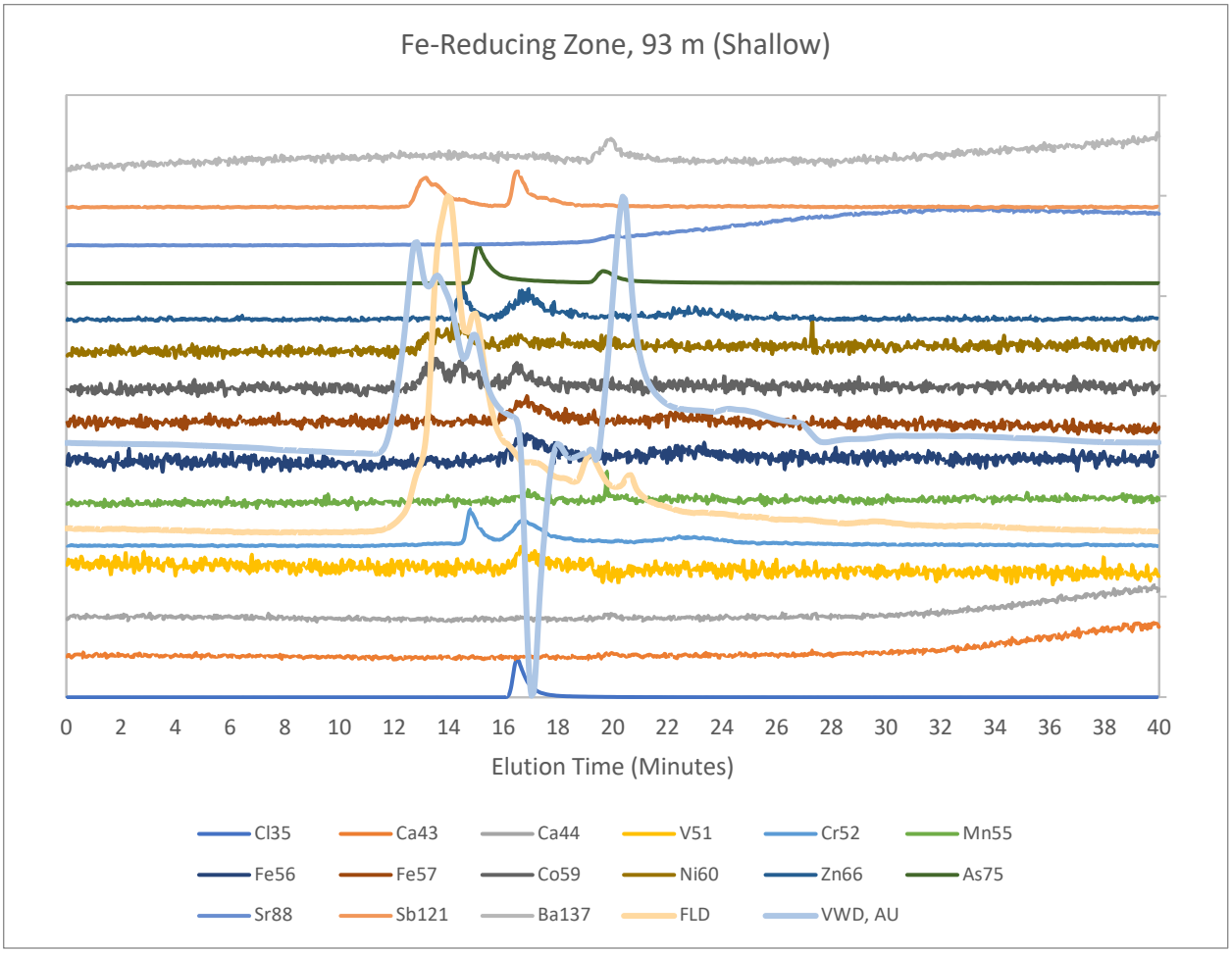

Figure 31. Time-matched chromatograms of ICP-MS data (primary axis) and FLD data (secondary axis) for an Fe-reducing sample. The positions on the y-axes are arbitrary.

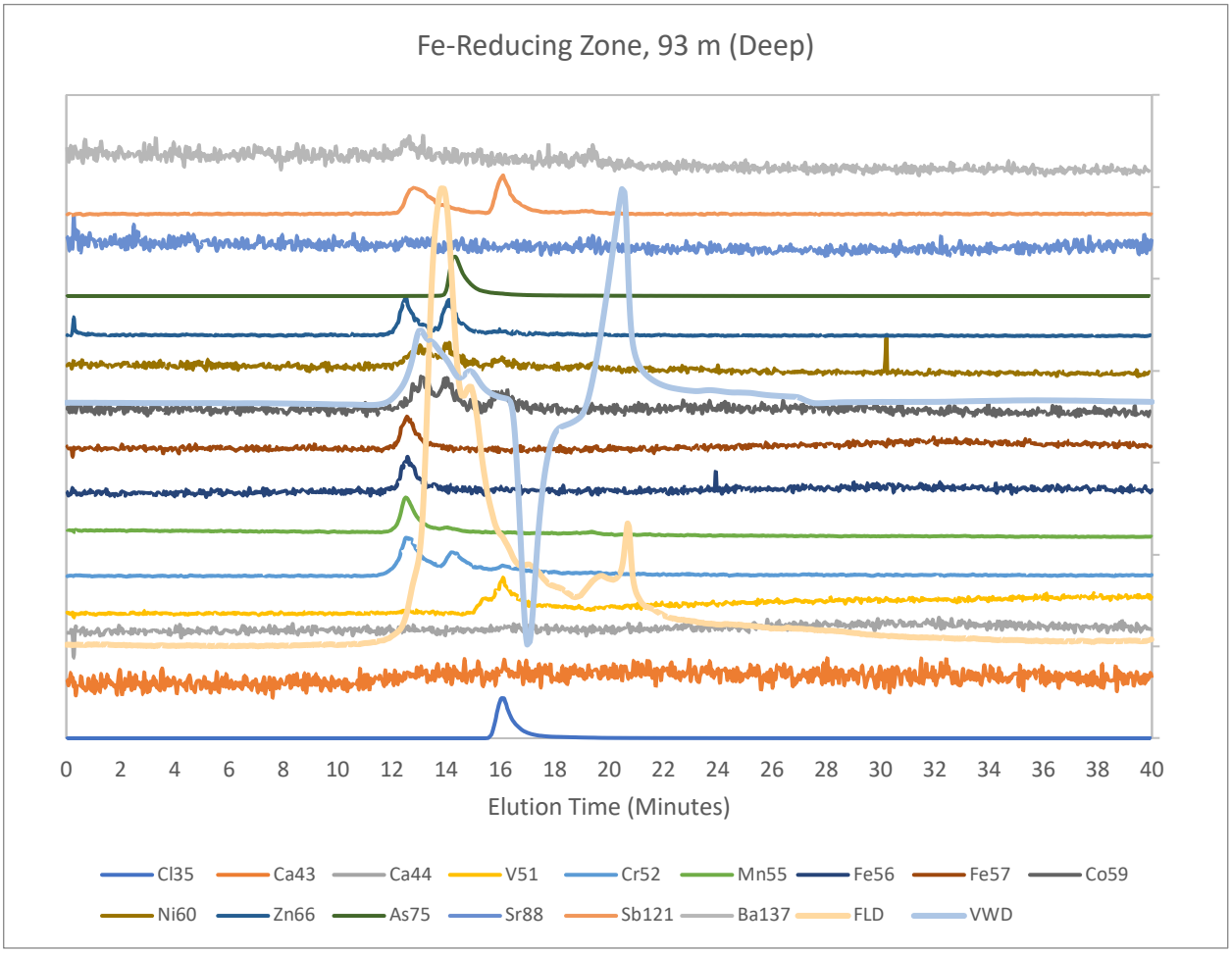

Figure 32. Time-matched chromatograms of ICP-MS data (primary axis) and FLD data (secondary axis) for an Fe-reducing sample. The positions on the y-axes are arbitrary.

Table 6. Retention Time of Trace Elements in DOM Elution Range

Element	1909-42	2321-105	1523-45	1418-50	1418-118
Cl35	16.5	16.5	16.5	16.5	16
Ca43	20	-	12	-	-
Ca44	20	-	12	-	-
V51	16.5	16	-	-	16
Cr52	12.5, 14.5	12.5	12.5, 14.5	15, 17	12.5, 14, 16
Mn55	12.5	12.5	12.5	-	12.5
Fe56	12.5	12.5	12.5	17	12.5
Fe57	12.5	12.5	12.5	17	12.5
Co59	14.5, 16.5	13, 16?	13.5, 14, 16.5	13.5, 14.5, 16.5	13, 14, 16
Ni60	14, 19.5?	13.5	13.5	14	13, 14, 16
Zn66	12.5, 14.5	12.5, 13.5	12.5, 14.5	14.5, 16.5	12.5, 14
As75	14.5	14.5	14.5	15, 19.5	14.5
Sr88	19.5	-	20	19	-
Sb121	13, 17.5	16.5	16.5	13, 16.5	12.5, 16
Ba137	20	19.5	10-33	20	12.5, 19.5
FLD	11-40	12-23	13-32	12-30	12-29
VWD	11-28	12-28	8-28	12-28	12-28

Alkaline Organic Extraction Analyses: PARAFAC

Four unique components were identified in the EEM spectra model. Component 1 (C1) (Figures 33-34, purple) plotted in the 250-350 nm region for excitation, and in the 350-500 nm

range for emission, characteristic of a combination of an A and C peak. Component 2 (C2) (Figures 33-34, blue) plotted in the 250-400 nm range for excitation, and in the 400-550 nm range for emission, characteristic of an A and C peak combination with a stronger C peak signal. Component 3 (C3) (Figures 33-34, green) plotted in the 250-300 nm range for excitation, and the 300-400 nm range for emission, characteristic of a T peak. Component 4 (C4) (Figures 33-34, yellow) plotted in the 250-350 nm range for excitation, and the 350-500 nm range for emission, characteristic of a M peak.

The relative abundances of each component were compared between samples of groundwater in the contaminant plume and samples of aquifer sediment to observe any organic transformations that may have resulted in a shift in component signatures. Changes in component signatures may have indicated mobilization or sequestration of any of the components. One background sediment sample was characterized, but no background well samples were included in the model. In the background sediment sample (denoted as TRINITY_1909_42_F1 on Figure 34), C4 was the dominant component, followed by C1, with a slight increase in C3 over C2.

The five sediment samples informing the model contained greater abundance of each of the four components than did the 15 well samples. Within the plume sediments, depth appeared to influence the overall abundance of components more so than distance; the two very deep samples were more similar despite being in different zones (interface, TRINITY_2321_105_F1, and Fe-reducing, TRINITY_1418_118_F1) than the very deep Fe-reducing sample was to the medium depth sample taken from the same core (TRINITY_1418_42_F1). In the two interface samples (TRINITY_2321_105_F1 and TRINITY_1523_45_F1), C2 had the greatest relative abundance and C3 had the least, but the medium depth sample had more C4 than the very deep sample. In the Fe-reducing sediment taken from the same core at different depths, C4 was most

abundant in the medium depth samples, followed by C1, while C1 was most abundant in the very deep sample, followed by C4.

Component 4 had a much higher signal in the sediment samples than the well samples. In the majority of well samples, C4 did not occur at all. It only occurred in slight amounts in three wells sampled from the middle of the Fe-reducing zone, at 101 m, 102 m, and 105 m (BEMIDJI_9315A, BEMIDJI_9315B, and BEMIDJI_510, respectively). In the 15 well samples, C1 had the highest signal, followed by C3, then C2. Components 2 and 3 both appeared to decrease with distance from the edge of the plume. Well sample 9315A had higher signals for each of the four components than all other wells and was more similar to the average sediment sample. Shallower well samples had slightly greater abundances of all components than deeper well samples.

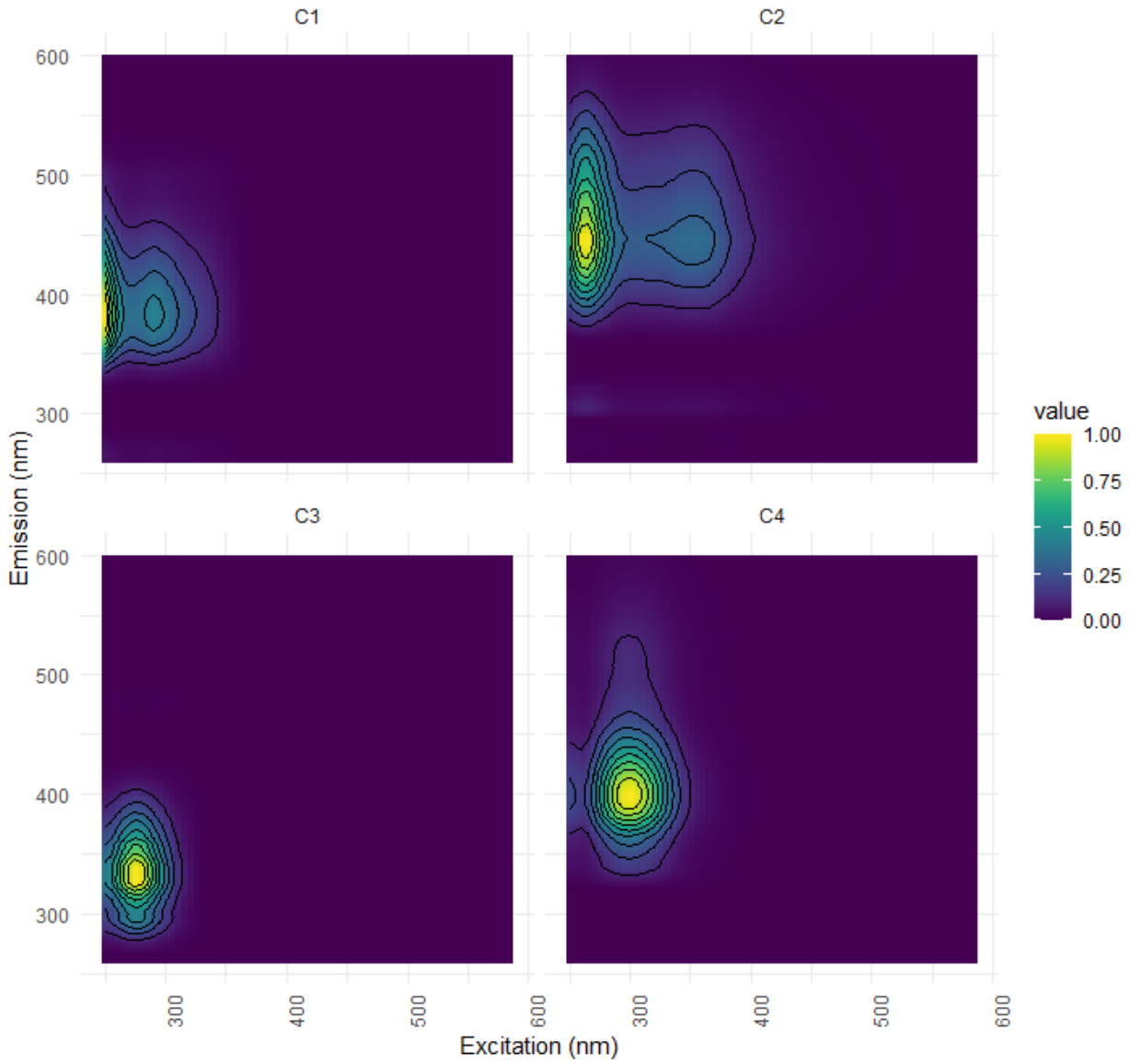

Figure 33. EEM spectra for four identified components: Component 1 (top left), Component 2 (top right), Component 3 (bottom left), and Component 4 (bottom right). PARAFAC modeling was informed by 15 well samples and 5 sediment samples.

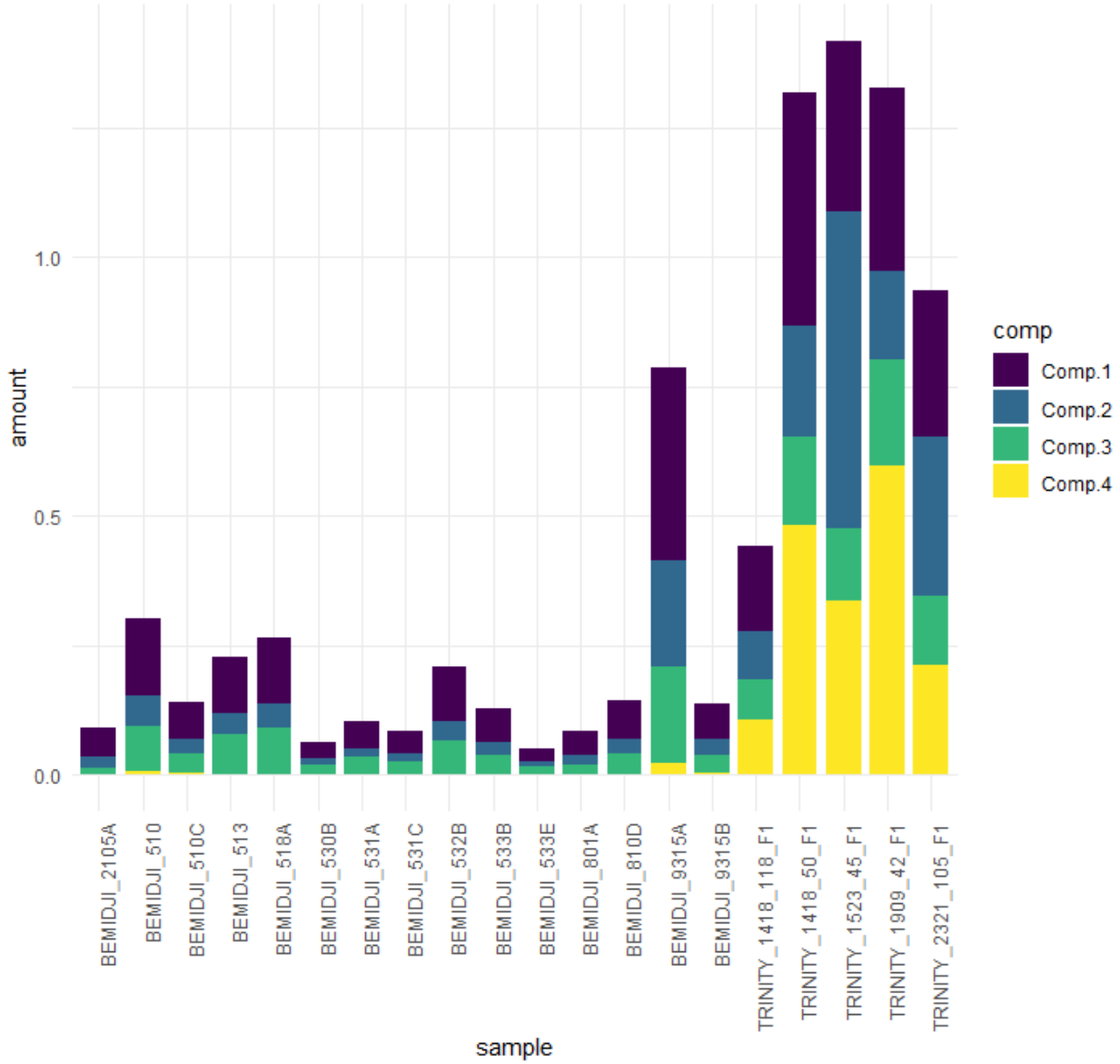

Figure 34. Composition of four identified components by sample. PARAFAC modeling was informed by 15 well samples and five sediment samples.

IV. Discussion

Complex elemental cycling is present at the Bemidji site both temporally and spatially as the contaminant plume has advanced downgradient through time and caused evolving redox zones. In an effort to improve understanding what of processes are causing elemental mass transfer, it is important to consider which geogenic mineral or organic phases function as sources of trace elements in native background sediments and/or function as sinks downgradient from the oil body.

Oxides and hydroxides as sources of trace elements

Redox-sensitive oxides are particularly vulnerable to an influx of organic carbon. After the oil spill, rapid proliferation of the microbial community drove the aquifer to anoxia, giving way to the reductive dissolution of Mn(IV)- and Fe(III)- oxides due to the lack of nitrate in groundwater. Berndt (1987) identified oxide minerals (inclusive of SiO_2) as comprising 76.9% to 92.7% of the bulk chemical composition, depending on grain size examined. Fe_2O_3 ranged from 0.98% to 7.6%, while MnO ranged from 0.01% to 0.09% (Berndt, 1987). Reduction of Fe(III) and Mn(IV) hydroxides through the biodegradation of hydrocarbon aids in the mobilization of significant masses of these associated trace elements into groundwater (Appendix A).

In the background sediment, oxides and hydroxides are a source of the majority of trace elements. Oxides and hydroxides comprise the highest concentration in background sediments for Al, As, Ce, Co, Cr, Fe, La, Mg, Mn, Ni, Pb, and Si, per the sequential extraction chemical analyses. Some elements, like Al, appear relatively non-reactive, likely due to their presence in mineral lattices of redox-insensitive oxides. For Ba, Ca, Co, Fe, Mg, Mn, and Pb, concentrations are significantly higher in the oxide and hydroxide phases of the background sediment than in the same phase of the Fe-reducing sediment, suggesting that they serve as a native source of these

elements that are mobilized due to geochemical reactions in the plume (Table 5). However, these elements are not all significantly depleted in the methanogenic and interface sediment. This suggests an unusual trend wherein mass mobilization of trace elements occurs between the interface and Fe-reducing zones that is yet to be characterized.

The PCA biplot of oxides and hydroxides (Figure 26) indicates a greater abundance of trace elements associated with oxides and hydroxides in the background than in any other zone, with the exception of As, Cr, and Zn. Previous characterization of the aquifer profile with an emphasis on Fe concluded that methanogenic sediment was depleted in Fe(III) oxides compared to the Fe-reducing zone (Zachara et al., 2004). Ziegler et al. (2017b) estimate that more than two thirds of the reducible Fe(III) has been reductively dissolved.

This higher concentration of the aforementioned metals in background sediment is attributable to their association with reducible Fe and Mn oxides. In the most contaminated sediments near the oil, which are now methanogenic but historically were Fe- and Mn- reducing, elemental concentrations in association with oxides and hydroxides are much lower than in background sediment (Table 5). High concentrations of Mn were mobilized in groundwater downgradient from the oil body as recorded in groundwater chemical analyses conducted in 1986 (Appendix A), resulting from Mn(IV) reduction, suggesting Mn mobilization began early in the contaminant plume's history. Fe-reduction began in earnest upon the depletion of Mn minerals.

Elemental mobilization from oxide and hydroxide phases is highlighted in the four elements examined in Jones et al. (2023), wherein long-term biodegradation had mobilized the majority of cations from the sediment, resulting in low (but detectable) trace element associations with Fe(III) hydroxides in the most contaminated sediments. Groundwater chemistry data show evidence of substantial Mn-reduction in 1986 in the form of Mn concentration in groundwater

exceeding 6000 to 8000 µg/L spanning 38 to 94 m downgradient from the oil spill (Appendix A). By comparison, Mn-reduction largely had ceased by 2022, when the highest dissolved Mn measured at 667 µg/L (Appendix A). Fe-reduction had not yet started in a substantive way in the mid-1980s, with the exception of wells immediately adjacent to the oil body (Appendix A). Despite evidence of widespread Mn reduction early in the plume's history, contemporaneous investigations of some sediment-bound trace elements did not see evidence of mobilization (Berndt, 1987). This suggests that trace elements may not be appreciable in the Mn fraction of reducible oxides, and they only leach into groundwater when Fe-reduction becomes the dominant TEAP. Alternatively, the rate of trace element dissolution from sediments is kinetically slow, such that significant differences were not measurable only seven years after the spill, whereas substantial differences were measurable in the 2010s and 2020s, after decades of widespread Mn and Fe-reduction, which is still ongoing (Appendix A).

Organic matter as sources of trace elements

Generally, organic matter serves as a smaller geogenic repository for trace elements than oxides or carbonates, as shown in the sequential extraction data (Table 2). However, some elements have detectable associations with organic matter in background sediment, most notably Ca and Mg (as well as Al, As, Ba, Ce, Fe, La, Mn, Ni, Si, Zn), indicating the presence of natural organic matter in the aquifer sediment independent of the oil spill (Figures 6-8, 11, 15-16, 18-19, 21, and 23). It is possible that these natural sources could be oxidatively dissolved via biodegradation by proliferated microbial communities that were stimulated by an influx of organic carbon from the oil.

A comparison of the fluorescence and UV organic matter signals in background sediment (Figure 28) compared to sediments in the plume (Figures 29-32) show a greater abundance of lower molecular weight organics in the background. The loss of these low molecular weights in the plume suggest that they were mobilized via microbial oxidation. Metals in the background sediment associated predominantly with the higher molecular weight fraction, so the mobilization of the lower molecular weight fraction is not consequential for trace metal mobilization (Figures 28-32). Interestingly, Ca peaks were observed around 20-min in the background (Figure 28), associated with lower molecular weight organic matter that is either depleted or diminished from the samples within the plume, such that Ca peaks are similarly missing or lower in the plume sediment (Figures 29-32). The Ca observations on the chromatograms align with the data from the Wilcoxon tests, wherein Ca and Mg were the only elements that were significantly depleted in the Fe-reducing zone relative to the background.

An additional source of organic matter in the aquifer is the crude oil itself, which is composed mainly of saturated aliphatic hydrocarbons (58-61%) that have created a marked shift in the organic composition of sediments in the plume (Eganhouse et al., 1993). In the plume sediment, 63-75% of the extractable organics originated from the saturated hydrocarbon fraction compared to 4-10% of the same fraction in uncontaminated sediment (Eganhouse et al., 1993). Since the spill, the aliphatic hydrocarbon body has been oxidatively dissolved by biodegradation while sitting atop the water table (Cozzarelli et al., 1990). While the terminal endpoint of hydrocarbon biodegradation is mineralization to CO_2, recent research has demonstrated that the biodegradation process has yielded oxidized organic carbon intermediates with oxygen-containing functional groups that have partitioned into the groundwater (Podgorski et al., 2021). As a result, increased dissolved organic matter has been reported in the plume in both older (Eganhouse et al.,

1993) and more recent studies (Bekins et al., 2016; Podgorski et al., 2021), the latter of which document polar degradation products traveling far beyond the extent of the hydrocarbon plume. The biodegradation of saturated aliphatic hydrocarbons has increased the concentration of aliphatic acids in particular near the oil body (Cozzarelli et al., 1990), which facilitated the dissolution of carbonate and silicate minerals, resulting in greater elemental release from source minerals compared to aromatic acids (Lazo et al., 2017). Furthermore, shorter carbon chain length and more hydroxyl functional groups also released greater quantities of elements (Lazo et al., 2017). Therefore, mobilized trace elements may be originating both from natural organic matter and contaminant organic matter at the Bemidji site.

Crude oil sampled from the site contained detectable amounts of Ni (4.30 ppm), Fe (7.02 ppm), Cr (210 ppb), Co (28.8 ppb), and Zn (746 ppb) (Cozzarelli and Baedecker, personal communication). However, the phase of these metals (organically complexed, free ions) is unknown. The biodegradation of the crude oil at the Bemidji site may have resulted in the mobilization of these elements into groundwater and subsequent attenuation by sediments, as evidenced by concentrations of Cr, Fe, and Ni in the organic phase of the plume sediment that are statistically significantly higher than in the background sediment organic phase (Table 5). In particular, Cr serves to illustrate this point as there is no phase wherein Cr is statistically depleted in the plume sediments relative to the background sediment, suggesting that background sediments do not act as a source for Cr measured in groundwater (Appendix A). Thus, a non-native source of Cr contamination can be inferred.

In my PARAFAC model of the organic matter composition in groundwater and sediment, the EEMs of C1 and C2 express maxima in the characteristic A and C peak regions, suggesting that they comprise a humic-acid like signature both in the background and contaminated plume

sediment (Figures 33-34) (Coble et al., 2014). The presence of C1 and C2 in the background suggest biogenic organic matter existing in the uncontaminated sediment. These components agree with EEMs components measured in groundwater by Podgorski et al. (2018), who identified six components in Bemidji well samples, three of which (C3, C4, and C6) indicated humic and/or fulvic excitation-emission spectra, which may bind cations via carboxyl functional groups.

Component 3 from the current study was identified as a tryptophan-type (T) peak (Coble et al., 2014). C3 closely aligned with C5 from Podgorski et al. (2018), who similarly identified a T peak in groundwater and hypothesized that part of the signal was comprised of dissolved polynuclear aromatic hydrocarbons, which are indicative of the presence of a contaminant source (Coble et al., 2014). In the current study, C3 appeared in both background and plume sediments and plume well samples (Figure 34), suggesting some natural presence of tryptophan-like fluorescing organic matter. However, the well sample 252 m downgradient, outside of the current hydrocarbon plume, had the lowest amount of C3. This may indicate a decrease in dissolved polynuclear aromatic hydrocarbons with distance from biodegradation in the plume samples, returning to background concentrations of C3.

Sediment samples contain a larger fraction of component C4 than groundwater samples. C4 is identified as a M peak (Figure 33), which usually indicates recent microbial activity in the sediment (Coble et al., 2014). This peak is only present in small amounts in three well samples in the current study and was not identified as a component in Podgorski et al. (2018). M peaks have not yet been documented in groundwater samples, though as the peak originates from recent microbial activity, it is possible that high microbial activity in a given region could be reflected in the organic components of the groundwater (Coble et al., 2014). Wells located at 101, 102, and

105 m from the oil body had a small amount of C4, which could be caused by those wells being in the middle of the modern Fe-reducing plume.

The presence of C4 is much higher in the sediment samples than in groundwater, often constituting the most prevalent component. Interestingly, C4 is strongest in the background sediment sample and lower within the plume sediment, which may indicate that aerobic degradation is the source of recent microbial activity. The relative loss of C4 in the plume might suggest that this OM fraction is the mobilized fraction of OM observed in the chromatograms in the 22- to 28-min retention time range (Figures 28-32). This finding might be supported by that of Podgorski et al. (2021), who identified that microbes are degrading low molecular weight, aliphatic OM, while higher molecular weight aromatic and acyclic OM persisted within the plume. Podgorski et al. (2021) did not however postulate the degradation of low molecular weight, aliphatic OM as being associated with an M peak.

It is possible that naturally-occurring organic matter had formed complexes with trace elements, and may not have been mobilized if not for biodegradation from a changing geochemical environment. However, declining levels of C4 in the plume sediment do not match with decreasing trace elements in the organic fraction within the plume, implying that C4 is not a significant source of metals in the background. Other sediment samples taken downgradient in the interface or Fe-reducing zone, but at shallower levels, have component composition more similar in appearance to the background sediment than to the deeper cores in the Fe-reducing zone (Figure 34). This suggests that samples at greater depth within the reducing region of the plume, instead of near the upper plume boundary near the water table, have lower concentrations of each component, indicating that these natural sources of OM are being biodegraded and mobilized in the plume.

Carbonates as sources of trace elements

The dominant carbonate minerals in the background sediment of the Bemidji aquifer are calcite and dolomite, comprising 4.1-6.9% of the bulk sediment (Bennett et al., 1993). Similar values for carbonate composition of the aquifer were identified by Berndt (1987), which determined carbonates constituted 5-9% of the sediment. Uncontaminated groundwater chemistry is largely controlled by the dissolution and precipitation of carbonate minerals (Bennett et al., 1993), with hydrochemical facies dominated by a Ca-HCO_3 water type (Appendix A). Results from this study indicate that Ca and Mg in carbonates are statistically more concentrated in background sediment than sediment within the plume (Table 5), suggesting that calcite and dolomite are highly mobilized due to biogeochemical processes induced by the plume. A similar trend is seen for B, which likely is substituting into the mineral lattice of carbonates as borate (BO_3^{3-}) in the place of CO_3^{2-} (Farmer et al., 2019), and was extracted in the same stage of the sequential extraction (Figure 25). Background carbonates were associated with trace amounts of Ba, Sr, Co, Ni, Ce, and La likely as impurities in the mineral lattice of calcite and dolomite. However, only Ba, Ni, Sr, along with Ca, Mg, and B were statistically higher in background sediments than sediments in the plume (Table 5), suggesting that not all trace elements are mobilized equally from native carbonate minerals.

Carbonates present in native sediment likely were mobilized through the production of organic acid intermediates as microorganisms degraded hydrocarbon contaminants and through acidity produced during methanogenesis (Cozzarelli et al., 1990; Bennett et al., 1993). Carbonate dissolution is evidenced by increased concentrations of Ca, Mg, and HCO_3^- in the contaminated groundwater when compared to the background groundwater (Berndt, 1987). Groundwater in

2011 and 2021 showed increasingly elevated concentrations of dissolved Ca downgradient of the oil body with time, likely from the onset of methanogenesis and subsequent acid production in the zone nearest to the oil spill site (Appendix A). The increased partial pressure of CO_2 and decreased pH associated with microbial metabolism further enhance the dissolution of carbonate minerals in the sediment (Berndt, 1987); this phenomenon may extend into the modern methanogenic zone, where groundwater pH has been measured as low as 5.5 (Jones et al., 2023).

Oxides and hydroxides as sinks for trace elements

For all examined elements aside from Cr, trace elements in oxides and hydroxides did not have a significant increase in concentration in sediments in the plume compared to the background. In fact, I observed statistically significant depletion of a host of elements from oxides and hydroxides in Fe-reducing sediment relative to background sediment and previous zones, including Ba, Ca, Ce, Co, Fe, La, Mg, Mn, Ni, and Pb (Table 5). These results suggest that oxides and hydroxides do not play a major role in attenuating trace elements within the geochemical zones sampled for this study. It is likely that elements remain mobilized and could be sequestered by oxides and hydroxides further downgradient than the Fe-reducing zone. Within the 100 m downgradient range examined for this study, the furthest sediment samples lie within the middle of the Fe-reducing zone. Bennett et al. (1993) suggested that Fe oxyhydroxides precipitate out at the leading front of the anoxic plume as groundwater intermingles with regionally oxic water, removing dissolved Fe from solution. This precipitation of Fe oxides and hydroxides may was later observed by Tuccillo et al. (1999) and termed the iron curtain. Zachara et al. (2004) identified greater amounts of Fe(III) oxides in the Fe-reducing zone than in the methanogenic zone, in forms such as goethite and hematite, with less poorly crystalline Fe(III) oxides, providing further evidence of the iron curtain. The presence of an iron curtain is critical for trace element cycling,

as an abundance of sorption sites can further sequester dissolved trace elements from groundwater and prevent them from traveling further downgradient. However, at the distances examined, oxide and hydroxide phases do not serve as effective sinks because no samples of the sub-oxic leading edge of the anoxic plume are included in this study.

Despite being effective at removing trace elements from groundwater, a 2015 resampling of the iron curtain observed by Tuccillo et al., (1999) saw that Fe(III) oxides had been remobilized as the Fe-reducing zone expanded and reductively dissolved the iron curtain, reestablishing it further downgradient in an effect known as a roll front (Ziegler et al., 2017a). Current estimates based on groundwater chemistry put the leading edge of the anoxic plume at approximately 135-140 m downgradient in 2016 (Cozzarelli et al., 2016). Contemporaneous Fe measurements in sediment at the same distance showed the iron curtain formation (Ziegler et al., 2017a) and demonstrated the roll front effect when compared to Tuccillo et al. (1999) who observed the curtain was more proximal to the oil.

Although the precipitation of Fe oxides and hydroxides at the leading edge of the anoxic plume may serve as an effective means of limiting trace element transport (Ziegler et al., 2017a; Ziegler et al., 2017b), these sediments serve only temporarily as a sink for trace elements. The anoxic plume at this site has continued to migrate since the spill occurred in 1979, with a declining rate of advancement through time (Cozzarelli et al., 2001; Cozzarelli et al., 2016). Historically, when Fe-reducing conditions are established at the precipitated iron curtain, Fe reduction has re-mobilized trace elements into the groundwater (Ziegler et al., 2017a).

Predictive modeling of the plume's growth rate has suggested that the hydrocarbon plume will eventually begin to retract back toward the oil body (Ziegler et al., 2021). In fact, field data collected in 2022 and 2023 documented for the first time a retraction of the benzene plume from

136 m downgradient from the oil body in 2012 to 120 m downgradient in 2022 (Cozzarelli, personal communication; Ziegler, personal communication). The plume of dissolved Fe retracted both at the 1 mg/L concentration (150 m to 145 m downgradient) and the 10 mg/L concentration (135 m to 123 m downgradient) over the same timeframe (Cozzarelli, personal communication). The observed plume retraction may result in the most recent iron precipitates serving as the terminal iron curtain, which is unlikely to be remobilized. Thus, trace elements entrained in Fe oxides and hydroxides there are likely to become stable sinks.

Organic matter as a sink for trace elements

Arsenic, B, Cr, Fe, La, and Ni are associated with organics in sediment in greater concentrations within the plume compared to background sediment (Table 5). In the PCA biplot for the organic phase (Figure 27), the samples appear to group by zone, with background and interface sediment dispersed across positive PC1, methanogenic sediment in the negative PC1 and negative PC2 quadrant, and the Fe-reducing sediment in the negative PC1 and positive PC2 quadrant.

Elements complexed with organic matter are likely then being retained by heavier molecular weight OM, based its persistence within the plume. In stream water analyses, some metals (Cu, Ni, Co, Cr, Zn, Fe, Ce, and V) were observed to preferentially complex with larger molecular size OM (Wu et al., 2004). These observations agreed with our own, wherein V, Cr, Mn, Fe, Co, Ni, Zn, and As eluted at times similar to the heavier weight OM (Table 6). Sr, Sb, and Ba, with some secondary peaks of the previously mentioned metals, eluted at later times with lower weight OM (Figures 28-32). These elements are likely present in ternary complexes,

wherein metals with high affinities bond to both negatively charged functional groups and anions, forming a bridge (Wu et al., 2004; Aftabtalab et al., 2022).

Of particular interest are the three elemental vectors pointing into the Fe-reducing region of the PCA: As, B, and Cr (Figure 27). The association of these elements with organic fraction of the Fe-reducing zone is additionally reflected in the pairwise Wilcoxon tests. Arsenic in particular has a significant increase in organic association in the Fe-reducing zone relative to all other zones (Table 5). Given the lack of As-OM interactions in the background or at other locations within the plume for carbonates, oxides and hydroxides, and organics, this zone denotes differing geochemical behavior. B and Cr are significantly elevated in the Fe-reducing zone relative to the background and interface sediment (Table 5). Arsenic, Cr, and B are unique from the other analytes in that they form trivalent oxyanions, which appear to be complexing with organic matter present in the Fe-reducing zone, as previously observed in laboratory conditions (Ojeda et al., 2023; Martin et al., 2017). In chromatograms of the interface zone, As-OM and Cr-OM complexes are recorded at 70 m and 77 m downgradient and at 93 m in the Fe-reducing zone (Figures 29-32). Heavy metal-OM complexes are observed for several other trace elements as well, notably Co, Ni, Zn, Sr, Sb, and Ba, all of which had complexes in each of the interface and Fe-reducing samples examined (Figures 29-32). The PCA vectors for these elements point towards the methanogenic sediment samples on the biplot (Figure 27).

Interestingly, these two groups of elements have very different chemical properties: As, Cr, B, and Sb (which was excluded from PCA due to detection limit issues), form oxyanions, whereas Co, Ni, Zn, Sr, and Ba are all divalent cations. Organic matter generates negatively charged functional groups (typically carboxyl groups) in the pH range of the contaminant plume, which explains complexation of cations, but fails to explain anion complexation. However, given

the different anionic and cationic associations with organic matter within the plume, the grouping of zones within the organic PCA biplot could be a result of trace elements with different charges complexing with different organic functional groups (Figure 27).

The humic-like signature in C2 in the PARAFAC model is elevated within the plume relative to the background, highest in the interface samples and lower in the Fe-reducing samples (Figures 33-34). The increase in C2 within the plume is accompanied by higher concentrations of trace elements associated with the organic phase, suggesting that C2 may be a contributor in the attenuation of trace elements. Therefore, an array of both naturally occurring and crude oil-derived organic components may play a role in complexing with or attenuating trace elements within the plume.

Several functional groups or mechanisms could be attenuating the trace elements in the organic matter complexes. Some complexes of OM and the previously discussed trace elements are observed in the background sediment chromatogram (Figure 28). While this could indicate the formation of metalloorganic complexes as a mechanism of attenuation in the plume, it may also indicate that some of these complexes were natively occurring in uncontaminated sediment. If the latter were the case, it would suggest that Fe-reducing microbes may not be able to break down these complexes, hence their presence in the leading Fe-reducing region of the plume; subsequent redox reactions may be able to break down the complexes, removing them from geochemically more developed zones closer to the origins of the plume.

Carbonates as sinks for trace elements

Groundwater chemistry from 1986, 2011, and 2021 shows increasing concentrations of dissolved Ca through time in the region nearest the oil body. In each year examined, the dissolved

Ca concentration decreases with increasing distance from the center of the oil body (Appendix A). However, concentrations were still high relative to the dissolved Ca in background sediment. Dissolved Mg concentrations slightly decreased through time, with the highest concentrations observed throughout the plume in 1986, and declining slightly in 2011 and 2021 (Appendix A). Berndt (1987) theorized that decreasing concentrations of Ca, Mg, and bicarbonate further downgradient from the oil body could suggest precipitation of carbonate minerals downgradient near the edge of and outside of the Fe-reducing plume. My data suggest that precipitation likely occurred differentially in sediments in all zones of the plume. As the plume has evolved and migrated throughout time, carbonate minerals precipitated in the Fe-reducing zone may have been mobilized by organic acids produced during subsequent methanogenesis in the same region, resulting in continuous elemental cycling in the carbonate phase until stabilization of plume expansion. However, thermodynamic favorability of carbonate minerals may be influencing the stability of the carbonate phase.

The distribution of samples in PC space on the carbonates PCA biplot (Figure 25) appears to show a slight grouping by geochemical zone. Vectors create an arc-like array from the background samples through the methanogenic samples and into the interface samples. The majority of elemental vectors (Al, Sr, Ni, La, Ba, Co, Cr, Mn, Zn, Ce, Cu, and Si) point into the methanogenic-grouped samples, whereas Pb and Fe vectors point into the interface zone. These different zones likely indicate where in the plume these carbonates have precipitated.

Extensive biodegradation activity has resulted in organic C mineralization to CO_2 in the aquifer, leading to CO_2 supersaturation (Bennett et al., 1993). Several elements (Pb, Fe, and Mn) that predominantly originated in oxide and hydroxide phases but were mobilized during Fe- and Mn- reduction precipitate as carbonates in the plume, despite little-to-no carbonate association in

the background sediment (Table 2). Mn and Pb are elevated in the methanogenic and interface zones relative to both the background and Fe-reducing zone sediment (Table 5), while Fe associated with carbonates is elevated in all plume sediment compared to the background (Table 5). In SEM-EDX, the medians for Ba, Co, and Ni all increased in methanogenic carbonates compared to background sediments, suggesting that their carbonate precipitation serves as a sink for these metals in methanogenic sediments, in agreement with PCA (Figure 25). Ba, Ni, and Sr are significantly higher in the background and methanogenic zone sediment compared to the Fe-reducing zone sediment (Figure 5). This supports the accumulation of these metals into carbonate mineral structures within the methanogenic zone sediment.

The most thermodynamically favorable divalent metal carbonates with the highest formation constants (K_f) appear to precipitate in the region closest to the center of the oil body, the methanogenic zone, while less thermodynamically favorable metal carbonates (lower K_f) generally precipitate in zones further downgradient from the spill site in the interface and Fe-reducing zones (Figure 25). Ca and Mg are much higher in the background sediment and therefore skew the vectors' locations. The formation constants of divalent carbonates decrease from $SrCO_3$ > $BaCO_3$ > $CaCO_3$ > $MgCO_3$ > $MnCO_3$ > $ZnCO_3$ > $FeCO_3$ > $PbCO_3$; a full table of carbonate mineral formation constants can be found in Appendix C, informed by Robie and Hemingway (1995). The Pb and Fe carbonates have a unique position relative to other carbonates, accumulating mostly further downgradient in interface sediments due to their comparatively lower K_f values compared to other metals.

Groundwater in the anoxic plume is supersaturated with respect to metal carbonates from decades of biodegradation, reflected in the increasing dissolution rates of divalent carbonates between pH 5 and 8, in the order Ni < Mg < Co < Fe < Mn < Zn < Cd < Sr $\leq$ Ca = Ba = Pb

(Pokrovsky & Schott, 2002). As pH continues to decrease, the rates of dissolution for the metal carbonates increase (Pokrovsky & Schott, 2002). Within the Bemidji plume, the pH ranges from 5.5 near the oil to 7.4 near the leading edge of the plume (Jones et al., 2023; Berndt, 1987). Groundwater supersaturation of metal carbonates creates conditions favorable to the precipitation of carbonate minerals.

Ca and Mg are statistically significantly higher in the background compared to the Fe-reducing sediment samples. This suggests that Ca and Mg are likely being mobilized from the background under Fe-reducing conditions. Given the spatial evolution of the plume, as the modern methanogenic zone was once Fe-reducing, the fact that Ca is not statistically different between the methanogenic and interface zones and the background could be explained by calcite and dolomite precipitating out in the methanogenic and interface zones. If this were the case, it would place $CaCO_3$ precipitation in alignment with the expected thermodynamic conditions based on the precipitation locations of other carbonates with similar K_f values (Robie & Hemingway, 1995; Pokrovsky & Schott, 2002).

Mn was mobilized into groundwater in significant amounts soon after the oil spill occurred owing to reduction of Mn oxides, evident from high concentrations of dissolved Mn observed in groundwater downgradient from the oil body in 1986 (Appendix A). Coupled with increased partial pressure of CO_2 from biodegradation, the precipitation of Mn carbonates was thermodynamically favorable, resulting in significantly higher concentrations of Mn carbonates in the modern methanogenic and interface zone sediment as compared to the background sediment (Table 5). Groundwater chemistry in 2011 and 2021 show much lower concentrations of dissolved Mn than in 1986, suggesting either attenuation of Mn by sediment or dissolved Mn traveling downgradient beyond the wells under observation (Appendix A).

Ba, Co, and Ni are present in carbonate minerals in greater amounts in the methanogenic zone sediment than in the background sediment, while Sr is higher in background carbonates and is nearly depleted in methanogenic zone carbonates (Figure 5). Ba and Ni carbonates all have lower K_f values than that of Sr carbonates. However, Sr carbonates have higher rates of dissolution at the pH observed in the Bemidji plume (Robie & Hemingway, 1995; Pokrovsky & Schott, 2002). This possibly caused the depletion of Sr in the methanogenic zone. Thermodynamic favorability under anoxic, high-HCO_3^- conditions coupled with lower rates of dissolution may have sequestered greater concentrations of the trace elements into carbonate minerals in the methanogenic and interface zone sediment than would have otherwise occurred in the native background sediment due to.

Both Pb and Fe are highest in the background sediment in the oxide and hydroxide phases (Figures 15 and 20). However, in the interface zone within the plume, both Pb and Fe are present in carbonates at significantly higher concentrations while also being significantly depleted from oxides and hydroxides (Table 5; Appendix B). Pb and Fe carbonates appear to precipitate the furthest of the carbonates examined, appearing predominantly in the interface zone, whereas the majority of other trace elements associated with carbonates occur in the methanogenic zone (Figure 25). The K_f values for Pb and Fe carbonates are lower than other metals examined in this study, resulting in these elements remaining mobile for further distances until other more thermodynamically favored carbonates had precipitated.

Elements present in the methanogenic zone on the PCA biplot, but not examined as common carbonate minerals may be present in solid solutions of more thermodynamically favored carbonate minerals. The introduction of heavy metal contaminants in biomineralization of hydrocarbons by microbial degradation also influences which carbonate polymorph precipitated

in the biomineralization process (Disi et al., 2022), indicating the influence heavy metals can have on carbonate precipitation. Complex precipitates involving multiple heavy metals have also been observed in experiments of microbially-controlled biodegradation as hydrocarbons are transformed into CO_2 (Huang et al., 2022).

Silicates as sources and sinks for trace elements

Silicate weathering occurred early in the plume history, as shown by elevated dissolved Si up to about 50 m from the oil body in 1986 (Appendix A). Since then, the zone of elevated Si advanced downgradient, where all wells measured up to 107 m were more than double the Si concentration of uncontaminated groundwater (Appendix A). Jones et al. (2023) examined Ba, Sr, Co, and Ni to evaluate the possibility that silicates are a source of trace element mobilization and attenuation. All four elements had some degree of association with silicate minerals in the background sediment, but Sr in particular had the greatest affinity for silicates (Figure 4). These findings are consistent with those of Bennett et al. (1993), which identified increased concentrations of Sr, Na, K, and SiO_2 in groundwater within the plume, suggesting feldspars as a source of Sr in the aquifer sediment. Jones et al. (2023) did not identify any regions up to a distance of 93 m downgradient where silicates were acting as an apparent sink for Sr, Ni, or Co. However, Ba in the interface zone was more abundant in silicates than in the background or methanogenic zone, suggesting that it may have been sequestered by silicates.

The top of the core located at 77 m downgradient from the oil body (in the interface zone) has a heightened signature of Si, Ca, and Mg in the oxides and hydroxides phase, relative to all other samples in and out of the plume. Associated with the anomalous signature at 77 m downgradient are higher concentrations of Ce, Co, La, Mn, Ni, and Pb in the oxides and

hydroxides phase as well (Figures 10-12 and 16-21). Physical observations of the top of the core illustrate that the sample is a fine-grained, orange-brown, clay-rich sediment that is much finer than most other samples in this study. The Bemidji aquifer is comprised of less than 1% clay minerals, usually kaolinite, smectite, and/or chlorite (Bennett et al., 1993). While the extraction step targeting oxides and hydroxides was not intended to extract from clay silicates, the hydroxylamine hydrochloride may have dissolved Fe(III) oxide surficial coatings on the clay minerals, subsequently causing a degree of extraction from the clays themselves. Previous extractions using hydroxylamine hydrochloride have resulted in suspected reductive dissolution of the surface of clay minerals and any associated trace metals as well (Helios-Rybicka & Calmano, 1988). Potential extraction of the clay minerals in these samples may be responsible for the elevated concentrations of the trace elements discussed above at the upper elevations of the 77 m core.

Exchangeable surface ions as sources and sinks for trace elements

Exchangeable surface ions tend to be the most mobile phase in aquifer sediments. However, the precipitation issues encountered with running the $MgCl_2$ extractants on the ICP-MS limited the meaningful data obtained in this study. For the elements where exchangeable data were obtained, non-parametric Kruskall-Wallis tests indicated no significant difference in concentration between geochemical zones for any element but Ca (Table 4). Therefore, the exchangeable data were removed completely from further analysis in this study. Further characterization of the elemental cycling of the Bemidji aquifer would benefit from exchangeable surface ion data to gain a more complete picture of the mobilization and attenuation at play.

The role of sorption to mineral surfaces is an important and potentially mobile phase that would be ideal to consider, as previous extraction analyses focused on As characterization identified 73% and 78% mean values of sorbed As in the Fe-reducing zone (Ziegler et al., 2017a). While Ziegler et al. (2017a) hypothesized that As was adsorbed to Fe(III) hydroxides, their extraction method was driven by phosphate exchange for arsenate and arsenite, a mechanism generalized to any adsorbed As, not just that adsorbed to oxides and hydroxides. The pH in the Fe-reducing zone would suggest that only oxides would serve as a sorbent phase for As oxyanions. However, evidence from this study suggests that an organic-bound As ternary complexes containing bridging cations may be the main retention mechanism for As in the Fe-reducing zone. Further study is warranted to complete the picture of As cycling in the contaminant plume.

Implications

Research and monitoring at the Bemidji oil spill site over the last four decades have resulted in an incredibly well-characterized geochemical profile that allows us to assess trace element cycling with detailed context of the redox conditions and pH that might be affecting trace element mobilization and attenuation in a crude-oil contaminated aquifer. The extent of characterization of this aquifer, of the dissolved primary and secondary contaminant plumes, and of the oil body itself has allowed us to determine controlling mechanisms affecting the stability of mineral phases and trace metals associated with them. In particular, the new knowledge of elemental cycling derived from analysis of the Bemidji site can be extrapolated to other sites similarly dominated by methanogenesis and Fe-reduction and/or sites similarly contaminated by organic carbon.

Results from this study may be used to inform water quality processes at other contaminated sites, such Superfund Sites where the primary remediation strategy is monitored

natural attenuation. Some studies have considered the effect of geogenic contaminants mobilized as a consequence of organic carbon biodegradation. For example, a landfill leachate undergoing active Fe-reduction in an aquifer has elevated levels of As in groundwater due to its sorption to Fe oxides (Delemos et al., 2006). However, this study suggests that the scope of geogenic contaminants in groundwater is likely much wider at organic-contaminated sites than what has been previously considered, and the biogeochemical mechanisms affecting the mineral dissolution and formation is diverse and interrelated. Trace element mobilization from soils contaminated with crude oil is positively correlated with the volume of crude oil spilled (Wyszkowski and Kordala, 2022). The fate of contaminants mobilized at a more recently contaminated site may be broadly informed by the processes observed over the course of four decades of monitoring at the Bemidji site. However, from the effects of site-specific properties on trace element cycling, such as the propensity for denitrification and sulfate reduction not observed at Bemidji, need to be additionally be considered, as those redox processes were not explored in this study.

The source of organic contamination may also affect redox processes, and consequently the yield of geogenic contaminants. In an aliphatic-dominated contaminant source, like that at the Bemidji site, the risk of elemental mobilization is higher, owing to aliphatic acids' greater capacity for releasing trace elements from sediment compared to aromatic acids because of increases in hydroxyl functional groups and reduction in chain length (Lazo et al., 2017). The ability for oxidized organic carbon intermediates to partition into the groundwater is a phenomenon likely of concern for other sites contaminated with organic carbon. At the Bemidji site, complexation between organic matter in the aquifer sediment and groundwater indicates that OM is a phase that should be considered in assessing the sources and sinks of trace elements at contaminated sites.

Drinking water regulations for inorganic contaminants are established by using the acceptable levels on a by-element basis (U.S. Environmental Protection Agency, 2023). However, given the dynamic processes observed in this study, it suggests that overall water quality should be considered based on the holistic assessment of all contaminants present. In the case of secondary geogenic contaminants, biodegradation can release contaminants from numerous source minerals into the groundwater supply. The current by-element method of groundwater assessment does not adequately consider the total hazard presented by an amalgamation of trace element contaminants. Analogous holistic quality measurements are made in other sectors, such as for food products and non-water beverages, which are assessed using the EPA's Total Hazard Quotient, which examines metal ion concentrations in sum total instead of as the concentrations of individual metals (U.S. Environmental Protection Agency, 1989; Hague et al., 2008). Similarly, treated waste water is assessed using whole effluent toxicity measurements, which consider the total toxicity of the collective constituents present in discharge waters and adjusted to site specific parameters, providing a baseline assessment of water toxicity to be paired with other risk assessment analyses (Chapman, 2000). Clearly, frameworks exist that consider the toxic effects of total inorganic and organic contaminants as a whole, rather than on an individual basis. Our study suggests that it may be appropriate to assess groundwater resource quality under similar conditions in concert with existing maximum acceptable contaminant levels, in order to gain a more holistic picture of the state of water resources.

V. Conclusions

While monitored natural attenuation successfully degrades hydrocarbon contaminants from aquifer systems, the resulting changes to geochemical conditions causes the mobilization of secondary geogenic contaminants. Oxides and hydroxides are reductively dissolved throughout

the Mn-reducing and Fe-reducing zones, releasing Fe, Mn, and Pb to groundwater. Sediment 100 m downgradient of the oil body remain depleted in trace elements associated with oxides and hydroxides, indicating that oxides do not become an appreciable sink within the extent of anoxic plume analyzed. Carbonate minerals are largely mobilized by biodegradation activity and lowering pH associated with H^+ from methanogenesis and organic acids produced as biodegradation intermediates. These acids then mobilize trace elements associated with carbonate minerals. However, with distance from the oil body, carbonate minerals precipitate with trace metals throughout the methanogenic and Fe-reducing zones, serving as the primary sink for trace elements in the anoxic plume. Carbonates likely serve as a sink for several trace elements mobilized from oxides and hydroxides, including Fe, Mn, and Pb. While trace elements are associated with native organic matter in sediment, there does not appear to be widespread mobilization of trace metals, as metals associate with larger molecular weight molecules, and microbial degradation only consumes the smaller molecular weight fraction. However, crude oil in the plume also contains Cr, Co, Ni, Fe, and Zn, although the form and solubility of these metals is not well characterized. Within the plume, dissolved trace elements are sequestered by complexing with heavier molecular weight OM in sediment. Mobilization and attenuation within the plume and downgradient extent shows evidence of a dynamic and interconnected system. Whole trace element analyses across multiple mineral phases provide a more accurate picture of element cycling in a contaminated aquifer, and may have applications to external systems similarly affected by methanogenesis and Fe-reduction resulting from hydrocarbon degradation.

VI. Bibliography

Aftabtalab, A., Rinklebe, J., Shaheen, S. M., Niazi, N. K., Moreno-Jiménez, E., Schaller, J., & Knorr, K. H. (2022). Review on the interactions of arsenic, iron (oxy)(hydr) oxides, and dissolved organic matter in soils, sediments, and groundwater in a ternary system. *Chemosphere*, *286*, 131790.

Amirbahman, A., Kent, D.B., Curtis, G.P.; Davis, J.A. (2006). Kinetics of Sorption and Abiotic Oxidation of Arsenic(III) by Aquifer Materials. *Geochim. Cosmochim*., *70*, 533−547.

Baedecker, M. J., Cozzarelli, I. M., Eganhouse, R. P., Siegel, D. I., & Bennett, P. C. (1993). Crude oil in a shallow sand and gravel aquifer—III. Biogeochemical reactions and mass balance modeling in anoxic groundwater. *Applied Geochemistry*, *8*(6), 569-586. https://doi.org/10.1016/0883-2927(93)90014-8

Bekins, B. A., Cozzarelli, I. M., Erickson, M. L., Steenson, R. A., & Thorn, K. A. (2016). Crude oil metabolites in groundwater at two spill sites. *Groundwater*, *54*(5), 681-691.

Bennett, P. C., Siegel, D. E., Baedecker, M. J., & Hult, M. F. (1993). Crude oil in a shallow sand and gravel aquifer—I. Hydrogeology and inorganic geochemistry. *Applied Geochemistry*, *8*(6), 529-549. https://doi.org/10.1016/0883-2927(93)90012-6

Berndt, M. P. (1987). Metal partitioning in a sand and gravel aquifer contaminated by crude petroleum, Bemidji, Minnesota. Master's Thesis. Syracuse University.

Boiteau, R.M., Shaw, J.B., Pasa-Tolic, L., Koppenaal, D.W., Jansson, J.K. (2018). Micronutrient metal speciation is controlled by competitive organic chelation in grassland soils. *Soil Biology and Biochemistry*, *120*, 283-291. https://doi.org/10.1016/j.soilbio.2018.02.018

Borch, T., Kretzschmar, R., Kappler, A., Van Cappellen, P., Ginder-Vogel, M., Voegelin, A., Campbell, K. (2010). Biogeochemical Redox Processes and their Impact on Contaminant Dynamics. *Environ. Sci. Technol., 44*(1), 15-23. https://doi.org/10.1021/es9026248

Chapman, P. M. (2000). Whole effluent toxicity testing—usefulness, level of protection, and risk assessment. *Environmental Toxicology and Chemistry: An International Journal*, *19*(1), 3-13.

Chou, L., Garrels, R.M., Wollast, R. (1989). Comparative study of the kinetics and mechanisms of dissolution of carbonate minerals. *Chemical Geology*, *78*(3–4), 269-82. https://doi.org/10.1016/0009-2541(89)90063-6

Coble, P. G. (Ed.). (2014). *Aquatic organic matter fluorescence*. Cambridge University Press.

Cozzarelli, I. M., Eganhouse, R. P., & Baedecker, M. J. (1990). Transformation of monoaromatic hydrocarbons to organic acids in anoxic groundwater environment. *Environmental Geology and Water Sciences*, *16*, 135-141.

Cozzarelli, I. M., Bekins, B. A., Baedecker, M. J., Aiken, G. R., Eganhouse, R. P., & Tuccillo, M. E. (2001). Progression of natural attenuation processes at a crude-oil spill site: I. Geochemical evolution of the plume. *Journal of Contaminant Hydrology*, *53*(3-4), 369-385.

Cozzarelli, I. M., Schreiber, M. E., Erickson, M. L., & Ziegler, B. A. (2016). Arsenic cycling in hydrocarbon plumes: secondary effects of natural attenuation. *Groundwater*, *54*(1), 35-45.

Delemos, J. L., Bostick, B. C., Renshaw, C. E., Stürup, S., & Feng, X. (2006). Landfill-stimulated iron reduction and arsenic release at the Coakley Superfund Site (NH). *Environmental science & technology*, *40*(1), 67-73.

Disi, Z.A., Attia, E., Ahmad, M.I., & Zouari, N. (2022). Immobilization of heavy metals by microbially induced carbonate precipitation using hydrocarbon-degrading ureolytic bacteria. *Biotechnology Reports*, *35*. https://doi.org/10.1016/j.btre.2022.e00747

Druschel, G.K., Emerson, D., Sutka, R., Suchecki, P., Luther, G.W. (2008). Low-oxygen and chemical kinetic constraints on the geochemical niche of neutrophilic iron(II) oxidizing microorganisms. *Geochimica et Cosmochimica Acta, 72*(14)*, 3358-3370.*

Eganhouse, R. P., Baedecker, M. J., Cozzarelli, I. M., Aiken, G. R., Thorn, K. A., & Dorsey, T. F. (1993). Crude oil in a shallow sand and gravel aquifer—II. Organic geochemistry. *Applied Geochemistry*, *8*(6), 551-567.

Farmer, J.R., Branson, O., Uchikawa, J., Penman, D.E., Hönisch, B., & Zeebe, R.E. (2019). Boric acid and borate incorporation in inorganic calcite inferred from B/Ca, boron isotopes and surface kinetic modeling. *Geochimica et Cosmochimica Acta*, *244*, 229-247. https://doi.org/10.1016/j.gca.2018.10.008

Hague, T., Petroczi, A., Andrews, P. L., Barker, J., & Naughton, D. P. (2008). Determination of metal ion content of beverages and estimation of target hazard quotients: a comparative study. *Chemistry Central Journal*, *2*, 1-9.

Helios-Rybicka, E., & Calmano, W. (1988). Changes in physio-chemical properties of some clay minerals by reducing extraction reagents. *Applied Clay Science*, *3*(1), 75-84. https://doi.org/10.1016/0169-1317(88)90007-5

Howarth, R. W. (2002). The Nitrogen Cycle. *Encyclopedia of Global Environmental Change*, *2*.

Huang, X., Zhang, R., Cui, M., & Lai, H. (2022). Experimental investigation on bioremediation of heavy metal contaminated solution by *Sporosarcina pasteurii* under some complex conditions. *Water*, *14*(4), 595.

Jones, K. L. (2020). Trace elements cycling in a crude oil-contaminated aquifer near Bemidji, Northern Minnesota. *Geosciences Student Honors Theses*. 20. https://digitalcommons.trinity.edu/geo_honors/20/

Jones, K. L, Ziegler, B. A., Davis, A. M., & Cozzarelli, I. M. (2023). Attenuation of barium, strontium, cobalt, and nickel plumes formed during microbial iron reduction in a crude-oil-contaminated aquifer. *ACS Earth Space Chem*., *7*(7), 1322-1336. https://doi.org/10.1021/acsearthspacechem.2c00387

Kalia, A., Sharma, S., Semor, N., Babele, P.K., Sagar, S., Bhatia, R.K., Walia, A. (2022). Recent advancements in hydrocarbon bioremediation and future challenges: a review. *3 Biotech, 12*(135). 10.1007/s13205-022-03199-y

Kleikemper, J., Pombo, S.A., Schroth, M.H., Sigler, W.V., Pesaro, M., Zeyer, J. Activity and Diversity of Methanogens in a Petroleum Hydrocarbon-Contaminated Aquifer. *Institute of Terrestrial Ecology, Swiss Federal Institute of Technology Zurich*.

Kojola, W. H., Brenniman, G. R., & Carnow, B. W. (1979). A review of environmental characteristics and health effects of barium in public water supplies. *Reviews on Environmental Health*, *3*(1), 79-95.

Lacey, Z. M. (2021). A modeling study of the mobilization and sequestration of trace metals in a crude-oil-contaminated aquifer. *Geosciences Student Honors Theses*. 22. https://digitalcommons.trinity.edu/geo_honors/22

Lazo, D. E., Dyer, L. G., & Alorro, R. D. (2017). Silicate, phosphate and carbonate mineral dissolution behaviour in the presence of organic acids: A review. *Minerals Engineering*, *100*, 115-123.

Léonard, A. & Lauwerys, R. R. (1980). Carcinogenicity, teratogenicity and mutagenicity of arsenic. *Mutation Research, Reviews in Genetic Toxicology*, *75*(1), 49-62. https://doi.org/10.1016/0165-1110(80)90027-5

Long, S.C., Aelion, C.M. (1999). Metabolite formation and toxicity measurements in evaluating bioremediation of a jet-fuel-contaminated aquifer. *Appl Biochem Biotechnol* , *76*, 79–97. https://doi.org/10.1385/ABAB:76:2:79

Martin, D.P., Seiter, J.M., Lafferty, B.J., & Bednar, A.J. (2017). Exploring the ability of cations to facilitate binding between inorganic oxyanions and humic acid. *Chemosphere*, *166*, 192-196. https://doi.org/10.1016/j.chemosphere.2016.09.084

Miyata, N., Tani, Y., Maruo, K., Tsuno, H., Sakata, M., Iwahori, K. (2006). Manganese(IV) oxide production by Acremonium sp strain KR21-2 and extracellular Mn(II) oxidase activity. *Appl. Environ. Microbiol*., *72*, 6467– 6473.

Morse, J. W., Luther III, G. W. (1999). Chemical influences on trace metal-sulfide interactions in anoxic sediments. *Geochimica et Cosmochimica Acta*, *63*(19/20), 3373-3378.

Murphy, K. R., Stedmon, C. A., Graeber, D., & Bro, R. (2013). Fluorescence spectroscopy and multi-way techniques. PARAFAC. *Analytical Methods*, *5*(23), 6557-6566.

Murphy, F., & Herkelrath, W. N. (1996). A sample-freezing drive shoe for a wire line piston core sampler. *Ground Water Monitoring and Remediation*, *16*, 86-90.

Naranjo, V.I., Hendricks, M., & Jones, K.S. (2020). Lead toxicity in children: An unremitting public health problem. *Pediatric Neurology*, *113*, 51-55. https://doi.org/10.1016/j.pediatrneurol.2020.08.005

Ng, G. H. C., Bekins, B. A., Cozzarelli, I. M., Baedecker, M. J., Bennett, P. C., & Amos, R. T. (2014). A mass balance approach to investigating geochemical controls on secondary water quality impacts at a crude oil spill site near Bemidji, MN. *Journal of Contaminant Hydrology*, *164*, 1-15.

Ojeda, A. S., Herron, C., Olshansky, Y., & Malina, N. (2023). Arsenic-dissolved organic matter complexation in water soluble extracts from lignite. *Chemosphere*, *342*, 140036.

Ollson, C.J., Smith, E., Herde, P., & Juhasz, A.L. (2017). Influence of sample matrix on bioavailability of arsenic, cadmium, and lead during co-contaminant exposure. *Science of the Total Environment*, *595*, 600-665. https://doi.org/10.1016/j.scitotenv.2017.04.036

Pavesi, T., & Moreira, J.C. (2020). Mechanisms and individuality in chromium toxicity in humans. *Journal of Applied Toxicology*, *40*, 1183-1197. https://doi.org/10.1002/jat.3965

Pfannkuch, H. O. (1979). Interim Report and Recommendations on Monitoring Program for Site M.P. 926.5, *Unpublished Consultant Report for Lakehead Pipe Line Company, Inc.*; Minneapolis, Minnesota.

Podgorski, D. C., Zito, P., McGuire, J. T., Martinovic-Weigelt, D., Cozzarelli, I. M., Bekins, B. A., & Spencer, R. G. (2018). Examining natural attenuation and acute toxicity of petroleum-derived dissolved organic matter with optical spectroscopy. *Environmental Science & Technology*, *52*(11), 6157-6166.

Podgorski, D. C., Zito, P., Kellerman, A. M., Bekins, B. A., Cozzarelli, I. M., Smith, D. F., ... & Spencer, R. G. (2021). Hydrocarbons to carboxyl-rich alicyclic molecules: A continuum model to describe biodegradation of petroleum-derived dissolved organic matter in contaminated groundwater plumes. *Journal of Hazardous Materials*, *402*, 123998.

Pokrovsky, O. S., & Schott, J. (2002). Surface chemistry and dissolution kinetics of divalent metal carbonates. *Environmental Science & Technology*, *36*(3), 426-432.

Pucher, M. (2023, June 15). *PARAFAC analysis of EEM data to separate DOM components in R.* The Comprehensive R Archive Network. https://cran.r-project.org/web/packages/staRdom/vignettes/PARAFAC_analysis_of_EEM.html#creating-a-parafac-model

Ratnaike, R. N. (2003). Acute and chronic arsenic toxicity. *Postgraduate Medical Journal 79*(933), 391-396. https://doi.org/10.1136/pmj.79.933.391

Robie, R. A., & Hemingway, B. S. (1995). *Thermodynamic properties of minerals and related substances at 298.15 K and 1 bar (105 Pascals) pressure and at higher temperatures* (Vol. 2131). US Government Printing Office. https://doi.org/10.3133/b2131

Siegel, D. I., Bennett, P. C., Baedecker, M. J., Berndt, M. P., & Franzi, D. A. (1985). Inorganic geochemistry of groundwater and aquifer matrix: First-year results. *U.S. Geological Survey Program on Toxic Waste – Groundwater Contamination: Proceedings of the Second Technical Meeting, Cape Code, Massachusetts, October 21-25.*

Sunderman, F. W., Hopfer, S. M., Sweeney, K. R., Marcus, A. H., Most, B. M., & Creason, J. (1989). Nickel absorption and kinetics in human volunteers. *Experimental Biology and Medicine*, *191*(1). https://doi.org/10.3181/00379727-191-42881

Swift, R. S. (1996). Organic matter characterization. In D. L. Sparks, A. L. Page, P. A. Helmke, R. H. Loeppert, P. N. Soltanpour, M. A. Tabatabai, C. T. Johnston, & M. E. Sumner (Eds.), *Methods of soil analysis: Part 3 Chemical Methods* (pp. 1011-1069).

Tessier, A., Campbell, P. G. C., & Bisson, M. (1979). Sequential extraction procedure for the speciation of particulate trace metals. *Analytical Chemistry*, *51*(7), 844-851. https://doi.org/10.1021/ac50043a017

Tuccillo, M. E., Cozzarelli, I. M., & Herman, J. S. (1999). Iron reduction in the sediments of a hydrocarbon-contaminated aquifer. *Applied Geochemistry*, *14*(5), 655-667. https://doi.org/10.1016/S0883-2927(98)00089-4

United States. Environmental Protection Agency. Office of Emergency, & Remedial Response. (1989). Assessing Human Health Risks From Chemically Contaminated Fish And Shellfish Guidance Manual. US Environmental Protection Agency.

United States. Environmental Protection Agency. (2023). *National Primary Drinking Water Regulations*, Washington, D.C. Retrieved from www.epa.gov/ground-water-and-drinking- water/national-primary-drinking-water-regulations.

Webster, J. D., Parker, T. F., Alfrey, A. C., Smythe, W. R., Kubo, H., Neal, G., & Hull, A. R. (1980). Acute nickel intoxication by dialysis. *Annals of Internal Medicine*, *92*(5). https://doi.org/10.7326/0003-4819-92-5-631

World Health Organization. (2022). *Guidelines for drinking-water quality: Fourth edition incorporating the first and second addenda*, Geneva, Switzerland.

Wu, F., Evans, D., Dillon, P., & Schiff, S. (2004). Molecular size distribution characteristics of the metal–DOM complexes in stream waters by high-performance size-exclusion chromatography (HPSEC) and high-resolution inductively coupled plasma mass spectrometry (ICP-MS). *Journal of Analytical Atomic Spectrometry*, *19*(8), 979-983.

Wyszkowski, M., & Kordala, N. (2022). Trace element contents in petrol-contaminated soil following the application of compost and mineral materials. *Materials*, *15*(15), 5233. https://doi.org/10.3390/ma15155233

Zachara, J.M., Fredrickson, J.K., Smith, S.C., Gassman, P.L. (2000). Solubilization of Fe(III) oxide-bound trace metals by a dissimilatory Fe(III) reducing bacterium. *Geochimica et Cosmochimica Acta*, *65*(1), 75-93.

Zachara, J. M., Kukkadapu, R. K., Gassman, P. L., Dohnalkova, A., Fredrickson, J. K., & Anderson, T. (2004). Biogeochemical transformation of Fe minerals in a petroleum-contaminated aquifer. *Geochimica et Cosmochimica Acta*, *68*(8), 1791-1805. https://doi.org/10.1016/j.gca.2003.09.022

Ziegler, B. A., Schreiber, M. E., & Cozzarelli, I. M. (2017a). The role of alluvial aquifer sediments in attenuating a dissolved arsenic plume. *Journal of Contaminant Hydrology*, *204*, 90-101.

Ziegler, B. A., Schreiber, M. E., Cozzarelli, I. M., & Ng, G. H. C. (2017b). A mass balance approach to investigate arsenic cycling in a petroleum plume. *Environmental Pollution*, *231*, 1351-1361.

Ziegler, B. A., Ng, G. H. C., Cozzarelli, I. M., Dunshee, A. J., & Schreiber, M. E. (2021). Arsenic in petroleum-contaminated groundwater near Bemidji, Minnesota is predicted to persist for centuries. *Water*, *13*(11), 1485.

VII. Acknowledgements

I would like to thank Trinity University's Semmes Scholars program, the Minnesota Pollution Control Agency, and the National Science Foundation (Award 2051747) for providing funding necessary to conduct this research. Thank you to Dr. Isabelle Cozzarelli, Jeanne Jaeschke, and Bridgette Polite from the United States Geological Survey for aiding us in running the ICP-MS and ICP-OES for our sequential extraction samples. Thank you to those at the USGS Minnesota Water Science Center. Thank you to Dr. Ann Ojeda and Dr. Natalia Malina at Auburn University for their assistance in examining the organic phase samples and conducting HPLC-SEC-ICP-MS, EEM, and PARAFAC analyses. Thank you to Dr. Frank Healy and Dr. Jennifer Steele at Trinity University for sharing lab resources to aid my research process. Thank you to Dr. Kathleen Surpless at Trinity University for acting as my thesis second reader and providing support throughout the process. To my research advisor Dr. Brady Ziegler, thank you for continually teaching me, advising me, and helping me grow as a researcher throughout the two years I've researched with you.

Appendix A: Groundwater chemistry data from various wells along the Bemidji north oil pool transect in 1986* (+/-1), 2011† (+/-2), and 2021† (+/-2)

well ID	m fr. oil center	Ca (mg/L)			Mg (mg/L)			Na (mg/L)			K (mg/L)			Si (mg/L)			Fe (mg/L)			Mn (µg/L)		
		1986	2011	2021	1986	2011	2021	1986	2011	2021	1986	2011	2021	1986	2011	2021	1986	2011	2021	1986	2011	2021
310E	-199	50.9	61.8	57.2	14.1	17.3	15.6	1.9	2.3	1.7	0.8	1.0	0.8	8.1	12.4	8.9	0.1	<0.1	0.0	11	1	<2
604A	-34	101.8	2.5	189.0	25.5	185.0	19.1	2.2		1.8	1.2	1.1	2.6	9.3	26.3	20.3	0.2		17.6	769	0	479
421	0	132.7	141.0	184.0	43.0	18.4	17.7	3.1	6.3	10.2	6.6	2.6	2.1	28.7	24.2	20.7	62.0	24.9	32.9	901	215	370
522	28	133.1	174.0	199.0	45.7	47.7	40.8	3.1	4.3	9.7	1.3	1.9	3.2	22.8	30.2	31.2	47.1	33.0	34.2	2599	214	
533D	38	151.9	187.0		45.0	37.3		3.4	9.2		1.6	1.1		17.4	27.6		5.2	31.0		6758	386	
533B	38	121.8		135.0	33.3		18.4	2.1		2.5	1.4		3.1	14.6		21.9	5.4		34.1	6977		509
532A	49	139.1	101.0		43.0	19.6		3.0	4.0		1.2	1.8		16.9	17.9		4.2	33.5		6428	358	
532B	49	133.1	99.7	158.0	40.6	15.3	23.3	2.7	2.3	2.7	1.4	2.2	2.7	16.9	23.1	23.1	2.0	21.5	33.0	8021	403	538
518	59	153.9	137.0	158.0	41.8	26.2	26.0	3.4	3.4	6.4	1.8	2.0	2.8	13.2	28.9	26.5	0.9	30.5	30.1	6977	145	230
531A	70	145.1	103.0	147.0	43.0	18.7	26.4	3.4	2.9	3.3	1.4	1.3	2.3	12.6	25.0	23.1	5.1	26.0	33.0	8021	249	334
533E	38	83.8	151.0	149.0	22.4	25.1	25.3	2.1	3.2	3.4	1.1	2.6	2.4	9.0	27.0	24.0	0.1	30.8	29.8	27	331	406
532C	49	119.0		73.6	32.1		14.0	2.2		2.1	1.3		1.4	11.2		13.6	0.2		1.6			398
513	80	133.9	99.4	130.0	36.0	23.5	24.6	2.9	1.9	4.8	1.3	1.3	2.0	10.1	17.2	24.2	0.1	34.8	28.3	7197	488	392
530A	94	119.8			31.6			2.8			1.1			9.6			0.2			4703		
530B	94	137.1	105.0	118.0	37.0	25.5	22.4	3.1	4.0	2.9	1.3	1.4	2.6	10.4	23.4	25.9	0.4	24.2	30.5	6813	269	370
530C	94	91.0	103.0	70.4	25.0	25.4	15.1	2.3	2.4	1.8	1.1	1.5	1.3	9.8	25.6	16.0	0.9	24.3	13.2	1610	490	394
510	107	119.0	104.0	122.0	31.1	25.8	26.9	2.2	1.2	2.2	1.3	1.6	1.7	10.4	18.6	22.0	0.1	29.2	26.3	3082	868	667
515A	139	123.8	84.0		34.0	20.6		2.3	6.4		1.3	1.7		10.7	10.6		0.1	0.0		5	296	
527	180	81.0			22.1			2.2			1.1			8.4			0.1			5		
529	185	73.3			20.7			--			0.0			0.3			0.1			5		

*Data from Bennett et al. (1993)

†Unpublished data from USGS Reston Biogeochemical Processes in Groundwater Laboratory

Appendix A (continued)

well ID	m fr. oil center	Al (µg/L)			Ba (µg/L)			Ni (µg/L)			Sr (µg/L)			B (µg/L)			Li (µg/L)			Cu (µg/L)		
		1986	2011	2021	1986	2011	2021	1986	2011	2021	1986	2011	2021	1986	2011	2021	1986	2011	2021	1986	2011	2021
310E	-199		125.0	<5	75.5	36.1	42.9	<8.8	382.0	0.9		48.8	53.2		393.0	10.2		<10	2			3
604A	-34	14.0	1.3	140.0			701.0		0.0	47.9	43.8	2.8	245.0		<100	<100		<10	<10		2	40
421	0		13.1	200.0	460.0	231.0	281.0	76.3	27.6	53.0		185.0	232.0		<100	<100		<10	10		17	37
522	28	92.8	<10	<5	649.6	618.0	680.0	32.3	71.2	39.7	227.8	277.0	289.0		<100	73.7		<10	5		<1.00	1
533D	38	51.0	<10		549.3	1190		38.1	47.0		254.1	253.0			254.0			<10			<1.00	
533B	38	48.0		<5			437.0			1.3	227.8		225.0			12.4			2			<0.5
532A	49		0.0		373.5	623.0		70.4	29.0			191.0										
532B	49	55.8	200.0	<5		394.0	504.0		12.9	2.6	210.3	167.0	225.0		390.0	13.1		11	3		22	<0.5
518	59		240.0	<5	346.1	314.0	442.0	49.9	27.6	10.7		161.0	225.0		390.0	15.1		<10	3		29	<0.5
531A	70	55.3	135.0	<5	280.1	306.0	439.0	29.3	21.3	8.9	184.0	139.0	201.0		179.0	18.0		<10	4		3	<0.5
533E	38	55.0	215.0	<5		451.0	544.0		21.8	18.5	149.0	165.0	205.0		400.0	16.4		11	4		19	<0.5
532C	49			120.0			171.0			15.0			195.0			950.0			<10			29
513	80		<100	<5	271.9	296.0	310.0	44.0	10.0	13.1		175.0	191.0		<50	19.1		<10	4		1	<0.5
530A	94	48.0			160.7			59.9			149.0				405.0			11			7	
530B	94	55.8	275.0	<5		118.0	181.0		8.5	1.1	122.7	188.0	178.0		395.0	11.5		11	2		40	<0.5
530C	94		325.0	<5		106.0	112.0		16.9	0.7		169.0	89.5			11.6			3			<0.5
510	107		<100	<5	200.5	250.0	263.0	<8.8	3.2	3.5		211.0	176.0		<50	21.8		<10	3		1	<0.5
515A	139	51.0	210.0		249.9	94.2		17.6	5.0		122.7	135.0			<50			<10			2	
527	180	35.1			130.5			8.8			157.7											
529	185	24.8									78.9											

Appendix A (continued)

well ID	m fr. oil center	Zn (µg/L)			Be (µg/L)			V (µg/L)			Cr (µg/L)			Co (µg/L)			Rb (µg/L)			Mo (µg/L)		
		1986	2011	2021	1986	2011	2021	1986	2011	2021	1986	2011	2021	1986	2011	2021	1986	2011	2021	1986	2011	2021
310E	-199		176.0	<2		<1	<0.5		<1	<0.5		<10	1.0		<1	<0.5		<1	<2		<1	<0.5
604A	-34		22.5	140		ND	<1		2.3	6.0		<10	10.0		12.1	8.4		2.0	2.5		<1.00	2.8
421	0		28.0	210		ND	<1		3.7	1.7		10.0	<10		8.0	8.8		1.2	1.2		<1.00	1.9
522	28		28.3	<2		ND	<0.5		3.1	<0.5		10.0	0.9		21.6	11.5		1.3	<2		2.0	0.9
533D	38		585.0			ND			4.1			<10			17.5			<1.0			1.4	
533B	38			<2			<0.5			<0.5			<0.5			2.7			3.2			2.0
532A	49																					
532B	49		75.0	<2		<1	<0.5		<1	<0.5		<10	<0.5		2.4	3.1		3.0	2.6		2.0	2.0
518	59		100.0	3		<1	<0.5		4.1	<0.5		14.2	<0.5		14.1	15.0		1.9	3.0		2.6	4.0
531A	70		452.0	<2		<1	<0.5		<1	<0.5		<10	<0.5		9.1	7.5		1.4	2.7		2.3	3.3
533E	38		ND	<2		<1	<0.5		3.3	0.8		10.4	2.1		7.2	7.3		2.2	2.7		1.5	2.1
532C	49			110			<1			4.0			10.0			9.6			2.4			3.0
513	80		42.0	<2		<1	<0.5		<1	<0.5		<10	<0.5		8.4	8.8		1.3	<2		2.6	3.5
530A	94		1930			<1			3.7			12.5			2.8			1.2			3.1	
530B	94		82.4	<2		<1	<0.5		1.9	<0.5		<10	<0.5		2.5	4.4		1.0	<2		4.0	2.5
530C	94			<2			<0.5			<0.5			<0.5			0.7			<2			1.5
510	107		40.0	<2		<1	<0.5		<1	<0.5		<10	<0.5		3.4	2.2		1.2	<2		2.6	3.2
515A	139		392.0			<1			<1			<10			<0.5			1.3			<1.0	
527	180																					
529	185																					

Appendix A (continued)

well ID	m fr. oil center	Ag (µg/L)			Cd (µg/L)			Sb (µg/L)			Sn (µg/L)			As (µg/L)			Se (µg/L)			Cs (µg/L)		
		1986	2011	2021	1986	2011	2021	1986	2011	2021	1986	2011	2021	1986	2011	2021	1986	2011	2021	1986	2011	2021
310E	-199		<1	<0.5		<1	<0.5		<1	<0.5		<1	ND		<1	0.7		<10	<1		<0.2	ND
604A	-34		ND	<0.5		<0.5	<0.5		<1	<1		ND	<1		55.0	67.7		<10	<10		ND	<0.2
421	0		ND	<0.5		<0.5	<0.5		<1	<1		ND	<1		230.0	91.3		<10	<10		ND	<0.2
522	28		ND	<0.5		<0.5	<0.5		<1	<0.5		ND	ND		95.1	29.1		<10	<1		ND	ND
533D	38		ND			<0.5			<1			ND			140.0			<10			ND	
533B	38			<0.5			<0.5			<0.5			ND			50.4			<1			ND
532A	49																					
532B	49		<0.5	<0.5		<0.5	<0.5		<1	<0.5		<10	ND		38.1	76.8		<10	<1		<0.2	ND
518	59		<0.5	<0.5		<0.5	<0.5		<1	<0.5		<1	ND		62.9	114.0		<10	<1		<0.2	ND
531A	70		<0.5	<0.5		<0.5	<0.5		<1	<0.5		ND	ND		53.9	90.0		<10	<1		<0.2	ND
533E	38		<0.5	<0.5		<0.5	<0.5		<1	<0.5		<1	ND		43.4	89.8		<10	<1		<0.2	ND
532C	49			<0.5			<0.5			<1			<1			8.0			<10			<0.2
513	80		<0.5	<0.5		<0.5	<0.5		<1	<0.5		ND	ND		34.5	83.1		<10	<1		<0.2	ND
530A	94		<0.5			<0.5			<1			<1			34.7			<10			<0.2	
530B	94		<0.5	<0.5		<0.5	<0.5		<1	<0.5		<1	ND		26.4	43.1		<10	<1		<0.2	ND
530C	94			<0.5			<0.5			<0.5			ND			8.9			<1			ND
510	107		<0.5	<0.5		<0.5	<0.5		<1	<0.5		ND	ND		17.1	30.6		<10	<1		<0.2	ND
515A	139		1			<0.5			<1			ND			<1.0			<10			<0.2	
527	180																					
529	185																					

Appendix A (continued)

well ID	m fr. oil center	Tl (µg/L)			Pb (µg/L)			U (µg/L)			La (µg/L)			Ce (µg/L)			Bi (µg/L)			Th (µg/L)		
		1986	2011	2021	1986	2011	2021	1986	2011	2021	1986	2011	2021	1986	2011	2021	1986	2011	2021	1986	2011	2021
310E	-199		<1	<0.5		0.7	<0.5		<0.2	<0.5		<0.2	<1		<0.1	<2		<0.2	ND		<0.2	ND
604A	-34		<1.0	<0.5		0.1	2.7		<0.10	1.6		ND	0.6		ND	1.1		ND	<0.2		ND	<0.2
421	0		<1.0	<0.5		0.2	1.8		<0.10	<0.05		ND	<0.2		ND	<0.2		ND	0.2		ND	<0.2
522	28		<1.0	<0.5		0.5	<0.5		<0.10	<0.5		ND	<1		ND	<2		ND	ND		ND	ND
533D	38		<1.0			0.1			<0.10			ND			ND			ND			ND	
533B	38			<0.5			<0.5			<0.5			<1			<2			ND			ND
532A	49																					
532B	49		<0.5	<0.5		1.1	<0.5		<0.05	<0.5		<0.2	<1		<0.2	<2		<0.2	ND		<0.2	ND
518	59		<0.5	<0.5		1.9	<0.5		<0.05	<0.5		0.2	<1		0.4	<2		<0.2	ND		<0.2	ND
531A	70		<0.5	<0.5		<0.5	<0.5		<0.05	<0.5		ND	<1		ND	<2		ND	ND		<0.2	ND
533E	38		<0.5	<0.5		0.8	<0.5		<0.05	<0.5		<0.2	<1		<0.2	<2		<0.2	ND		<0.2	ND
532C	49			<0.5			1.2			0.1			<0.2			<0.2			<0.2			<0.2
513	80		<0.5	<0.5		<0.5	<0.5		0.1	<0.5		ND	<1		ND	<2		ND	ND		<0.2	ND
530A	94		<0.5			1.3			0.2			<0.2			0.4			<0.2			<0.2	
530B	94		<0.5	<0.5		1.2	<0.5		<0.05	<0.5		<0.2	<1		0.3	<2		<0.2	ND		<0.2	ND
530C	94			<0.5			<0.5			<0.5			<1			<2			ND			ND
510	107		<0.5	<0.5		<0.5	<0.5		0.3	<0.5		ND	<1		ND	<2		ND	ND		<0.2	ND
515A	139		<0.5			<0.5			0.4			ND			ND			ND			<0.2	
527	180																					
529	185																					

Appendix B: Fingerprint matrices of 18 elements quantified in sequential chemical extractions.

Aluminum													
Zone		Background			Methanogenic			Interface			Fe-Reducing		
Compared to zone		Methan	Interf	Fe-Red	Back	Interf	Fe-Red	Back	Methan	Fe-Red	Back	Methan	Inter
phase	Carbonates												
	Oxides									-1			1
	Organics												

Arsenic													
Zone		Background			Methanogenic			Interface			Fe-Reducing		
Compared to zone		Methan	Interf	Fe-Red	Back	Interf	Fe-Red	Back	Methan	Fe-Red	Back	Methan	Inter
phase	Carbonates												
	Oxides												
	Organics	-1		-1	1	1	-1		-1	-1	1	1	1

Boron													
Zone		Background			Methanogenic			Interface			Fe-Reducing		
Compared to zone		Methan	Interf	Fe-Red	Back	Interf	Fe-Red	Back	Methan	Fe-Red	Back	Methan	Inter
phase	Carbonates		1					-1					
	Oxides						1					-1	
	Organics	-1		-1	1	1			-1	-1	1		1

Barium													
Zone		Background			Methanogenic			Interface			Fe-Reducing		
Compared to zone		Methan	Interf	Fe-Red	Back	Interf	Fe-Red	Back	Methan	Fe-Red	Back	Methan	Inter
phase	Carbonates			1			1			1	-1	-1	-1
	Oxides			1							-1		
	Organics						1					-1	

Calcium													
Zone		Background			Methanogenic			Interface			Fe-Reducing		
Compared to zone		Methan	Interf	Fe-Red	Back	Interf	Fe-Red	Back	Methan	Fe-Red	Back	Methan	Inter
phase	Carbonates			1							-1		
	Oxides			1			1			1	-1	-1	-1
	Organics			1			1			1	-1	-1	-1

Cerium													
Zone		Background			Methanogenic			Interface			Fe-Reducing		
Compared to zone		Methan	Interf	Fe-Red	Back	Interf	Fe-Red	Back	Methan	Fe-Red	Back	Methan	Inter
phase	Carbonates												
	Oxides						1					-1	
	Organics									1			-1

Cobalt													
Zone		Background			Methanogenic			Interface			Fe-Reducing		
Compared to zone		Methan	Interf	Fe-Red	Back	Interf	Fe-Red	Back	Methan	Fe-Red	Back	Methan	Inter
phase	Carbonates												
	Oxides			1			1				-1	-1	
	Organics												

Chromium													
Zone		Background			Methanogenic			Interface			Fe-Reducing		
Compared to zone		Methan	Interf	Fe-Red	Back	Interf	Fe-Red	Back	Methan	Fe-Red	Back	Methan	Inter
phase	Carbonates												
	Oxides			-1						-1	1		1
	Organics	-1	-1	-1	1	1		1	-1	-1	1		1

Copper													
Zone		Background			Methanogenic			Interface			Fe-Reducing		
Compared to zone		Methan	Interf	Fe-Red	Back	Interf	Fe-Red	Back	Methan	Fe-Red	Back	Methan	Inter
phase	Carbonates					-1			1	1			-1
	Oxides												
	Organics												

Iron													
Zone		Background			Methanogenic			Interface			Fe-Reducing		
Compared to zone		Methan	Interf	Fe-Red	Back	Interf	Fe-Red	Back	Methan	Fe-Red	Back	Methan	Inter
phase	Carbonates	-1	-1	-1	1			1			1		
	Oxides	1	1	1	-1			-1			-1		
	Organics	-1	-1	-1	1	1		1	-1		1		

Lanthanum													
Zone		Background			Methanogenic			Interface			Fe-Reducing		
Compared to zone		Methan	Interf	Fe-Red	Back	Interf	Fe-Red	Back	Methan	Fe-Red	Back	Methan	Inter
phase	Carbonates												
	Oxides						1					-1	
	Organics	-1			1								

Magnesium													
Zone		Background			Methanogenic			Interface			Fe-Reducing		
Compared to zone		Methan	Interf	Fe-Red	Back	Interf	Fe-Red	Back	Methan	Fe-Red	Back	Methan	Inter
phase	Carbonates	1	1	1	-1			-1			-1		
	Oxides			1			1			1	-1	-1	-1
	Organics			1			1			1	-1	-1	-1

Manganese													
Zone		Background			Methanogenic			Interface			Fe-Reducing		
Compared to zone		Methan	Interf	Fe-Red	Back	Interf	Fe-Red	Back	Methan	Fe-Red	Back	Methan	Inter
phase	Carbonates	-1			1		1			1		-1	-1
	Oxides			1			1			1	-1	-1	-1
	Organics					1	1		-1			-1	

Nickel													
Zone		Background			Methanogenic			Interface			Fe-Reducing		
Compared to zone		Methan	Interf	Fe-Red	Back	Interf	Fe-Red	Back	Methan	Fe-Red	Back	Methan	Inter
phase	Carbonates			1			1				-1	-1	
	Oxides						1					-1	
	Organics	-1		-1	1					-1	1		1

Lead													
Zone		Background			Methanogenic			Interface			Fe-Reducing		
Compared to zone		Methan	Interf	Fe-Red	Back	Interf	Fe-Red	Back	Methan	Fe-Red	Back	Methan	Inter
phase	Carbonates	-1	-1		1		1	1		1		-1	-1
	Oxides			1							-1		
	Organics												

Silicon													
Zone		Background			Methanogenic			Interface			Fe-Reducing		
Compared to zone		Methan	Interf	Fe-Red	Back	Interf	Fe-Red	Back	Methan	Fe-Red	Back	Methan	Inter
phase	Carbonates												
	Oxides	1			-1		-1					1	
	Organics					-1	-1		1			1	

Strontium													
Zone		Background			Methanogenic			Interface			Fe-Reducing		
Compared to zone		Methan	Interf	Fe-Red	Back	Interf	Fe-Red	Back	Methan	Fe-Red	Back	Methan	Inter
phase	Carbonates			1			1				-1	-1	
	Oxides												
	Organics												

Zinc													
Zone		Background			Methanogenic			Interface			Fe-Reducing		
Compared to zone		Methan	Interf	Fe-Red	Back	Interf	Fe-Red	Back	Methan	Fe-Red	Back	Methan	Inter
phase	Carbonates												
	Oxides	-1			1	1			-1				
	Organics					-1			1	-1			1

Appendix C: Formation Constants of Divalent Carbonates, adapted from Robie and Hemingway (2002)

Carbonate Mineral Formula	Formation Constant (K_f)
$PbCO_3$	109.58
$FeCO_3$	119.63
$ZnCO_3$	128.82
$MnCO_3$	143.5
$MgCO_3$	180.36
$CaCO_3$	197.7
$BaCO_3$	198.35
$SrCO_3$	199.29
$CaMgCO_3$	378.65